

UNIVERSITY COLLEGE LONDON

PhD Thesis

**Structure-Transport Properties of
Fluids in Narrow Pores:
Relevance to Shale gas**

Author:

Sakiru Babatunde Badmos

Supervisor:

Prof. Alberto Striolo

*A dissertation submitted in fulfilment of the degree
of Doctor of Philosophy*

in the

Department of Chemical Engineering

February 2020

Declaration of Authorship

I, Sakiru Babatunde Badmos, declare that this thesis titled, “Structure-Transport Properties of Fluids in Narrow Pores: Relevance to Shale gas” and the works presented in it are my own. Where information has been derived from other sources, I confirm that they have been properly indicated in the thesis.

Signed:

Date:

Abstract

Shale gas has attracted significant attention in the past decade. Pioneered by the USA since the 1940s, the production of shale gas in Europe is still in its early stage and has not been attempted in Africa. Oil and gas production from shale is technologically difficult, in part due to very small sizes of pores in shale formations and poor pore connectivity. Experimental characterisation has revealed heterogeneous nature of shale, and a network of connected pores is actually not visible at the resolution of tens of nanometers. Poor pore connectivity in shale rocks is responsible for its low permeability. To produce oil and gas from shale formations, more advanced technology such as horizontal drilling and hydraulic fracturing is required. However, recovery is still very low as oil rate drops rapidly. To improve production, enhanced oil recovery (EOR) is proposed. In order to design advanced EOR technologies, fluid–fluid and fluid–rock interactions in nanopores are crucial. This thesis seeks to better understand the behaviour of fluids confined in narrow pores. The techniques of choice are based on molecular dynamics simulations, conducted at the atomic resolution. The pores considered are of slit-shaped geometry and of dimensions as small as 1–2.2 nm carved out of silica, muscovite, MgO, alumina and graphite. The fluids simulated include hydrocarbons, such as *n*-butane and *n*-octane, as well as a few other fluids, including H₂O, CO₂, H₂S and N₂. The results show, in qualitative agreement with literature observations, that confinement affects the structure of aqueous H₂S due to perturbation of water coordination around H₂S. It was also found that injection of H₂S or CO₂ could help to displace hydrocarbon from the confining pore surfaces, and that the performance of the injected gas depends on the chemistry of the surface. CO₂ and H₂S could displace hydrocarbons from inorganic surfaces but not from organic surface. Analysis of the interaction energy between confined fluids and the pore surfaces shows that the results depend on gas–surface and hydrocarbon–surface interactions. At the conditions simulated, CO₂ or H₂S suppressed hydrocarbon mobility due to pore crowding. These findings could contribute to designing advanced EOR strategies for achieving both improved hydrocarbon production, acid gas sequestration as well as natural gas sweetening.

Impact Statement

The increase in global population and decline in fossil energy sources has led to tremendous effort towards alternative energy sources. Shale gas and oil has been found to be an option to achieve this purpose. To improve production from shale reservoirs, it is crucial to understand rock-fluid and fluid-fluid interactions and their implications on fluid structure and transport. This thesis provides detailed molecular-level information about fluid behaviour in model sub-surface formations.

The removal of sour gases from natural gas is achieved industrially by absorption-stripping processes, membrane separation and adsorption. In this thesis, the effect of confinement on H_2S solubility, structural and dynamical properties was studied, and it was found that hydrated silica pore could function as a material for separating H_2S from natural gas due to higher permeability of H_2S compared to other typical components of natural gas. The results could form a basis for developing new natural gas sweetening technologies.

Enhanced oil recovery (EOR) is a technology used to improve hydrocarbon recovery in oil and gas production. As a contribution to EOR technology, the injection of CO_2 , H_2S and N_2 into model solid substrates containing hydrocarbons was studied to investigate the ability of the gases to displace hydrocarbon from the pore surfaces. This study is invaluable as it gives access into the mechanism of enhanced hydrocarbon recovery. It was found that H_2S preferentially adsorb on porous media and facilitates displacement of hydrocarbon from the surface of the porous media. This could form a basis for understanding the mechanism of gas-based EOR. The results also show that mixture of CO_2 and H_2S does not give synergistic effect in terms of hydrocarbon displacement from the pore surfaces. The results from this study is useful for improving EOR technology.

Acknowledgements

All praise belongs to **Allah** the giver and taker of life. I am grateful to Him for His unearned mercy and favour bestowed on me that has made it possible for me to complete my PhD. I will always be grateful to you my Lord.

Special thanks to my advisor **Professor Alberto Striolo** for his support and encouragement throughout my study. Thank you very much sir. I am really grateful. I am also grateful to our collaborator, **Prof. David R. Cole** from the Ohio State University, USA, for his contributions.

To my beloved wife, **Mrs Ruqoyyah Amoke Badmos**, I must say that your prayers, perseverance and encouragement kept me on this journey. Thank you very much for being a wonderful wife.

I am very grateful to Allah for blessing me with wonderful kids during the most challenging phase of my life. The birth of **Labeebah Ebunoluwa** is a consolation during the period of trial and struggle, while the arrival of my twins (**Masroor Araoluwa and Mahboob Ifeoluwa**) is a remarkable turning point during this journey. Your birth, though very challenging brought breakthrough and progress in my research. I love you so much my beloved kids.

I am grateful to my parents (**Mr Sirajudeen Badmos and Late Mrs Hikmot Badmos**) for your prayers and for laying the good foundation for my academic pursuit. I pray Allah overlooks my mother's shortcomings and count her among His righteous servants (Aameen).

I say thank you to everyone in Professor Striolo's group (past and present) especially **Dr Anh Phan** for her contributions to my research work and **Ms Abeer Khedr** for her encouragement and prayers, and to all my friends for moral support and prayers. Special thanks to **Dr Saheed Busari** for his contribution to the success of my thesis.

Once again, I am grateful to Allah who with His mercy, acts of good deeds are completed.

Publications

The work presented in this thesis has been published in the following articles or in preparation.

1. **Sakiru B. Badmos**, David R. Cole and Alberto Striolo. Aqueous Hydrogen Sulphide in Slit-Shaped Silica Nano-Pores: Confinement Effects on Solubility, Structural and Dynamical Properties. *Journal of Physical Chemistry C*, 2018, 122, 14744-14755.
2. **Sakiru B. Badmos**, Tai Bui, David R. Cole and Alberto Striolo. Factors Governing the Enhancement of Hydrocarbon Recovery via H₂S and/or CO₂ Injection: Insights from a Molecular Dynamics Study in Dry Nano-Pores. *Journal of Physical Chemistry C*, 2019, 123, 23907-23918.
3. **Sakiru B. Badmos**, Urvi Shah, Naimul Islam, David R. Cole and Alberto Striolo. Competitive Adsorption and Reduced Mobility: *N*-Octane, CO₂ and H₂S in Alumina and Graphite Pores. *In Preparation*.

Contents

| | |
|--|-------------|
| Declaration of Authorship | i |
| Abstract | ii |
| Impact Statement | iii |
| Acknowledgements | iv |
| Publications | vi |
| List of Figures | xi |
| List of Tables | xvii |
| | |
| 1 Introduction | 1 |
| 2 Simulation Models and Methodology | 6 |
| 2.1 Molecular Dynamics Simulation | 6 |
| 2.1.1 Background | 6 |
| 2.1.2 Force fields | 8 |
| 2.1.3 Algorithms | 12 |
| 2.1.4 Periodic boundary condition | 13 |
| 2.1.5 Thermostat | 15 |
| 2.1.5.1 Velocity rescaling | 16 |
| 2.1.5.2 Berendsen Thermostat | 17 |
| 2.1.5.3 Anderson Thermostat | 17 |
| 2.1.5.4 Nosé–Hoover | 18 |
| 2.2 Statistical mechanics and molecular simulation | 18 |
| 2.2.1 Ensemble | 19 |
| 2.3 Techniques for result analysis | 21 |
| 2.3.1 Radial distribution function (RDF) | 22 |

| | | |
|----------|---|-----------|
| 2.3.2 | Mean Square Displacement (MSD) | 23 |
| 2.3.3 | Residence Correlation function (RCF) | 25 |
| 2.3.4 | Spatial Distribution function | 26 |
| 3 | Aqueous Hydrogen Sulfide in Slit-Shaped Silica Nanopores: Confinement Effects on Solubility, Structural, and Dynamical Properties | 27 |
| 3.1 | Abstract | 27 |
| 3.2 | Introduction | 28 |
| 3.3 | Simulation Methods and Algorithms | 32 |
| 3.3.1 | Simulation set up | 32 |
| 3.3.1.1 | Pseudo-bulk systems | 32 |
| 3.3.1.2 | Confined system | 34 |
| 3.3.2 | Force fields | 35 |
| 3.3.3 | Algorithms | 37 |
| 3.4 | Results and discussion | 38 |
| 3.4.1 | Pseudo-bulk systems | 38 |
| 3.4.2 | Confined systems | 43 |
| 3.4.2.1 | Density profiles | 43 |
| 3.4.2.2 | Solubility | 44 |
| 3.4.2.3 | Hydration structure | 46 |
| 3.4.3 | Effect of pore size | 49 |
| 3.4.4 | Structural properties | 54 |
| 3.4.4.1 | Orientation of confined fluid molecules | 54 |
| 3.4.4.2 | In-plane density distributions | 56 |
| 3.4.5 | Dynamical properties | 58 |
| 3.4.5.1 | Diffusion coefficients | 58 |
| 3.4.5.2 | Residence times and Rotational dynamics | 62 |
| 3.5 | Conclusions | 67 |
| 3.6 | Acknowledgements | 69 |
| 4 | Factors Governing the Enhancement of Hydrocarbon Recovery via Acid Gas Injection: Insights from A Molecular Dynamics Study in Dry Nano-Pores | 70 |
| 4.1 | Abstract | 70 |
| 4.2 | Introduction | 72 |
| 4.3 | SIMULATION MODELS AND METHODOLOGY | 75 |
| 4.3.1 | Simulation set up | 75 |
| 4.3.2 | Force field | 80 |
| 4.3.3 | Algorithms | 81 |
| 4.4 | RESULTS AND DISCUSSION | 82 |
| 4.4.1 | Binary Systems: Enhancement of butane displacement by H ₂ S and CO ₂ | 82 |

| | | |
|----------|---|------------|
| 4.4.1.1 | Density profiles | 82 |
| 4.4.1.2 | Interaction energy in silica pores | 86 |
| 4.4.1.3 | Residence times | 88 |
| 4.4.2 | Ternary systems | 91 |
| 4.4.2.1 | Effect of H ₂ S-CO ₂ mixture on <i>n</i> -butane displacement | 91 |
| 4.4.2.2 | Effect of acid gas-N ₂ mixture on <i>n</i> -butane displacement | 92 |
| 4.4.3 | Effect of Pore Surface Chemistry | 93 |
| 4.4.3.1 | Density profiles and percentage removals | 93 |
| 4.4.3.2 | Interaction energy | 98 |
| 4.4.3.3 | Residence times | 100 |
| 4.4.3.4 | Effect of Nitrogen | 102 |
| 4.4.4 | Molecular Structure of Adsorbed Gases | 103 |
| 4.4.4.1 | Orientation of adsorbed gases in the first adsorbed layer | 103 |
| 4.4.4.2 | Planar density distribution | 105 |
| 4.4.4.3 | Diffusion Coefficient of confined fluids | 106 |
| 4.5 | Conclusions | 113 |
| 4.6 | Acknowledgements | 114 |
| 5 | Competitive Adsorption and Mobility: N-Octane, CO₂ and H₂S in Alumina and Graphite Pores | 115 |
| 5.1 | Abstract | 115 |
| 5.2 | Introduction | 116 |
| 5.3 | Simulation Methods and Algorithms | 119 |
| 5.3.1 | Simulation set up | 119 |
| 5.3.2 | Force fields | 122 |
| 5.3.3 | Algorithms | 122 |
| 5.4 | Results and Discussion | 123 |
| 5.4.1 | Density Profiles | 123 |
| 5.4.2 | Interaction Energy | 126 |
| 5.4.3 | Structure of adsorbed acid gas | 128 |
| 5.4.3.1 | In-plane density distribution | 128 |
| 5.4.3.2 | Molecular Length and Orientation of <i>n</i> -octane | 130 |
| 5.4.4 | Diffusion coefficient of confined fluids | 132 |
| 5.5 | Conclusions | 134 |
| 6 | Summary and Outlook | 136 |
| A | Methodology | 140 |
| B | Supporting Information for Chapter 4 | 142 |
| B.1 | Determination of the required number of fluid molecules | 142 |

| | |
|------------------------------------|------------|
| B.2 Pressure calculation | 143 |
| Bibliography | 154 |

List of Figures

| | | |
|-----|--|----|
| 2.1 | Periodic boundary conditions. The unit cell is enclosed in green . . . | 14 |
| 2.2 | Radial distribution function of a liquid | 23 |
| 2.3 | MSD plot showing ballistic and diffusive regimes | 24 |
| 3.1 | Initial configuration for the pseudo-bulk simulation containing 400 molecules of water and 40 molecules of H ₂ S is shown in the panel (a). Simulation snapshots of the simulated pores are shown in panels (b–d). The pore widths are (b) 1, (c) 1.49, and (d) 2.2 nm. For the fluid molecules, oxygen atoms are shown in red, sulfur atoms in yellow, and hydrogen atoms in white | 33 |
| 3.2 | Density profiles of H ₂ S in X-direction at different H ₂ S loadings for 1nm pore. | 36 |
| 3.3 | Density profiles of sulfur of H ₂ S (S) and oxygen atom of water (OW) along the Z-direction of the simulation box at different bulk pressures. Only one profile is shown for OW because it does not change significantly with pressure. | 39 |
| 3.4 | Comparison of (a) Simulated solubility of H ₂ S in water compared against the experimental data of Kuranov et al. (b) Simulated water IFT compared against the experimental data of Shah et al. In both cases, the results are shown as a function of H ₂ S pressure. In the simulations, the errors were estimated as standard deviation from the mean | 40 |
| 3.5 | Hydration structure of H ₂ S in bulk water under atmospheric conditions. (a) RDF between sulfur (S) of H ₂ S and oxygen of water (OW), (b) RDF between sulfur of H ₂ S and hydrogen atoms of water (HW).In panels (a and b), the literature datasets are from Riahi and Rowley. The arrow in panel (b) highlights a shoulder discussed in the text. | 44 |
| 3.6 | 3D distribution of OW around H ₂ S. The iso-density surface is drawn at 0.363 Å ⁻³ | 45 |
| 3.7 | Density profile of oxygen atoms of H ₂ O (OW, red line) at 23 bar and sulfur atom of H ₂ S (S) along the direction perpendicular to the pore surface at different bulk pressures for a 1 nm slit pore | 46 |
| 3.8 | H ₂ S solubility in water as a function of bulk pressure. The results are shown for bulk water and confined water in all pore sizes simulated. Lines are only guides to the eye. | 47 |

| | | |
|------|--|----|
| 3.9 | Comparison of RDF between S of H ₂ S and OW of H ₂ O in the 1.0 nm-wide pore and in the bulk(a); 3D SDF of OW in the first hydration shell of H ₂ S (b) in bulk water and (c) confined in a 1 nm-wide pore. The iso-density surfaces are drawn at 0.364 and 0.303 Å ⁻³ for bulk and confined water respectively. It was necessary to consider slightly different iso-density surfaces for computational reasons. The results show that the distribution of OW is denser in the hydration structure of bulk H ₂ S. | 49 |
| 3.10 | Density profile of oxygen atoms of H ₂ O (OW, red line) and sulfur atom of H ₂ S (S) along the direction perpendicular to the pore surface at different bulk pressures for (a) 1.49nm (b) 2.2nm pores. LS1 denotes the H ₂ S layer near the second hydration layer. Note that density profiles OW of H ₂ O (red line) for panels (a and b) are at 26.0 and 24.2 bar respectively | 51 |
| 3.11 | RDF between sulfur atom of H ₂ S and water oxygen in all simulated pores and in the bulk | 53 |
| 3.12 | 3D SDF of water oxygen atoms in the first hydration shell of H ₂ S in all pores and in bulk water. The iso-density surfaces are drawn at 0.364, 0.303, 0.318 and 0.345 Å ⁻³ for a,b,c and d respectively. For computational reasons, the iso-density surfaces are drawn at slightly different densities | 54 |
| 3.13 | Distribution of angle theta, formed between the dipole moment vector and H-H vector of water and the vector normal to the surface | 56 |
| 3.14 | Density profiles of OW and HW in the direction perpendicular to the pore surface for 1nm pore | 57 |
| 3.15 | Distribution of angle theta, formed between the S-M vector and the H-H vector of H ₂ S and the vector normal to the surface for H ₂ S molecules in LS1 and middle of the pore for (a) 2.2nm (b) 1.49nm (c) 1nm at 23 bar. For 1nm-size pore, only angle distribution for H ₂ S molecules at the middle of the pore is shown in panel (c) | 58 |
| 3.16 | In-plane density distribution of oxygen atoms of water (OW) in layer LO1 (a) and LO2 (b). In plane density distribution of sulfur atoms of H ₂ S in layer LS1 (c). The results are obtained for the 1.49 nm-wide silica pore. The pore contains 800 H ₂ S and 7600 H ₂ O molecules | 59 |
| 3.17 | Mean square displacements of sulphur of H ₂ S (a) and oxygen of water (b) in the simulated hydrated pores compared with that of bulk water at 23 bar. | 61 |
| 3.18 | End point of vectors connecting positions of H ₂ S molecules at time t and $t + \Delta t$ ($\Delta t=250$ ps) in (a) 1nm pore (b) 1.49nm pore and (c) 2.2 nm pore | 63 |

| | | |
|------|--|----|
| 3.19 | Residence autocorrelation function for water molecules found within layers LO1, LO2 and in the middle of the pore of width 1.49 nm compared to that of bulk liquid water (a). Residence autocorrelation function for water molecules in layer LO2, H ₂ S molecules in layer LS1, and bulk water molecules (b). The confined system consists of 800 H ₂ S and 7600 H ₂ O molecules. The bulk system consists of 58 H ₂ S and 2064 H ₂ O molecules. | 65 |
| 3.20 | Vector–vector autocorrelation function for fluid molecules at different regions of the 1.49 nm pore compared with that of bulk water. The systems considered are the same as those in Figure 3.19 | 68 |
| 4.1 | Simulation snapshots for binary systems containing <i>n</i> -butane and H ₂ S in silica (a) MgO (b) and muscovite (c). All systems shown contain 300 <i>n</i> -butane and 500 H ₂ S molecules. Cyan spheres are -CH ₃ and -CH ₂ in <i>n</i> -butane, purple are sulphur, white are hydrogen, red are oxygen, yellow are silicon, green are potassium, grey are aluminium, blue are magnesium | 77 |
| 4.2 | Simulation snapshots for binary systems containing <i>n</i> -butane and CO ₂ in silica (a) MgO (b) and muscovite (c). All systems shown contain 300 <i>n</i> -butane and 500 H ₂ S molecules. Cyan spheres are -CH ₃ and -CH ₂ in <i>n</i> -butane, purple are sulphur, white are hydrogen, red are oxygen, yellow are silicon, green are potassium, grey are aluminium, blue are magnesium | 79 |
| 4.3 | Density profile of the COM of <i>n</i> -butane in the binary system with H ₂ S loading (a), CO ₂ loading (b) and N ₂ loading (c). The density profile for a system with pure <i>n</i> -butane is also shown for comparison. All systems contain 300 <i>n</i> -butane molecules | 83 |
| 4.4 | Density profile of S of H ₂ S (a) H of H ₂ S (b) C of CO ₂ (c) O of CO ₂ (d) and N of N ₂ (e) in the binary systems at different acid gas and N ₂ loadings in silica pores. | 85 |
| 4.5 | RCF for <i>n</i> -butane molecules in the first layer at different H ₂ S loading (a) and CO ₂ loading (b). The RCF for system containing pure <i>n</i> -butane is also shown for comparison. RCF of H ₂ S molecules in the first layer at different loading are shown in (c) and for CO ₂ molecules at different loading in (d) | 90 |
| 4.6 | Comparison of density profiles of <i>n</i> -butane in the presence of pure acid gas and their mixture (a) and RCF for the same system (b). The binary systems comprises 300 <i>n</i> -butane and a total of 500 molecules of the acid gas. The mixture comprises 250 molecules of each acid gas. Density profiles of <i>n</i> -butane for varying composition of acid gas is shown in (c). The systems in (c) have a total acid gas loading of 375 and 300 molecules of <i>n</i> -butane | 92 |

| | | |
|------|---|-----|
| 4.7 | Density profiles for COM of <i>n</i> -butane for (a) H ₂ S – N ₂ system (b) CO ₂ – N ₂ system. Density profiles for N of N ₂ for (c) H ₂ S – N ₂ (d) CO ₂ – N ₂ systems. There are 300 <i>n</i> -butane molecules in all cases. The total number of gas molecules is 500. Percentage of hydrocarbon displaced is also shown for H ₂ S – N ₂ (e) and CO ₂ – N ₂ systems (f) | 94 |
| 4.8 | <i>N</i> -butane density profiles at different acid gas loadings for H ₂ S in muscovite (a) CO ₂ in muscovite (b) H ₂ S in MgO (c) and CO ₂ in MgO (d). Density profiles of <i>n</i> -butane at different N ₂ loadings in muscovite (e) and MgO (f). All systems comprises 300 <i>n</i> -butane molecules | 96 |
| 4.9 | Density profile of S of H ₂ S (a) H of H ₂ S (b) C of CO ₂ (c) O of CO ₂ (d) and N of N ₂ (e) in the binary systems at different acid gas and N ₂ loadings in muscovite pores. | 97 |
| 4.10 | Density profile of S of H ₂ S (a) H of H ₂ S (b) C of CO ₂ (c) O of CO ₂ (d) and N of N ₂ (e) in the binary systems at different acid gas and N ₂ loadings in MgO pores. | 99 |
| 4.11 | Magnitude of total interaction energy of <i>n</i> -butane at different acid gas loading for silica (a) muscovite (b) and MgO (c). The systems comprise 300 <i>n</i> -butane molecules and each of the acid gas. The interaction energies are normalised by the number of <i>n</i> -butane molecules in the system. The interaction energy shown is only due to van der Waals interaction as <i>n</i> -butane molecules bear no charge | 100 |
| 4.12 | Magnitude of total interaction energy of acid gases at different acid gas loading for silica (a) muscovite (b) and MgO (c). The systems comprise 300 <i>n</i> -butane molecules and each of the acid gas. The interaction energies are normalised by the number of acid gas molecules in the system. The interaction energy shown is the sum of the LJ and electrostatic contributions. | 102 |
| 4.13 | Probability distribution of angle theta for CO ₂ molecules (a) and H ₂ S molecules (b) adsorbed within 2Å from silica and muscovite surfaces and 5Å from MgO surface. The results are compared with the isotropic distribution. All systems contain 300 <i>n</i> -butane and 500 acid gas molecules | 105 |
| 4.14 | In-plane density distribution of S of H ₂ S in silica (a) muscovite (b) and MgO (c). Snapshot of a section of silica (d) muscovite (e) and MgO (f) are also shown. All systems contain 500 H ₂ S and 300 <i>n</i> -butane | 107 |
| 4.15 | In-plane density distribution of C of CO ₂ in silica (a) muscovite (b) and MgO (c). All systems contain 500 H ₂ S and 300 <i>n</i> -butane | 108 |
| 4.16 | COM MSD for binary systems of <i>n</i> -butane and (a) H ₂ S in silica (b) CO ₂ in silica (c) H ₂ S in muscovite (d) CO ₂ in muscovite (e) H ₂ S in MgO (f) CO ₂ in MgO pores | 110 |

| | | |
|-----|---|-----|
| 5.1 | Simulation snapshots for <i>n</i> -octane - CO ₂ systems in (a) alumina (b) graphite. Snapshots for <i>n</i> -octane-H ₂ S systems in (c) alumina (d) graphite. All systems shown contain 200 <i>n</i> -octane and 500 gas molecules. Cyan spheres are -CH ₃ and -CH ₂ in <i>n</i> -octane, yellow are sulphur, white are hydrogen, red are oxygen and grey are aluminium. For clarity, only a portion of the solid substrates are shown. Please refer to Section 5.3.1 for the simulation boxes. | 121 |
| 5.2 | Density profiles of <i>n</i> -octane in (a) alumina (b) graphite at different H ₂ S loadings and density profiles of COM of <i>n</i> -octane at different CO ₂ loadings in (c) alumina and (d) graphite. All systems contain 200 molecules of <i>n</i> -octane | 124 |
| 5.3 | Density profiles of S of H ₂ S in (a) alumina (b) graphite and density profiles of C of CO ₂ in (c) alumina (d) graphite at different acid gas loadings. All system contain 200 molecules of <i>n</i> -octane | 125 |
| 5.4 | Density profiles of S of H ₂ S in (a) alumina (b) graphite and density profiles of C of CO ₂ in (c) alumina (d) graphite at different acid gas loadings. All system contain 200 molecules of <i>n</i> -octane | 126 |
| 5.5 | <i>n</i> -octane-surface interaction energy for binary systems of <i>n</i> -octane-H ₂ S in (a) alumina (b) graphite and for binary systems of <i>n</i> -octane-CO ₂ in (c) alumina (d) graphite. All systems contain 200 <i>n</i> -octane molecules. The interaction energies are normalised by the number of <i>n</i> -octane in the system | 127 |
| 5.6 | H ₂ S-surface interaction energy for binary systems of <i>n</i> -octane - H ₂ S in (a) alumina (b) graphite and CO ₂ -surface interaction energy for binary systems of <i>n</i> -octane - CO ₂ in (c) alumina (d) graphite. All systems contain 200 <i>n</i> -octane molecules at 350K. The interaction energies are normalised by the number of H ₂ S or CO ₂ in the system | 129 |
| 5.7 | In-plane density distribution of COM of CO ₂ in (a) alumina (b) graphite and same result for H ₂ S in (c) alumina (d) graphite. All systems contain 200 <i>n</i> -octane molecules and 500 molecules of the gas | 130 |
| 5.8 | Probability distribution of angle between C1-C8 vector and normal to the surface and the angle between the orthogonal vector to the plane of C1-C8 vector and C1-C2 vector and the normal to the surface for <i>n</i> -octane occupying (a) first layer (b) middle region. Probability distribution of χ for <i>n</i> -octane occupying (c) first layer (d) middle region. The results are shown for <i>n</i> -octane-H ₂ S in graphite and alumina pores for 500H ₂ S loading | 132 |
| B.1 | Snapshots for simulation set ups used for pressure calculation in (A) Silica (B) Muscovite (C) MgO. All systems contain 300 <i>n</i> -butane molecules, constrained within the pore. There are 3310, 4138 and 4459 CO ₂ molecules in A, B and C respectively. The number of CO ₂ molecules in the pore is ~ 500 in A, B and C | 144 |

| | | |
|------|--|-----|
| B.2 | Simulation snapshots for binary systems containing <i>n</i> -butane and N ₂ in silica (a) Muscovite (b) and MgO (c). All systems shown contain 300 <i>n</i> -butane and 500 H ₂ S molecules. Cyan spheres are -CH ₃ and -CH ₂ in <i>n</i> -butane, purple are sulphur, white are hydrogen, red are oxygen, yellow are silicon, green are potassium, grey are aluminium, blue are magnesium | 145 |
| B.3 | Interaction energy as a function of time over the last 10ns of the simulation for (a) H ₂ S in muscovite (b) CO ₂ in muscovite (c) H ₂ S in silica (d) CO ₂ in silica (e) H ₂ S in MgO (f) CO ₂ in MgO | 146 |
| B.4 | <i>N</i> -butane residence time for binary system of <i>n</i> -butane-H ₂ S in (a) muscovite (c) MgO and binary systems of <i>n</i> -butane-CO ₂ in (b) muscovite (d) MgO. | 147 |
| B.5 | Density profiles of (a) COM of <i>n</i> -butane in <i>n</i> -butane-H ₂ S-N ₂ systems (b) COM of <i>n</i> -butane in <i>n</i> -butane-CO ₂ -N ₂ systems (c) S and N of H ₂ S and N ₂ (d) C and N of CO ₂ and N ₂ at different acid gas-N ₂ ratios in muscovite pores | 148 |
| B.6 | Density profiles of (a) COM of <i>n</i> -butane in <i>n</i> -butane-H ₂ S-N ₂ systems (b) COM of <i>n</i> -butane in <i>n</i> -butane-CO ₂ -N ₂ systems (c) S and N of H ₂ S and N ₂ (d) C and N of CO ₂ and N ₂ at different acid gas-N ₂ ratios in MgO pores | 149 |
| B.7 | In-plane density distribution of H of H ₂ S in silica (a) muscovite (b) and MgO (c). All systems contains 500 H ₂ S and 300 <i>n</i> -butane . . . | 150 |
| B.8 | In-plane density distribution of O of CO ₂ in silica (a) muscovite (b) and MgO (c). All systems contains 500 H ₂ S and 300 <i>n</i> -butane . . . | 151 |
| B.9 | COM MSD for acid gases in binary systems of <i>n</i> -butane-acid gas in (a) silica (b) muscovite (c) MgO | 152 |
| B.10 | COM MSD of <i>n</i> -butane for binary systems of <i>n</i> -butane-N ₂ in (a) silica (b) muscovite (c) MgO; N MSD of N ₂ in (d) silica (e) muscovite (f) MgO | 153 |

List of Tables

| | | |
|------|--|----|
| 2.1 | Partition function of common ensembles | 21 |
| 3.1 | Composition and bulk pressure for the 2-phase systems | 33 |
| 3.2 | Confined system composition with corresponding bulk pressure for 1nm pore | 36 |
| 3.3 | System composition for 1.49nm pore with corresponding bulk pressure | 37 |
| 3.4 | System composition for 2.2nm pore with corresponding bulk pressure | 37 |
| 3.5 | H ₂ S solubility in H ₂ O and H ₂ O IFT at different bulk pressures . . . | 41 |
| 3.6 | Solubility of H ₂ S in Confined Water for 1nm pore ^a | 46 |
| 3.7 | Solubility of H ₂ S in Confined Water for 1.49nm pore ^a | 46 |
| 3.8 | Solubility of H ₂ S in Confined Water for 2.2nm pore ^a | 47 |
| 3.9 | Composition of the Fluid Systems Simulated at 23 bar in Pores with Period Boundary Conditions Implemented along Both the X and Y Directions as Well as in the Bulk | 50 |
| 3.10 | Water–H ₂ S interaction energies in the bulk and the simulated pores. The errors in the Coulombic and LJ interaction energies are standard deviation from the mean while errors in the total interaction energies were obtained from the errors in Coulombic and LJ interaction energies using error propagation method | 53 |
| 3.11 | Diffusion coefficients for H ₂ S in water ^a | 60 |
| 3.12 | Eigenvalues from PCA of H ₂ S diffusion in all hydrated pores | 62 |
| 3.13 | Residence times for water and H ₂ S molecules in different regions in 1.49nm pore and bulk water | 66 |
| 4.1 | Composition of all simulated systems | 80 |
| 4.2 | Bulk Pressure corresponding to the system summarised in Table 4.1. For each pore, the lower and upper pressures are reported, as estimated at increasing acid gas loading. For details, please refer to Appendix B2 | 80 |
| 4.3 | Percentage of <i>n</i> -butane removed from FAL with H ₂ S and CO ₂ loading | 84 |
| 4.4 | <i>N</i> -butane interaction energy with the silica surface. All systems contain 300 <i>n</i> -butane molecules | 88 |
| 4.5 | Acid gas – Surface interaction energy in silica pores normalised by acid gas loading | 90 |
| 4.6 | Percentage of <i>n</i> -butane displaced from FAL in all simulated substrates for acid gas injection at different acid gas loading | 97 |

| | | |
|-----|--|-----|
| 4.7 | Self-diffusion coefficient for <i>n</i> -butane, acid gases and N ₂ in silica pores. The system composition is shown in Table 4.1 | 109 |
| 4.8 | Self-diffusion coefficient for <i>n</i> -butane, acid gases and N ₂ in muscovite pores. The system composition is shown in Table 4.1 | 111 |
| 4.9 | Self-diffusion coefficient for <i>n</i> -butane, acid gases and N ₂ in MgO pores. The system composition is shown in Table 4.1 | 111 |
| 5.1 | Estimated pressure and composition of all simulated systems in this work. In all cases, the simulation temperature was 350K (a = alumina and b = graphite) | 121 |
| 5.2 | Self-diffusion coefficient for <i>n</i> -octane, CO ₂ and H ₂ S in graphite pores. The system composition is shown in Table 4.1 | 133 |
| 5.3 | Self-diffusion coefficient for <i>n</i> -octane, CO ₂ and H ₂ S in alumina pores. The system composition is shown in Table 4.1 | 134 |
| A.1 | Intramolecular interaction parameters (Bond) | 140 |
| A.2 | Intramolecular interaction parameters (Angle) | 140 |
| A.3 | Intermolecular interaction parameters | 141 |
| B.1 | Composition of all simulated systems in this work. In all cases, the simulation temperature was 350K | 143 |

Chapter 1

Introduction

The need to meet increasing global energy demand and the depletion of conventional fossil energy necessitate the quest for alternative energy sources. Shale gas and oil, which are unconventional energy sources have received much attention in recent decades as they have the potential to meet the worlds future energy need [1]. Hydrocarbons found in shales are trapped within the shale reservoir, the source rock from which the hydrocarbons are generated. This is due to low permeability of shale and consequently, their recovery becomes impossible by just drilling wells into the shale formations. In order to recover the hydrocarbons trapped within the nano-pores of shale formations, more advanced technology such as horizontal drilling and hydraulic fracturing through injection of fluids at high pressures are required [2]. Based on IUPAC classification, nano-pores are in three categories: micropores ($<2\text{nm}$) , mesopores (2–50 nm) and macropores ($> 50\text{nm}$) [3]. All these pore sizes are present in shales resulting in a wide pore size distribution [4]. Large-scale exploration of shale gas requires better understanding of fluid-rock interactions which influence hydrocarbon sorption, structure and transport.[5] In

hydraulic fracturing, the injected water for stimulating the formation is usually trapped within the formation. Recent study [6] has shown that the recovery of hydraulic fracturing water is low during flow back operations and that signifies that large volume of the injected water is trapped within the sub-surface formation. Consequently, there is need to better understand the confinement of water and volatile species in narrow pores in order to improve well productivity and hydrocarbon recovery.

Unlike conventional reservoirs, shale formations are characterized by ultra-low permeability, heterogeneity and pore sizes in nanoscale. Properties of fluids confined within these nano-pores show strong deviation from their bulk behaviour.[7–9] In small pores, fluid behaviour is strongly influenced by the solid–fluid interactions which affect the overall thermodynamic, structural and transport properties of confined fluids. The confinement effect on fluid properties needs to be properly understood in order to improve the extraction of geological fluids and other applications such as catalysis [10], separation [11], nano-fluidics [11] and environmental remediation [12]. One property of a fluid that is strongly influenced by confinement is solubility. Several theoretical studies have found enhancement of gas solubility due to confinement [13–17]. For example, Luzar and Bratko [17] found enhanced solubility of oxygen and nitrogen in water by 5–10 folds in hydrophobic nanopores of $\sim 4\text{nm}$. Experimental observations have also confirmed enhanced gas solubility due to confinement.[18, 19] Rakotavao et al. [19] observed tremendous increase in the solubility of hydrogen in n-hexane and ethanol confined in mesoporous silica aerogel.

There has been extensive studies on the behaviour of fluids under confinement [13–17, 20]. Most studies focus on fluid molecules such as methane (CH_4), carbon dioxide (CO_2) and other volatile hydrocarbons. To contribute to this field, in **Chapter 3**, MD simulations were conducted to study the solubility, structural and dynamical properties of aqueous H_2S confined in silica pores of different sizes. H_2S is chosen because of its high toxicity, corrosiveness [21], ability to form clathrate hydrates [22, 23] which can block oil pipelines and catalyst deactivation property [24, 25]. A previous study [26] reported that H_2S permeates hydrated silica pore faster than methane. This thesis investigates the mechanism responsible for higher permeation of H_2S through hydrated silica pore compared to CH_4 .

The growing concern about greenhouse gas emission has stimulated research into developing new technologies for mitigating air emissions. In recent times, CO_2 injection into geological formations for sequestration and enhanced oil recovery (EOR) has been receiving attention [27, 28]. The EOR methods commonly used to produce oil and gas from shale and tight oil are water injection, gas injection and surfactant injection. Gas injection is preferred in EOR because it gives higher recovery compared to water flooding [29]. The CO_2 potential for enhanced hydrocarbon recovery is due to its preferential adsorption close to the surface of the rock materials [30–32] and its dissolution in the oil resulting in viscosity reduction and swelling of the oil [33–35]. Most research on EOR via gas injection focussed on CO_2 injection because it is often coupled with CO_2 sequestration into geological formation. The injection of pure H_2S or mixture of CO_2 and H_2S is investigated in this thesis. There have been theoretical studies on enhancement of hydrocarbon

recovery via CO₂ injection [31, 32, 36–39] as well as experiments [40–44]. Zhang and Cao [38] studied CH₄ and CO₂ in a shale matrix to investigate CH₄ displacement by CO₂ injection at different pore sizes and found that the amount of CH₄ displaced and CO₂ sequestered increased with pore size. Sun et al. [45] investigated adsorption and diffusion of CH₄ and CO₂ in montmorillonite nanopores and observed stronger interaction of CO₂ with the pore surface resulting in its slower diffusion. To complement these efforts, in **Chapter 4**, MD simulations were performed to investigate *n*-butane recovery via acid gas (CO₂, H₂S) injection in silica, muscovite and MgO. This Chapter focuses on the behaviour of *n*-butane and the injected acid gases at the fluid–solid interfaces. Because the substrates considered in **Chapter 4** are inorganic, and the results depend on fluid–surface interactions, simulations were then conducted in alumina (inorganic) and graphite pores to better understand the role of competitive adsorption on hydrocarbon recovery via gas injection. The results are reported in **Chapter 5** of this thesis.

Molecular simulation is a powerful tool that provides detailed molecular–level information about the behaviour of fluid molecules confined within nanopores of materials found beneath the earth at conditions that may not be accessed through experimental studies in the laboratory. The development of this tool has been made possible through rapid technological advancement in the last decades. However, molecular simulation results still require validation against experiments for them to be reliable. This thesis seeks to gain fundamental insights into fluid behaviour in sub-surface environments in nano-scale by conducting molecular dynamics (MD) simulations in order to improve processes such as gas separation and

hydrocarbon production.

In summary, the thesis is organized as follows: In **Chapter 2**, simulation models and methodology are explained in detail. These include: Force fields and algorithms, MD basics and techniques for result analysis.

In **Chapter 3**, MD simulation results for aqueous H₂S confined in silica pores are reported. Effect of confinement on the solubility of H₂S in water as well as structural (molecular density profiles, molecular orientation, spatial distribution function (SDF), radial distribution function (RDF), in-plane distribution) and dynamical (diffusion coefficient, rotational dynamics, residence times) properties of the confined fluids are reported. The effects of pore width on solubility, structural and dynamical properties are also investigated.

In **Chapter 4**, MD simulation results on *n*-butane displacement due to H₂S and CO₂ injection are reported. The amount of *n*-butane displaced from the surface, surface-fluid interaction energies, residence times, and diffusion coefficients are reported. The effects of pore chemistry on the performance of the gas are also documented.

Chapter 5 documents the study that complements the results reported in **Chapter 4**. In this Chapter, graphite and alumina substrates were simulated in order to access the effect of competitive adsorption on gas-based EOR. In **Chapter 6**, detailed conclusions about the work herein and the future outlook are reported.

Chapter 2

Simulation Models and Methodology

2.1 Molecular Dynamics Simulation

Molecular Dynamics (MD) simulation techniques are used throughout for the work reported in this thesis. Computational details and algorithms used are presented in this section of the thesis.

2.1.1 Background

Molecular dynamics simulation methods are used extensively to obtain information on the temporal evolution of systems in phase space giving rise to the trajectory from which useful information can be extracted. MD simulations can be used to study different properties of materials such as interfacial properties, dynamical and structural properties of a fluid which when the right force field is used, give

useful molecular-level information that is difficult or inaccessible through experimental studies[46]. However, predictions via molecular dynamics simulations rely on experimental data for validation. The temporal evolution of the system is obtained by solving the Newtons equations of motion numerically with the positions and velocities of the molecules written in trajectory files from which macroscopic properties of interest can be obtained using the knowledge of statistical mechanics. Given the potential energy function $U(r_{ij})$, the force acting on a particle due to the interaction with its neighbours can be obtained as the negative of the derivative of the potential energy function given in Equation 2.1. Hence, Newtons equation of motion for N particles can be written as Equation 2.2:

$$\vec{F}_{ij} = -\nabla_{r_{ij}}U(\vec{r}_{ij}) \quad (2.1)$$

$$\sum_{i \neq j}^N \vec{F}_{ij} = m_i \frac{d^2 \vec{r}}{dt^2} \quad (2.2)$$

In Equation 2.1 and 2.2, $U(\vec{r}_{ij})$ is the potential energy function, \vec{F}_{ij} is the force acting on atom i due to presence of atom j , N is the total number of atoms in the system, m_i and \vec{r}_i are the mass and position of atom i respectively, and t is time. Macroscopic properties are extracted from the trajectory when equilibrium

is attained. This is a state of minimum energy where properties of the system such as temperature, pressure and density fluctuate about their mean values.

2.1.2 Force fields

A force field is a collection of parameters and mathematical equations that describe the interaction between atoms in a molecular system from which the potential energy of interaction is computed. The basic form of potential energy includes bonded interaction terms and non-bonded interaction terms. The bonded interaction terms describe the interaction between molecules that are covalently bonded and the non-bonded terms describe both the long-range electrostatic forces and van der Waals forces. The general form of the interaction energy is additive and is given by Equation 2.3:

$$E = E_b + E_a + E_{pd} + E_{imd} + E_{coul} + E_{VDW} \quad (2.3)$$

The bonded interaction energies are the bond stretching, angle bending, proper dihedral and improper dihedral terms. The bond stretching and angle bending terms describe the energy of deformation of the bond length and angle respectively and are expressed as harmonic potential described as Equations 2.4 and 2.5:

$$E_b = \frac{1}{2} \sum_{bonds} K_b (r_{ij} - r_0)^2 \quad (2.4)$$

$$E_a = \frac{1}{2} \sum_{\text{angles}} K_\theta (\theta_{ijk} - \theta_0)^2 \quad (2.5)$$

r_0 , θ_0 , K_b and K_θ in Equations 2.4 and 2.5 represent the equilibrium bond length, equilibrium bond angle, bond strength and angle strength respectively. r_{ij} is the bond length between atom i and j while θ_{ijk} is the angle formed by atoms i , j and k . For molecules with more than three atoms, there is contribution of torsion to the total energy of the system. These include proper and improper dihedral energies expressed as Equation 2.6 and 2.7 respectively:

$$E_{\text{proper}} = \frac{1}{2} [c_1(1 + \cos(\phi)) - c_2(1 + \cos(2\phi)) + c_3(1 + \cos(3\phi)) - c_4(1 + \cos(4\phi))] \quad (2.6)$$

$$E_{\text{improper}} = \sum_{\text{improper}} K_\psi (\psi_{ijkl} - \psi_0)^2 \quad (2.7)$$

ϕ is the angle formed between the planes formed by atoms i , j , k and l , c_1 , c_2 , c_3 , and c_4 are dihedral coefficients. K_ψ and ψ are improper dihedral coefficient and improper dihedral angle respectively. The non-bond interaction is usually modelled as a combination of van der Waals potential and coulombic potential. The van der Waal potential comprises dispersive and repulsive interactions between atoms i and j separated by distance r_{ij} . A common form of this potential is the 12-6 Lennard Jones (LJ) potential expressed as Equation 2.8:

$$U_{ij} = 4\epsilon_{ij} \left[\left(\frac{\sigma_{ij}}{r_{ij}} \right)^{12} - \left(\frac{\sigma_{ij}}{r_{ij}} \right)^6 \right] \quad (2.8)$$

Where ϵ_{ij} and σ_{ij} represent well depth and distance at zero potential energy respectively. ϵ_{ij} and σ_{ij} for unlike atoms are determined using Lorentz-Berthelot combination rules [47] given in Equations 2.9 and 2.10:

$$\sigma_{ij} = \frac{(\sigma_{ii} + \sigma_{jj})}{2} \quad (2.9)$$

$$\epsilon_{ij} = \sqrt{(\epsilon_{ii}\epsilon_{jj})} \quad (2.10)$$

The coulombic potential describes the interaction between two charged particles i and j with partial charges q_i and q_j and it is expressed as Equation 2.11:

$$E_{coul} = f \frac{(q_i q_j)}{(\epsilon_r r_{ij})} \quad (2.11)$$

Where $f = \frac{1}{4\pi\epsilon_0}$, and is referred to as Coulombs constant, ϵ_0 is the permittivity of free space and ϵ_r is relative permittivity. In the work reported here, CLAYFF force field [48] was used to model silica, muscovite, MgO and alumina, the Transferable

Potentials for Phase Equilibria (TraPPE-UA) [49] to describe *n*-butane and *n*-octane. CO₂ was described using TraPPE and EPM2 [50] force fields. SPC/E model was used to describe water and the model developed by Kamath and Potoff [51] to describe H₂S. Nitrogen (N₂) was described as a single LJ sphere without coulombic interactions.[52] The CLAYFF force field is a general model that has been used extensively to describe hydrated and multi-component mineral surfaces [11, 13, 26, 32]. In the CLAYFF model implemented in this work, all atoms are fixed except the surface hydroxyl groups of silica and alumina, and surface potassium atoms of muscovite which were allowed to vibrate. This model has been validated against experiments for structure of oxides, oxyhydroxides and hydroxides [48]. In the TraPPE force field, CO₂ is rigid with all atoms on a straight line forming a bond angle of 180°. *N*-butane is a flexible molecule described by angle bending and dihedrals. The united-atom (UA) formalism was implemented in describing the -CH₃ and -CH₂ groups of the *n*-butane. The SPC/E model is chosen to simulate water as it has been found to reproduce radial distribution function of water at ambient conditions. SPC/E is a rigid water model consisting of three interaction sites in which the distance between the oxygen atom and each of the hydrogen atoms is set to 1Å and the H–O–H angle set to the tetrahedral angle (109.47°). Charges are located at oxygen and hydrogen atoms in a proportion that ensures that the molecule is neutral, and the oxygen atom is a Lennard-Jones site. The H₂S model is a three-site model similar to that of Jorgensen [53]. Charges are placed on sulphur and the hydrogen with a fixed bond of length 1.34Å between the sulphur and the hydrogen. The H-S-H bond angle is set to an equilibrium value of 92.5° with angle bending described by harmonic potential. Dispersive

interactions are represented by single Lennard-Jones site placed on the sulphur atom. The hydrogen atoms are not described by dispersive interactions. The model parameters for all molecules are presented in Tables A.1 – A.3 of Appendix A.

2.1.3 Algorithms

In MD simulation, the evolution of the system of interest requires solving Newtons equations of motion for N particles interacting with each other via the specified potential. This exercise is non-trivial as there are $6N$ degrees of freedom involved and no analytical route is possible. Therefore, the equations of motion for the N -particle system are solved numerically. There are various numerical schemes available for the integration of Newtons equations of motion, examples of such numerical methods are verlet, velocity-verlet and leap frog algorithms. The leap frog algorithm is used in all simulations reported in this thesis.

In leap frog algorithm, the equations for obtaining the position and velocity at time $(t + \Delta t)$ are expressed as Equations 2.12 and 2.13 respectively:

$$\vec{r}(t + \Delta t) = \vec{r}(t) + \vec{v}(t + \frac{1}{2}\Delta t)\delta t \quad (2.12)$$

$$\vec{v}(t + \frac{1}{2}\Delta t) = \vec{v}(t - \frac{1}{2}\Delta t) + \vec{F}(t)\frac{\delta t}{m} \quad (2.13)$$

In this algorithm, velocities are first calculated at time $(t + \frac{1}{2}\Delta t)$ which are then

used to obtain the positions at time $(t + \Delta t)$. Hence, velocities leap over positions while positions leap over velocities. The use of leap-frog algorithm does not allow the calculation of velocities at time t . However, these can be obtained through an approximation that involves an average of the velocities at $(t + \frac{1}{2}\Delta t)$ and $(t - \frac{1}{2}\Delta t)$ as shown in Equation 2.14:

$$\vec{v}(t) = \frac{1}{2}[\vec{v}(t + \frac{1}{2}\Delta t) + \vec{v}(t - \frac{1}{2}\Delta t)] \quad (2.14)$$

When using this algorithm, the time step for the integration should be small enough to ensure energy conservation. The time step used in all simulations reported here is 1fs.

2.1.4 Periodic boundary condition

In order to simulate a bulk system of fluid in a simulation box, periodic boundary condition (PBC) is usually employed. PBC removes surface effect which any finite system will have and ensures that the internal structure of the fluid is dominated by bulk forces rather than surface forces. The implementation of PBC makes it possible to simulate bulk fluids and remove surface forces exerted by the surface molecules if PBC is not used. PBC ensures that the number of molecules in the simulation box remains unchanged as a molecule that leaves the simulation box re-enters from the opposite end of the box. When PBC is applied on a system, the unit cell is replicated throughout the space to form an infinite number of unit cells as shown in **Figure 2.1**. The periodic cells contain atoms whose positions combine

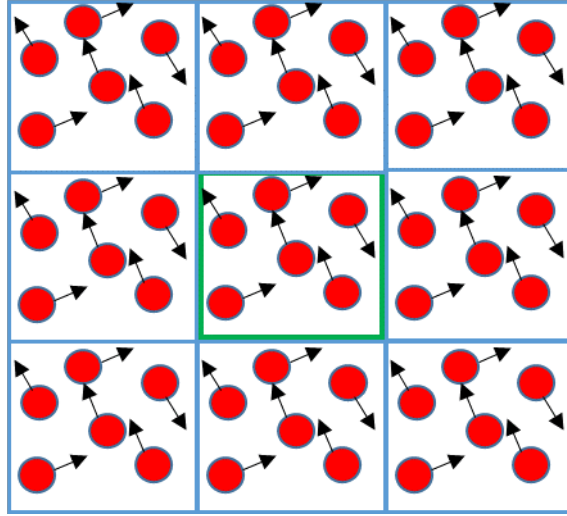


FIGURE 2.1: Periodic boundary conditions. The unit cell is enclosed in green

the position of the atom in the unit cell and a translational position vector defined by Equation 2.15:

$$\vec{R} = n_1 a + n_2 b + n_3 c \quad (2.15)$$

Where a , b , and c are vectors corresponding to the edges of the box and n_1 , n_2 and n_3 are any integers. The position of the image of atom i is expressed as Equation 2.16:

$$\vec{r}_i^{image} = \vec{r}_i + \vec{R} \quad (2.16)$$

All periodic images have the same momentum as the corresponding atom in the unit cell and is given in Equation 2.17

$$P_i^{image}(n_1, n_2, n_3) = P_i = m_i v_i \quad (2.17)$$

The estimation of the interaction potential between atom i and every other atom in the simulation cell assuming pair additivity involves $N(N-1)$ terms. In principle, the interaction with atoms in the periodic cells (images of atoms in the simulation cell) has to be included. This is computationally expensive and therefore, an approximation is required. The approximation usually employed is the minimum image convention where an atom interacts with the closest images of other atoms in the simulation cell. The number of terms involved in the calculation of the potential assuming pair additivity then reduces to $\frac{1}{2}N(N-1)$ but the calculation is still computationally expensive. A further approximation is made using a spherical cut-off where interaction between atoms whose separation is greater than the cut-off distance (r_c) is not included in the potential energy calculation. This means that atom i experiences a force due to its interaction with atom j or only one of its images.

2.1.5 Thermostat

The use of thermostat in MD simulations is very crucial as this helps to explore ensembles other than the Microcanonical ensemble (NVE) and allows comparison with experimental data as experiments are usually performed at constant temperature and pressure. To achieve this comparison, canonical ensemble (NVT) or isothermal-isobaric ensemble (NPT) may be desirable. To simulate in NPT ensemble, a barostat is used in addition to the thermostat to keep the pressure close to the desired value. The use of thermostat in MD simulation ensures that the temperature stays within the set value and also prevents long term energy drift

that may arise as a result of numerical integration errors. A number of thermostats have been proposed, each utilizing different approaches. However, we must always consider whether the chosen approach gives the correct microstate distribution and realistic dynamic behaviour in the chosen ensemble such that the equations of motion yield accurate properties of the system. The common thermostats used in MD simulation include velocity rescaling, Anderson, Berendsen and Nosé–Hoover thermostats.

2.1.5.1 Velocity rescaling

In velocity rescaling, the velocities of the molecules in the system are rescaled at each step (or after a pre-set number of steps) in order to drive the system temperature to the desired value. This is done by multiplying the velocities with a scaling factor λ , such that Equation 2.18 holds. The scaling factor λ is simply the square root of the ratio of the desired temperature to the instantaneous temperature of the system.

$$V_{new}^N = \lambda V^N \quad (2.18)$$

Where $\lambda = \sqrt{\frac{T}{T_{inst}}}$, V_{new} , V , T , T_{inst} and N are the new velocity, old velocity, target temperature, instantaneous temperature and number of particles respectively. Velocity rescaling does not generate correct thermodynamics of the canonical ensemble as it allows no fluctuation in the kinetic energy of the system. This is unrealistic from statistical mechanics point of view [54].

2.1.5.2 Berendsen Thermostat

Berendsen thermostat [55] approach is similar to velocity rescaling as both involve scaling the temperature as the simulation progresses. When using Berendsen approach, the system is assumed to be weakly coupled to a heat bath and there is a time scale associated with the update of the velocities. The scaling factor λ , depends on the coupling constant τ , according to Equation 2.19:

$$\lambda = 1 + \frac{\delta t}{\tau} \left(\frac{T}{T_{inst}} - 1 \right)^{\frac{1}{2}} \quad (2.19)$$

Where δt is the time step in the MD simulation. This thermostat does not also preserve the energy fluctuation in the simulation

2.1.5.3 Anderson Thermostat

In Anderson thermostat, temperature control is through stochastic collision of randomly selected particles with a heat bath at the target temperature. When single-particle approach is used, a particle is selected randomly and its velocity is re-assigned from the Maxwell-Boltzmann distribution at the target temperature. In this scheme, the strength of the coupling to the heat bath is chosen, and this is a function of the frequency of collision of the selected particle with the heat bath. [56] Anderson thermostat generates a canonical distribution but there is decorrelation of particle velocities and as a result does not preserve molecular kinetics. Transport property computed from the trajectory generated using this thermostat is unrealistic.

2.1.5.4 Nosé–Hoover

Nosé–Hoover [57, 58] is considered the most accurate of the thermostats mentioned as it gives correct canonical ensemble which yields accurate structural and dynamical properties of system of interest. Temperature control in Nosé–Hoover thermostat involves modification of the equation of motion by introducing a friction parameter through which the motion of particles is controlled until the system temperature, T approaches the target value T_0 . The modified equation of motion is expressed as Equation 2.20: [56]:

$$\frac{d^2 \vec{r}_i}{dt^2} = \frac{F_i}{m_i} - \frac{P\xi}{Q} \frac{d\vec{r}_i}{dt} \quad (2.20)$$

Where ξ is the friction factor that controls the motion of particles so that temperature T approaches the set value T_0 . The parameter Q , controls the friction dynamics and P is the particle momentum.

2.2 Statistical mechanics and molecular simulation

Molecular dynamics (MD) simulation gives detailed information about the evolution of a microscopic system. Computation of macroscopic properties from MD trajectories requires the application of statistical mechanics. The application of

statistical mechanics in molecular simulations provides a theoretical framework which makes it possible to predict average properties of a system using statistical tools (such as probability, averages and deviations). In statistical mechanics, the collection of all possible configurations a system can be in that is consistent with an imposed constraint (such as temperature, pressure, number of particles) gives rise to a statistical ensemble. The total number of ways a system can be prepared that is consistent with the constraints is referred to as the *partition function*. Once the partition function of a system is known, all thermodynamic properties of the system can be calculated.

2.2.1 Ensemble

A statistical ensemble is a collection of different possible representation of a system. It is a probability distribution for the state of a system and comprises of virtual copies of the system of interest each possessing the same macroscopic properties but differ microscopically. An ensemble is usually defined given certain constraints on the system. The constraint variable could be number of particles in a simulation box, volume of the box, total energy of the system, temperature, pressure and chemical potential. A system which has fixed number of particles, volume and energy is said to be in micro-canonical (NVE) ensemble. NVE is the foundation on which other ensembles are built. Since it is much easier to keep temperature constant rather than energy, canonical ensemble where number of particles, volume and temperature (NVT) are kept constant becomes very useful. Experiments are usually performed at constant temperature and pressure, therefore, it is imperative

to impose constraints which make comparison with experimental data possible. NPT ensemble then becomes an option to achieve this purpose. Another ensemble that is used for simulating phase transitions is the Grand canonical ensemble where volume, temperature and chemical potential are kept constant.

In molecular dynamic simulation, thermodynamic properties are obtained as averages over successive configurations generated from the simulation by numerical integration of Newtons equation of motion for every time step. The calculation of these averages has been made possible as a result of an assumption that averages calculated over multiple realization of a system is the same as time averages obtained from MD trajectories. This assumption is referred to as *Ergodic hypothesis*. Ergodicity can be achieved when the system is allowed to evolve for a long period of time. A system which can sample all possible configurations in phase space when allowed to evolved for a long time is said to be *ergodic*.

In this ensemble, the number of particles (N), volume (V), and temperature (T) of the system are kept constant. The system temperature is maintained at the desired value with the aid of a thermostat through which the system is coupled to a heat bath with which it can exchange energy. The average energy of the system is obtained from the energy of each microstate, m and is given by Equation 2.21:

$$\langle E \rangle = \sum_{m=1}^{\omega} P(m) E_m \quad (2.21)$$

$\langle E \rangle$ is the average energy, $P(m)$ is the probability of observing state m , E_m is the energy of state m and ω is the total number of possible states. The probability

TABLE 2.1: Partition function of common ensembles

| Ensemble | Imposed constraints | Partition function |
|---------------------|---------------------|---|
| Canonical | N, V, T | $\sum_{m=1}^{\omega} \exp(-\beta U_m)$ |
| Isothermal-Isobaric | N, P, T | $\sum_{m=1}^{\omega} \exp(-\beta U_m - \beta PV)$ |
| Grand canonical | μ, V, T | $\sum_{m=1}^{\omega} \exp(-\beta U_m + \sum_i N_i \mu_i)$ |

of observing a state can be computed if the partition function is known. The partition function of the canonical ensemble Z_{NVT} , is the sum over all possible states of the Boltzmann factor expressed in Equation 2.22:

$$Z_{NVT} = \sum_{m=1}^{\omega} \exp(-\beta E_m) \quad (2.22)$$

Where $\beta = \frac{1}{K_b T}$, K_b is Boltzmanns constant. Partition function of common ensembles are presented in **Table 2.1** with U_m as internal energy of state m , V as volume, μ as chemical potential, P as pressure and N as number of particles.

2.3 Techniques for result analysis

Statistical averages of macroscopic properties can be computed from MD trajectories. These include thermodynamic properties (such as temperature and pressure), transport properties (such as diffusion coefficient) and structural properties (such as radial distribution function and structure factor). These properties are estimated as ensemble averages from MD simulations.

2.3.1 Radial distribution function (RDF)

The radial distribution function (also called pair correlation function) is a probability distribution function that shows how molecules are radially packed around a reference molecule. It describes how density varies with the radial distance from the reference molecule. RDF is commonly used for describing the structure of fluids and solids in material science. The computation of RDF involves determining the number of particles that can be found within a distance r and $r + \delta r$ from a reference particle and a histogram of the particles is constructed. RDF gives information about the relative probability of finding atom i in the vicinity of j at separation distance r . The running integral of RDF is the number of atoms j in a sphere of specified radius r around atom i . The radial distribution function of a system of N molecules can be computed using Equation 2.23:

$$g(r) = \frac{\rho(r)}{\rho} \quad (2.23)$$

Where $\rho(r)$ is the local density at a distance r from a reference atom, ρ is the system average bulk density. The local density is calculated from the ratio of the number of molecules or atoms whose centre lie within a spherical shell of radius δr at a distance r from the reference molecule or atom, to the volume of the shell $\rho(r) = \frac{n(r)}{4\pi r^2 \delta r}$. The global density (average bulk density of the system) is obtained as ($\rho = N/V$). A typical RDF of a liquid is shown in **Figure 2.2**

The RDF of a solid has peaks whose heights and separations give information about the lattice structure. In a liquid, RDF is characterised by peaks at short distances

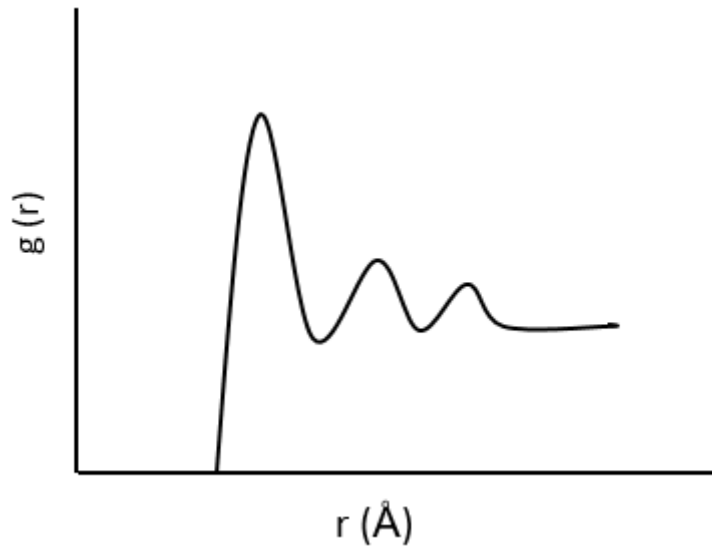


FIGURE 2.2: Radial distribution function of a liquid

which decay to a steady value (usually one) at long separations. The position of the first peak corresponds to the location of the first coordination shell and that of the second peak locates the second coordination shell. The coordination number in the first shell is estimated as the integral of RDF up to the first minimum.

2.3.2 Mean Square Displacement (MSD)

The translational dynamics of a condensed fluid or gaseous system is usually quantified in terms of diffusion coefficient. In MD simulation, diffusion coefficient can be obtained from a numerical implementation of Einstein relation [59] where the diffusion coefficient is obtained from the long time limit gradient of a plot of the mean square displacement (MSD) as a function of time. The MSD is expressed as Equation 2.24:

$$MSD(t) = \langle |r(t) - r(0)|^2 \rangle \quad (2.24)$$

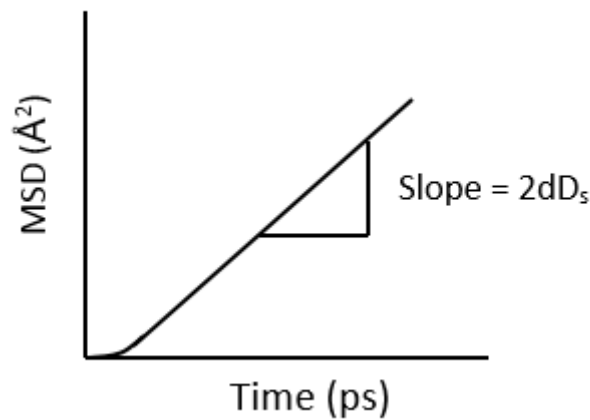


FIGURE 2.3: MSD plot showing ballistic and diffusive regimes

Albert Einstein related MSD to the self diffusion coefficient D_s , according to the relation given in Equation 2.25:

$$D_s = \lim_{t \rightarrow \infty} \frac{1}{2dt} \langle |r(t) - r(0)|^2 \rangle \quad (2.25)$$

d in Equation 2.25 is the dimensionality of the system. For a 2D MDS, d is equal to 2, and equal to 3 for a 3D system. A typical MSD plot is shown in **Figure 2.3**. At very short time, MSD plot is non-linear because the motion of a particle does not resemble a random walk until it collides with its neighbours and the distance covered is proportional to the square of the time taken. This region is known as the ballistic regime and the MSD is parabolic. At longer times, MSD becomes proportional to time and the plot approximates a straight line. This region is the diffusive regime. The diffusion coefficient computed from Einstein relation is only reasonable after a long simulation time. Only the linear part of the plot (diffusive regime) is used for the calculation of self-diffusion coefficient with the linear relationship verified by log-log plot of MSD versus time.

2.3.3 Residence Correlation function (RCF)

To quantify how long fluid molecules spend in a specific region in the pore, the residence correlation function, $C_R(t)$ is used. $C_R(t)$ is defined as Equation 2.26

$$C_R(t) = \frac{\langle N_i(t)N_i(0) \rangle}{\langle N_i(0)N_i(0) \rangle} \quad (2.26)$$

In Equation 2.26, $N_i(t) = 1$ if molecule i resides in the layer of interest at time t and 0 otherwise. If molecule i belongs to the layer at time $t = 0$, $N_i(t) = 0$ and remains equal to 1 as long as molecule i stays in the layer; but this quantity becomes 0 when molecule i leaves the layer of interest. $C_R(t)$ decays from 1 to 0. The faster $C_R(t)$ decays to zero, the faster the molecules leave the layer of interest. The dynamics of orientation of a molecule can be studied using the dipole-dipole autocorrelation functions. This can be computed using Equation 2.27:

$$C_{DM}(t) = \frac{\langle M_i(t)M_i(0) \rangle}{\langle M_i(0)M_i(0) \rangle} \quad (2.27)$$

Where $M(0)$ is the dipole moment of molecule i at $t = 0$ and $M(t)$ is the dipole moment of molecule i at time t . As in the case of residence autocorrelation function, if a molecule leaves the layer considered, it does not contribute anymore to the dipole-dipole moment autocorrelation function. The faster $C_{DM}(t)$ falls to zero, the faster the molecule changes its orientation.

2.3.4 Spatial Distribution function

The Spatial distribution function (SDF) quantifies the three-dimensional density distribution of molecules coordinating a specific molecule of interest. SDF is basically RDF presented in 3D and is usually represented as an iso-surface of the density distribution of the coordinating fluid molecules. To calculate SDF, positions of molecules in a specified shell around a reference molecule are extracted from MD trajectories. These coordinates are extracted as volume maps that can be displayed as iso-surfaces.

Chapter 3

Aqueous Hydrogen Sulfide in Slit-Shaped Silica Nanopores: Confinement Effects on Solubility, Structural, and Dynamical Properties

The material presented in this Chapter was published in **2018** in volume 122, pages 14744-14755 of The Journal of Physical Chemistry C

3.1 Abstract

It is known that confinement in nm-size pores affects many structural and transport properties of water and co-existing volatile species. Of particular interest for fluids in sub-surface systems, in catalysis, and in separations are reports that confinement can enhance the solubility of gases in water. Here, equilibrium molecular dynamics simulations for aqueous H₂S confined in slit-shaped silica pores at 313K

are reported. The effect of pore width on H₂S solubility in water, molecular distribution of the various fluid molecules within the pores, the hydration structure for solvated H₂S molecules, and the dynamical properties of the confined fluids were investigated. The simulation results demonstrate that confinement reduces the H₂S solubility in water, and that the solubility increases with pore size. Data analysis suggests that these results are due to perturbations on the coordination of water molecules around H₂S due to confinement. Confinement also dampen the dynamical properties of aqueous H₂S. Comparing the results obtained for aqueous H₂S to those reported elsewhere for aqueous CH₄, it can be concluded that H₂S permeates hydrated slit-shaped silica nano-pores faster than CH₄. These observations could have important implications for developing new natural gas sweetening technologies and contribute to better understanding of fluid behaviour in subsurface formations.

3.2 Introduction

Natural gas is widely considered as a high quality, clean and economical energy source. However, it usually contains undesirable substances such as hydrogen sulphide (H₂S) and carbon dioxide (CO₂). H₂S is of special interest because of its high toxicity, tendency to corrode pipelines and other process equipment, [21] ability to form clathrate hydrates, [22, 23] which can plug pipelines, and its catalyst deactivation property. [24, 25] It has been reported that the occurrence of acid gases including H₂S, as well as CO₂ impurities, strongly affect many subsurface phenomena, including water-rock geochemical reactions with implications

on the optimal strategies for carbon sequestration technologies.[60] The removal of sour gases from natural gas is done industrially by gas-liquid absorption-stripping processes using amine-based compounds, [61] membrane separations,[62] and adsorption. [61, 63] In a theoretical study by Phan et al., [26] it was suggested that hydrated nanopores show large selectivity to H₂S permeation, compared to other typical natural gas components. This Chapter seeks to quantify the molecular mechanisms responsible for the observation of Phan et al. MD simulation results on adsorption and selectivity of H₂S in Metal–Organic Frameworks (MOFs) have also previously been reported in the literature. [64]

Silica-based porous materials are widely used as representative substrates for academic investigations because silica is one of the most abundant materials on Earth. Results from these studies could contribute to improving applications such as separations, [11] nanofluidics, [11] catalysis,[10] environmental remediation, [12] and sub-surface geo-energy, [65]although many investigations focused on structural and dynamical properties of fluids confined in silica nanopores of varying pore size [66] and different morphologies.[11, 32, 67, 68] This Chapter presents results for H₂S as a guest molecule adsorbed in confined water. The structural and dynamical properties of confined water is strongly affected by the confining pore surfaces; [69] and it is expected that the perturbation due to confinement dictates the behaviour of guest molecules adsorbed within the hydrated pore. The solubility of volatile gases in different solvents under confinement is receiving increasing attention. [13–17] Several studies reported enhancement of solubility of gases in liquids confined in small pores, a phenomenon referred to as *oversolubility*. For example,

Luzar and Bratko [17] found enhancement of the solubility of nitrogen (N_2) and oxygen (O_2) in water by 5-10 folds when confined in hydrophobic pores of width 38-43Å. A study by Phan et al. [13] revealed higher solubility of methane (CH_4) in water confined in a partially filled 1nm-wide silica pore. Ho et al.[14] reported enhancement of CO_2 and H_2 uptake in a MCM-41 pore containing octamethylcyclotetrasiloxane (OMCTS). Hu et al. [66] reported oversolubility of CH_4 in confined benzene, and the dependence of such solubility on pore width. Gadikota et al.[20] documented the solubility of CH_4 , CO_2 , and argon (Ar) in water confined in Na-montmorillonite pores. Based on experiments and simulations, these authors reported higher solubility for CO_2 and Ar in confined water compared to bulk water, whereas results obtained for CH_4 suggest that confinement reduces CH_4 solubility. The enhanced solubility of gases under confinement has been confirmed experimentally. [18, 19] Pera-Titus et al. [18] studied the solubility of H_2 in $CHCl_3$, CCl_4 , *n*-hexane, ethanol and water when confined within γ -alumina, silica and MCM-41, and found that H_2 solubility was enhanced by up to 15 times the corresponding bulk value in pores less than 15nm in size. Rakotovao et al. [19] confirmed the results of Pera-Titus et al. using 1H NMR.

According to Ho et al, [14] oversolubility could be due to one, or a combination of the following mechanisms: (i) the solute interacts more strongly with the surface than the solvent, favouring its adsorption close to the pore walls; (ii) the pore is partially filled, resulting in gas/solvent interface which facilitates adsorption of the gas into the solvent-rich phase; and (iii) the solubility follows a confinement-induced mechanism where adsorption of the gas is favored in regions of low solvent

densities generated due to layering of the solvent. A balance between solute-substrate, solvent-substrate, and solvent-solute interactions is expected to dictate the resultant oversolubility. [66] Gadikota et al. [20] showed that solute size and the presence of salt in confined water are also important in modulating the free energy of dissolution of various gases in confined water.

H₂S is chosen in this study because of its polar nature and its relevance to industrial applications. Comparison of the predicted solubility of H₂S in confined water to that predicted for CH₄ discussed elsewhere, [13] will facilitate better understanding of the controlling mechanisms for gas solubility in confined water. The results will also complement those of Gadikota et al., [20] who considered both CH₄ and CO₂, a non-polar compound with large quadrupole, in water confined within montmorillonite pores.

In this study, molecular dynamics (MD) simulations were used to investigate the effect of confinement on the solubility of H₂S in confined water as well as structural and dynamical properties of the confined fluids. The simulations were conducted at 313K and pressures in the range of $\sim 5 - 26$ bar with focus on the comparison of the properties of the confined fluids with that of the bulk.

3.3 Simulation Methods and Algorithms

3.3.1 Simulation set up

3.3.1.1 Pseudo-bulk systems

To calculate the solubility of hydrogen sulphide (H_2S) in water, as well as the interfacial tension (IFT), equilibrium MD simulations were conducted for 2-phase systems in the canonical ensemble (NVT) at 313K. The initial configuration was built by placing a thick slab of 400 water molecules in a simulation box of dimension $19.6\text{\AA} \times 19.6\text{\AA} \times 30\text{\AA}$. The water slab was first equilibrated in canonical ensemble for 1ns and then centred in a tetragonal periodic cell of $19.6\text{\AA} \times 19.6\text{\AA} \times 90\text{\AA}$, where it was allowed to come in contact with H_2S vapour. H_2S molecules were placed in the vapour phase on both sides of the water slab as shown in 3.1a. The simulation set up is similar to what has been described in previous studies. [70, 71] The number of H_2S molecules was varied to manipulate the pressure of the system while keeping the number of water molecules constant. The pressure of the system was calculated from H_2S density above the water slab using the Peng-Robinson equation of state. [72] Note that the density of water in the gas phase is low compared to that of H_2S (vapour pressure of H_2O at 313K is 0.073bar) and is not used for the bulk system pressure calculation. The compositions of the systems simulated and the corresponding bulk pressures are shown in Table 3.1. To study the solvation of H_2S in bulk liquid water additional simulations were conducted for bulk systems without interfaces in the canonical ensemble (NVT). The composition for these simulations was taken from the solubility simulations.

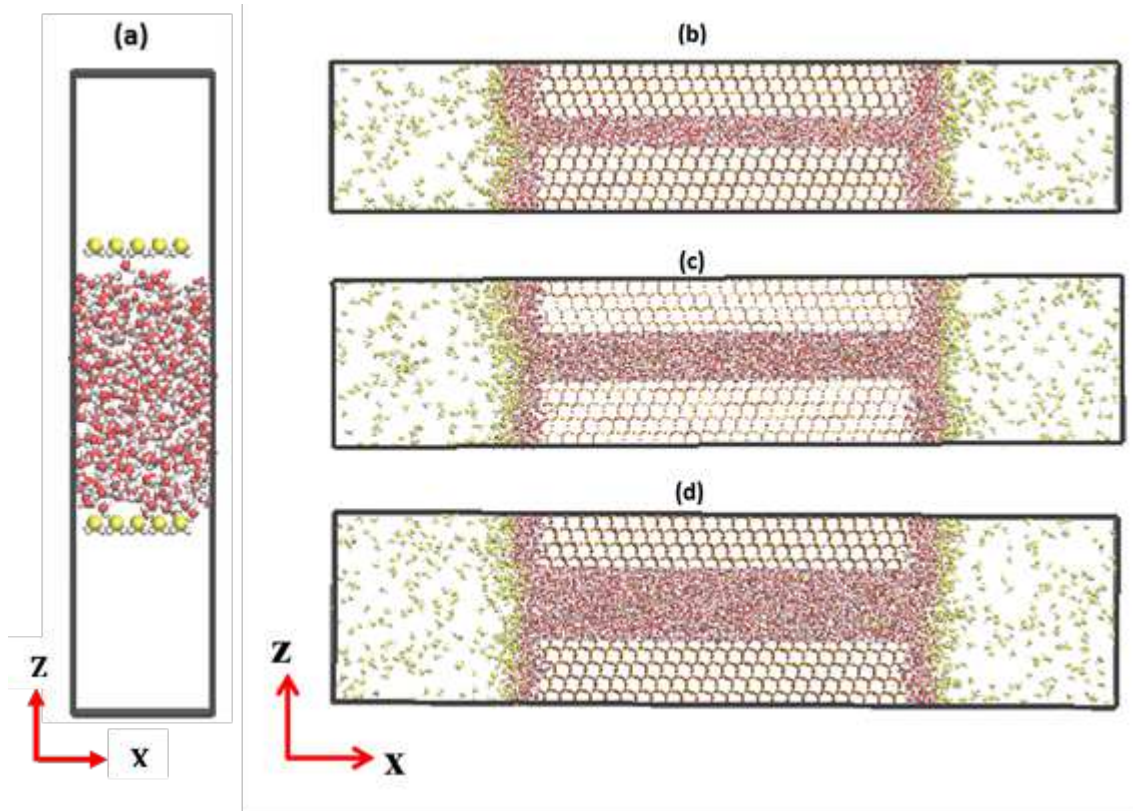


FIGURE 3.1: Initial configuration for the pseudo-bulk simulation containing 400 molecules of water and 40 molecules of H_2S is shown in the panel (a). Simulation snapshots of the simulated pores are shown in panels (b–d). The pore widths are (b) 1, (c) 1.49, and (d) 2.2 nm. For the fluid molecules, oxygen atoms are shown in red, sulfur atoms in yellow, and hydrogen atoms in white

TABLE 3.1: Composition and bulk pressure for the 2-phase systems

| System (Bulk) | Composition (molecules) | Bulk Pressure (bar) |
|---------------|--|---------------------|
| 1 | $8\text{H}_2\text{S}-400\text{H}_2\text{O}$ | 5.5 ± 0.5 |
| 2 | $18\text{H}_2\text{S}-400\text{H}_2\text{O}$ | 10.9 ± 0.7 |
| 3 | $24\text{H}_2\text{S}-400\text{H}_2\text{O}$ | 14.0 ± 0.3 |
| 4 | $32\text{H}_2\text{S}-400\text{H}_2\text{O}$ | 18.9 ± 0.7 |
| 5 | $40\text{H}_2\text{S}-400\text{H}_2\text{O}$ | 22.6 ± 0.6 |

The simulation box was cubic with size of $40\text{\AA} \times 40\text{\AA} \times 40\text{\AA}$, and periodic boundary conditions were implemented in all directions.

3.3.1.2 Confined system

The silica substrates used in this study were obtained from β -cristobalite SiO_2 by cutting the crystal along the (1 1 1) crystallographic plane. By placing two silica slabs parallel to each other with a separation distance d (i.e., the pore width), the slit-shaped pores were created. The distance d is the shortest center-to-center distance between the oxygen atoms of the -OH groups on the silica surface measured across the pore volume along the Z-direction. Consistent with low pH conditions, all non-bridging oxygen atoms of silica were protonated, resulting in -OH surface density of 4.54 per square nanometer. This is in reasonable agreement with experiments.[68] Each silica slab is parallel to the X-Y plane of the simulation box and has dimensions of $104.05 \times 100.8 \text{ \AA}^2$. Atoms of the silica slabs were kept fixed throughout the simulation except the hydrogen atoms on the surface, which were allowed to vibrate. The X and Y dimensions of the simulation box remain constant for all simulations at 224.78 \AA and 100.8 \AA , respectively, while the Z dimension changes depending on the pore width. The Z dimensions of the simulation box are 42.92 \AA , 47.80 \AA and 54.92 \AA for 1nm, 1.49nm and 2.2nm pores, respectively. The simulation box is periodic in X, Y and Z directions, but the silica slabs are only periodic along the Y direction as they are exposed to two bulk regions along the X direction (see Figures 3.1b - d). The simulation setup is similar to the one implemented in previous studies. [13, 73] The initial configuration for the 1.0 nm-wide pore was obtained by first placing 6,000 water molecules in the unconfined region of the simulation box. A simulation was then conducted for 3 ns to allow the water molecules to adsorb within the pore. The 6,000 water molecules fully fill

the 1nm pore and yield a thin water film near the pore entrances. H₂S molecules were then placed in the unconfined space (bulk) on both sides of the silica pore. As the simulation progresses, H₂S molecules exchange between the hydrated pore and the bulk. At equilibrium, some H₂S are adsorbed in the pore while the remaining H₂S molecules occupy the bulk region as shown in Figure 3.1b. The bulk pressure of the system was estimated from the H₂S density in the bulk region calculated along the X-direction using the Peng-Robinson equation of state. [72]. The density profile in X-direction for the 1nm pore is shown in Figure 3.2. The errors in the estimated bulk pressure are due to fluctuation of H₂S density in the bulk region. The H₂S solubility was calculated from the composition of water and H₂S in the pore. The pressure of the system was manipulated by changing the number of H₂S molecules in the bulk region. The same procedures were followed to study the effect of pores size on the results. The composition of the simulated systems and the corresponding bulk pressures are shown in Table 3.2 - 3.4.

3.3.2 Force fields

The rigid SPC/E model was used to describe water as it gives reasonable estimates for structure, density, and diffusion coefficient of liquid water under ambient conditions. [74] The model developed by Kamath and Potoff was used to describe H₂S. [51] The CLAYFF [48] force field was implemented to model the silica slabs. CLAYFF is a general force field widely used for simulating fluids interacting with clay and clay-related substrates. Nonbonded interactions were modeled by dispersive and electrostatic interactions. The dispersive interactions were described by

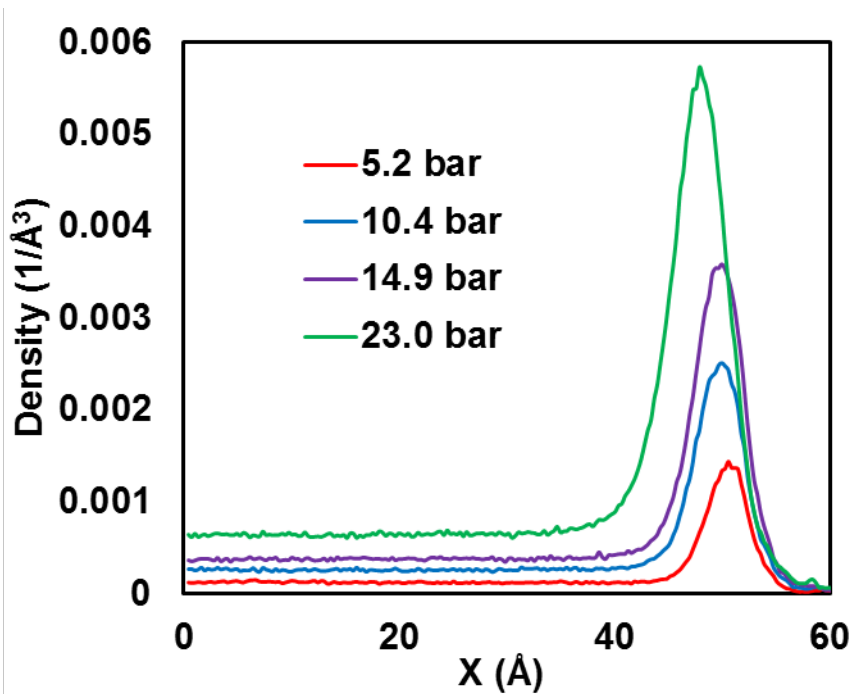


FIGURE 3.2: Density profiles of H₂S in X-direction at different H₂S loadings for 1nm pore.

TABLE 3.2: Confined system composition with corresponding bulk pressure for 1nm pore

| H ₂ S-H ₂ O composition | Bulk Pressure (bar) |
|---|---------------------|
| 120-6000 | 5.2 ± 0.1 |
| 240-6000 | 10.4 ± 0.2 |
| 360-6000 | 14.9 ± 0.3 |
| 600-6000 | 23.0 ± 0.4 |

the 12-6 Lennard Jones (LJ) potential and the electrostatic interactions were described by the Coulombic potential. The Lorentz-Berthelot combination rules [47] were used to calculate LJ parameters for unlike atoms. The cutoff distance for all interactions was set to 9 Å. The long-range corrections to electrostatic interactions were implemented using the particle mesh Ewald method.[75]

TABLE 3.3: System composition for 1.49nm pore with corresponding bulk pressure

| Composition H ₂ S-H ₂ O | Bulk Pressure (bar) |
|---|---------------------|
| 200-7600 | 7.4 ± 0.2 |
| 400-7600 | 14.4 ± 0.3 |
| 600-7600 | 20.5 ± 0.3 |
| 800-7600 | 26.0 ± 0.6 |

TABLE 3.4: System composition for 2.2nm pore with corresponding bulk pressure

| Composition H ₂ S-H ₂ O | Bulk Pressure (bar) |
|---|---------------------|
| 300-10000 | 9.2 ± 0.4 |
| 500-10000 | 14.6 ± 0.3 |
| 700-10000 | 20.1 ± 0.5 |
| 900-10000 | 24.2 ± 0.5 |

3.3.3 Algorithms

All simulations were performed using the simulation package GROMACS version 5.1.2 [76, 77] in the canonical ensemble (NVT). Newtons equations of motion were solved using the leapfrog algorithm. [78] The temperature of the system was maintained at 313 K using the Nosé–Hoover thermostat [57, 58] with a relaxation time of 100 fs. The bonds and angles in H₂O were kept fixed using the SETTLE algorithm. [79] For bulk and pseudo-bulk simulations, each system was equilibrated for 18 ns, followed by a production run of 12 ns conducted for data analysis. For confined systems, simulations were conducted for a total time of 120ns and the last 10ns trajectory was used for analysis. The systems were considered equilibrated when H₂S densities fluctuate around constant values, and the system energy fluctuates within 10% of its average value.

3.4 Results and discussion

3.4.1 Pseudo-bulk systems

The atomic density profiles of water oxygen (OW) and sulfur of H₂S (S) for the 2-phase simulations with compositions shown in Table 3.1 are reported in Figure 3.3. The Z-direction of the simulation box is perpendicular to the liquid water slab. The results are obtained as number density of OW and S. In the gaseous phase, the density is low as expected, whereas in the liquid phase the density is consistent with the density of bulk liquid water at 313K. The solubility of H₂S in bulk water is estimated as the ratio of the average number density of S to the average number density of OW in the liquid slab. The region between points A and B shown in Figure 3.3 was used for the solubility calculation to exclude the two interfaces. The solubility results are reported as a function of pressure in Table 3.5. The uncertainties in the estimated pressures reflect density fluctuations in the gaseous phase and was estimated using block averaging. In Figure 3.4, top panel, comparison of the solubility results against the experimental data reported by Kuranov et al. [80] is shown. It is clear that the force fields implemented here under-estimate the solubility of H₂S in bulk water and the discrepancy increases as the pressure increases. The under-estimation of the solubility in water could be a consequence of the fact that the H₂S force field implemented here was developed for pure H₂S. The mixing rules implemented may not adequately represent the physical interactions between H₂S and water. The solubility results were compared with the experimental data reported by Kuranov et al. [80] as they

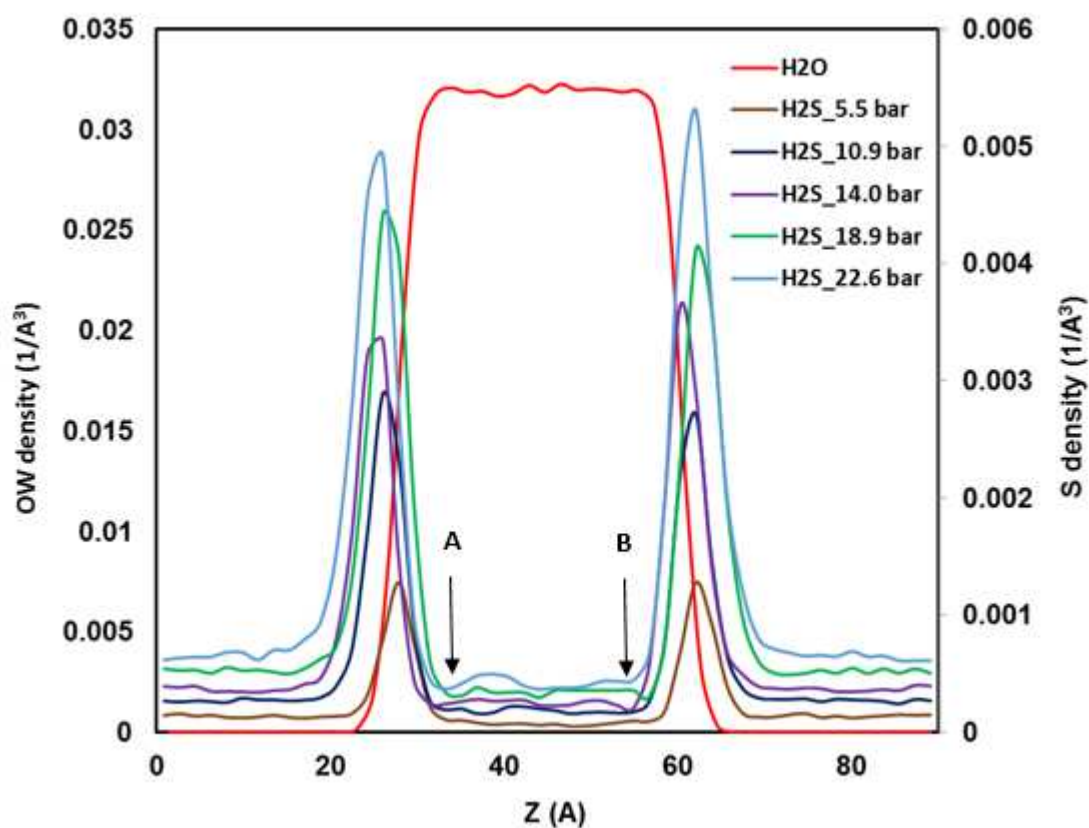


FIGURE 3.3: Density profiles of sulfur of H_2S (S) and oxygen atom of water (OW) along the Z-direction of the simulation box at different bulk pressures. Only one profile is shown for OW because it does not change significantly with pressure.

were obtained at similar thermodynamic conditions as those chosen in this study. Other experimental data at conditions different from those chosen here are also available for H_2S solubility in water. [81–85] While at low to moderate pressure ($P < 5$ bar), there is agreement between experimental results by different groups, [81, 84] the agreement diminishes as pressure increases. For example, Selleck et al. [82] suggested that H_2S solubility in water increases rapidly as pressure increases, whereas Gillespie et al. [85] do not agree with this trend. Rather than attempting to resolve this argument, the simulation results provide benchmark data for H_2S solubility in bulk water to quantify the effect of confinement.

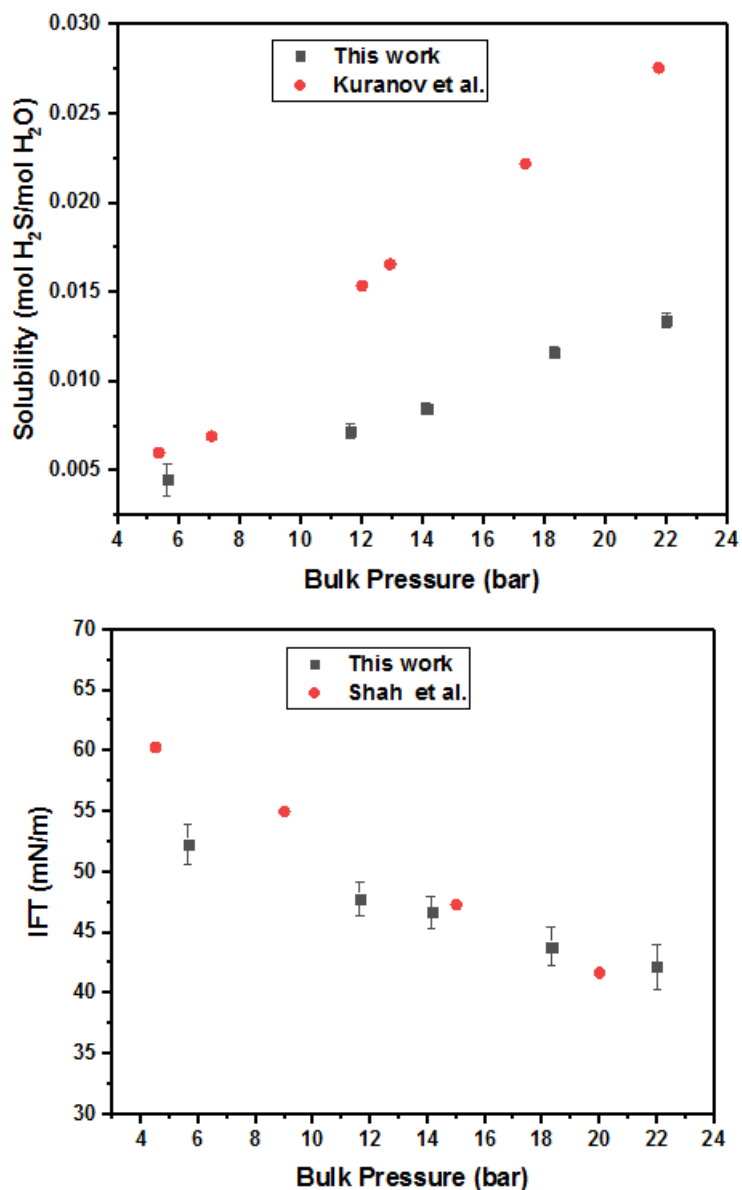


FIGURE 3.4: Comparison of (a) Simulated solubility of H₂S in water compared against the experimental data of Kuranov et al.[80] (b) Simulated water IFT compared against the experimental data of Shah et al.[86] In both cases, the results are shown as a function of H₂S pressure. In the simulations, the errors were estimated as standard deviation from the mean

TABLE 3.5: H₂S solubility in H₂O and H₂O IFT at different bulk pressures

| Bulk pressure (bar) | H ₂ S solubility $\times 10^3$ | IFT (mN/m) |
|---------------------|---|----------------|
| 5.5 ± 0.3 | 4.3 ± 1.1 | 52.1 ± 1.6 |
| 10.9 ± 0.7 | 6.9 ± 1.0 | 47.8 ± 1.4 |
| 14.0 ± 0.4 | 8.1 ± 0.4 | 46.7 ± 1.3 |
| 18.9 ± 0.7 | 11.0 ± 1.2 | 43.8 ± 1.6 |
| 22.6 ± 0.6 | 13.2 ± 0.8 | 42.2 ± 1.8 |

To validate the force fields against experimental data, as well as to assess whether the implemented simulation algorithms are reliable, effect of H₂S on the IFT of water, γ is quantified. γ is estimated using Equation 3.1[87]

$$\gamma = \frac{1}{2}L_z[\langle P_{zz} \rangle - \frac{1}{2}(\langle P_{xx} \rangle + \langle P_{yy} \rangle)] \quad (3.1)$$

In Equation 3.1, L_z is the length of the simulation box along the Z-direction perpendicular to the interface, while P_{xx} , P_{yy} , and P_{zz} are the pressure tensors along X, Y, and Z directions respectively. The IFT results are presented in Table 3.5 and Figure 3.4b. The IFT results are in reasonable agreement with experiments, [86] as shown in Figure 3.4b. The slight difference between simulated and experimental IFT data could be due to the truncation of the dispersive interactions, which were not corrected for in the calculations. [88] For completeness, the IFT of pure SPC/E water at 313K has been reported to be 60.7 mN/m, [89] whereas in this study, 55.1 ± 1.8 mN/m was obtained. Both simulated and experimental results show that H₂S decreases water surface tension and that the effect is stronger as the H₂S pressure increases. Because the density profiles of Figure 3.3 show an accumulation of H₂S at the interface, it suggest that H₂S acts as a surfactant, consistent with what has been reported by Riahi and Rowley. [70] According to

Riahi and Rowley, [70] contacting a slab of water simulated with the polarizable model SWM4-NDP at the density of 764 kg/m^3 , with liquid H_2S of density 764 kg/m^3 at 313 K reduced the IFT from 63 to 20 mN/m, which is in good agreement with experimental data. [86]

To quantify the solvation of H_2S molecules in bulk liquid water, an equilibrium MD simulation was conducted for a bulk system, in the absence of interfaces, as described in section 3.3.1. The system comprises 2123 H_2O molecules and 3 H_2S molecules, and gives solubility under ambient conditions. The simulation was conducted at atmospheric pressure and 313 K. To quantify the hydration structure, radial distribution function (RDF) between the sulfur (S) of H_2S and the oxygen of water (OW) was calculated, as well as the RDF between S and the hydrogen atoms of water (HW). The results are in good agreement with the ab initio study of Riahi and Rowley, [70] conducted using the CP2K package. [90] The three-dimensional (3D) distribution of oxygen atoms of water (OW) around the bulk H_2S was also calculated. The results are shown in Figure 3.6. This system was also used to compute the self-diffusion coefficient of both water and H_2S in the bulk. The values obtained were 3.2 ± 0.8 and $3.5 \pm 0.5 \times 10^{-9} \text{ m}^2/\text{s}$ for H_2S and water, respectively and are consistent with previous simulation results.[70, 91] The estimated diffusion coefficient of H_2S in water is in reasonable agreement with the value of $2.6 \pm 0.1 \times 10^{-9} \text{ m}^2/\text{s}$ reported by Riahi and Rowley,[70] who conducted simulations using polarizable force fields. Tamimi et al.[92] reported experimental diffusion coefficients of $2.55 \times 10^{-9} \text{ m}^2/\text{s}$ for H_2S in bulk water at 308 K.

3.4.2 Confined systems

3.4.2.1 Density profiles

The distribution of molecules within the 1.0 nm-wide pore is quantified in terms of molecular density profiles in the direction normal to the pore surfaces. The density profiles for water oxygen atoms (OW) and sulfur atoms of H₂S (S) are shown in Figure 3.7 at different H₂S pressures. Because the density profile of OW does not change significantly with H₂S pressure, only one OW profile is shown for clarity. For all density profiles shown, $Z = 0$ corresponds to the center of the pore. For the 1 nm wide pore, +5 and 5 Å represent the location of oxygen atoms of the –OH groups on the two silica slabs. The OW density profiles reveal layering of water molecules with two distinct hydration peaks formed at a distance of ~ 1.25 Å from the pore walls. This suggests that water molecules interact strongly with the pore surfaces, possibly through hydrogen bonds, as discussed in detail elsewhere. [93]

The results reveal that H₂S molecules distribute primarily in the region close to the pore center while they seem excluded from the interfacial region. The exclusion of H₂S from the regions near pore walls could be due to the limited ability of H₂S to form hydrogen bonds with the OH groups on the surface, as well as to the large water density near the interfaces, which could yield steric hindrance. The limited ability of H₂S to form hydrogen bonds was attributed by Riahi and Rowley to its large size and weak polarity. [70] The small shoulder in the RDF between bulk S and HW supports the limited ability of H₂S to form hydrogen bonds with water (see Figure 3.5b).

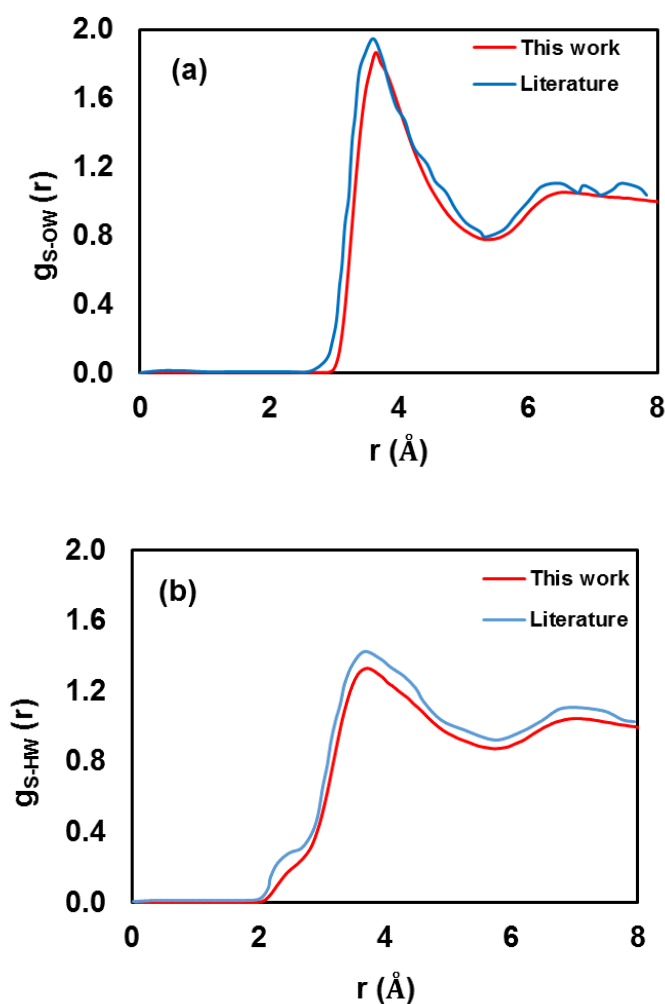


FIGURE 3.5: Hydration structure of H_2S in bulk water under atmospheric conditions. (a) RDF between sulfur (S) of H_2S and oxygen of water (OW), (b) RDF between sulfur of H_2S and hydrogen atoms of water (HW). In panels (a,b), the literature datasets are from Riahi and Rowley. [70]

3.4.2.2 Solubility

The solubility of H_2S in water confined within the 1.0 nm-wide pore is estimated as the ratio of the number of adsorbed H_2S to the number of water molecules within the pore at equilibrium. ~ 1 nm from the pore entrances were excluded to eliminate pore entrance effects. The results, reported in Table 3.6 and Figure 3.8, show that the solubility of H_2S in confined water increases as the bulk pressure increases, but in all cases, it is much lower compared to the solubility of H_2S in bulk water. The

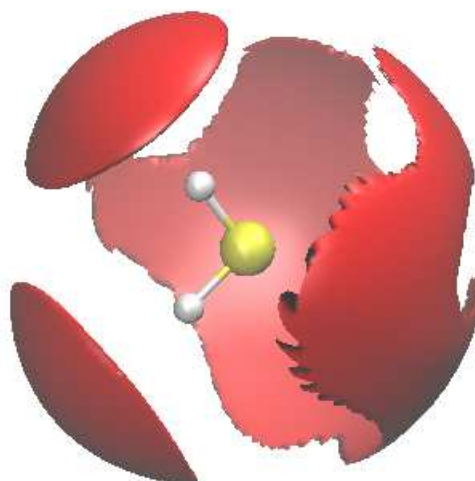


FIGURE 3.6: 3D distribution of OW around H₂S. The iso-density surface is drawn at 0.363 \AA^{-3}

observation that confinement reduces H₂S solubility in water is contrary to most studies on gas solubility in confinement as the results from those studies show that solubility of a gas increases in confinement. [13, 15–17] However, lower solubility of a gas in confinement compared to the bulk value has been reported in some cases. [20, 94] For example, Hu et al. [66] reported lower solubility for methane in benzene confined within graphite pores for pore width in the range $\sim 16 - 32 \text{ \AA}$. The results discussed so far suggest that, for water–H₂S in the 1.0 nm–wide silica pore, there is no preferential adsorption of H₂S close to the pore walls and there is no fluid–fluid interface inside the pore as the pore is fully hydrated. H₂S adsorption does not occur where local water density is low, suggesting that there is no enhancement of H₂S density via filling molecular cavities. Thus, it appears that none of the mechanisms leading to oversolubility described by Ho et al. [14] is observed for the system considered here. For completeness, it should be noted that Ho et al. [14] found enhanced solubility of H₂ gas in OMCTS confined in MCM-41, and observed accumulation of H₂ in low OMCTS density regions close to the pore

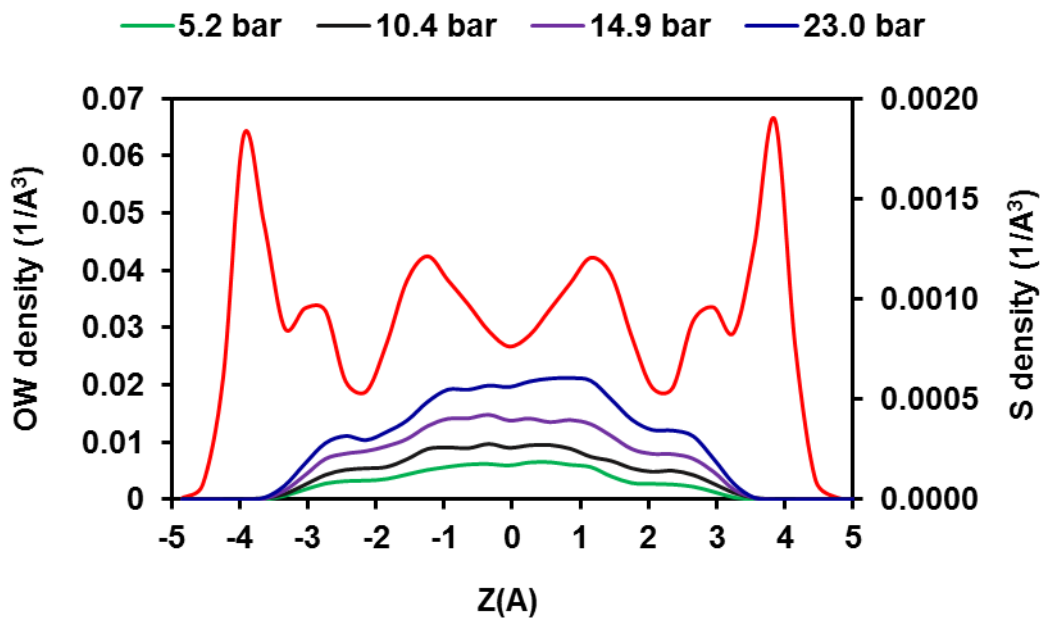


FIGURE 3.7: Density profile of oxygen atoms of H_2O (OW, red line) at 23 bar and sulfur atom of H_2S (S) along the direction perpendicular to the pore surface at different bulk pressures for a 1 nm slit pore

TABLE 3.6: Solubility of H_2S in Confined Water for 1nm pore^a

| Bulk Pressure (bar) | Solubility $\times 10^3$ |
|---------------------|--------------------------|
| 5.2 ± 0.2 | 3.0 ± 0.5 |
| 10.4 ± 0.2 | 3.7 ± 0.7 |
| 14.9 ± 0.4 | 5.1 ± 0.6 |
| 23.0 ± 0.4 | 8.1 ± 1.0 |

TABLE 3.7: Solubility of H_2S in Confined Water for 1.49nm pore^a

| Bulk Pressure (bar) | Solubility $\times 10^3$ |
|---------------------|--------------------------|
| 7.4 ± 0.2 | 3.7 ± 0.2 |
| 14.4 ± 0.3 | 6.9 ± 0.4 |
| 20.5 ± 0.3 | 9.9 ± 0.5 |
| 26.0 ± 0.6 | 10.5 ± 1.5 |

center.

3.4.2.3 Hydration structure

To investigate if there exist a relationship between lower solubility of H_2S in confined water and its hydration structure, the atomic RDF was calculated between

TABLE 3.8: Solubility of H₂S in Confined Water for 2.2nm pore^a

| Bulk Pressure (bar) | Solubility $\times 10^3$ |
|---------------------|--------------------------|
| 9.1 ± 0.4 | 5.1 ± 0.8 |
| 14.6 ± 0.3 | 7.5 ± 0.6 |
| 20.1 ± 0.5 | 10.4 ± 0.5 |
| 24.2 ± 0.5 | 13.8 ± 0.5 |

^aThe errors are standard deviations from the mean obtained from five blocks of production simulations, each of which lasts 2 ns

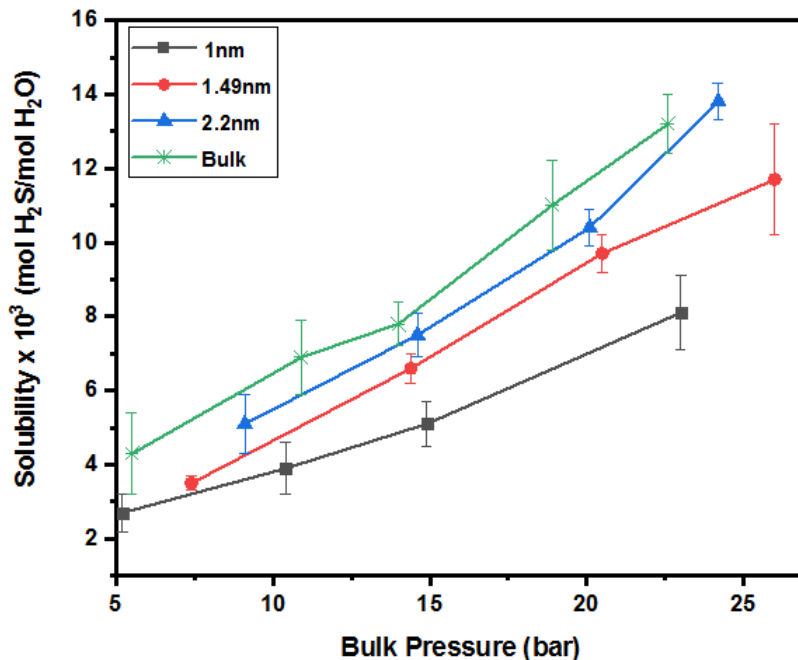


FIGURE 3.8: H₂S solubility in water as a function of bulk pressure. The results are shown for bulk water and confined water in all pore sizes simulated. Lines are only guides to the eye.

sulfur of H₂S and oxygen of water (g_{SOW}) as well as the 3D spatial distribution function (SDF) of the oxygen atoms of H₂O molecules within the first hydration shell of H₂S. Note that in all the simulations for the 3D SDF analysis, the H₂S molecules are free to move. For these calculations, MD-analysis code [95, 96] was implemented in an in-house Python algorithm. The radius of the first hydration shell corresponds to the position of the first minimum in the S-OW radial distribution function (g_{SOW}). For the SDF calculation, an independent simulation was

conducted within a 1 nm-wide pore with no bulk regions. The X and Y dimensions of the simulation box for this simulation are 104.78 and 100.82 Å respectively. Because of periodic boundary conditions, the pore is effectively infinite along X and Y directions. This simulation was conducted for 30 ns and the last 4 ns were used for analysis. The composition of the confined system represents the equilibrated hydrated pore exposed to H₂S at a pressure of 23 bar (see Table 3.9 for the composition of the simulated system). 23 bar is chosen because it is the highest pressure simulated in the 1nm pore. The RDF and SDF for the confined system are compared to a bulk system simulated at the same condition (23 bar and 313 K). A two-dimensional (2D) in-plane RDF was calculated for the confined system because the silica slabs confine the system along the Z-direction, whereas 3D RDF was calculated for the bulk system. The results are presented in Figure 3.9. The RDFs in Figure 3.9a show a higher first peak for the bulk than for the confined system, while the peak position is similar. This suggests a stronger interaction between coordinating water molecules and H₂S in the first hydration shell of bulk H₂S. These results are consistent with the SDF of water oxygen atoms within the first hydration shell of H₂S shown in Figure 3.9(b and c). These data suggest that bulk water is able to provide a more complete hydration structure to H₂S than water confined in the 1.0 nm wide silica pores considered in this study.

Although confinement reduces H₂S solubility in water, while it enhances CH₄ solubility as reported elsewhere,[13] results from this study reveal that H₂S solubility in confined water is higher than that of CH₄. This comparison holds even though the study on CH₄ solubility was conducted at 300 K, a lower temperature than

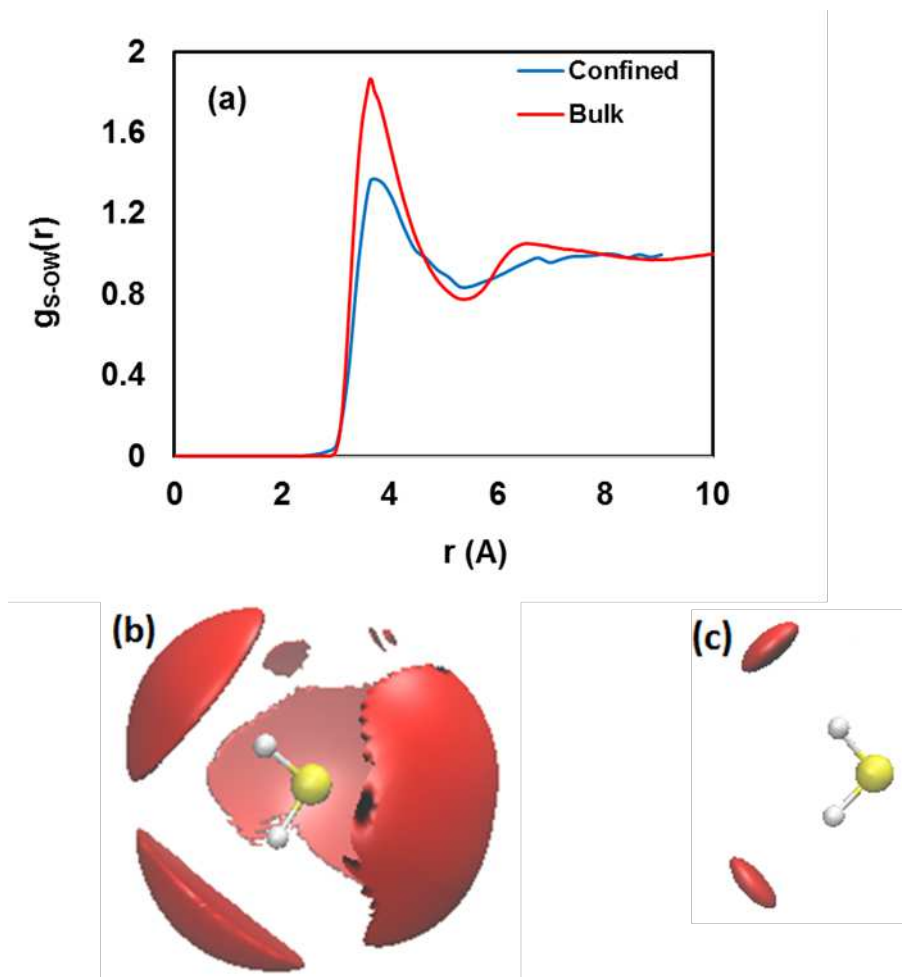


FIGURE 3.9: Comparison of RDF between S of H_2S and OW of H_2O in the 1.0 nm-wide pore and in the bulk(a); 3D SDF of OW in the first hydration shell of H_2S (b) in bulk water and (c) confined in a 1 nm-wide pore. The iso-density surfaces are drawn at 0.364 and 0.303 \AA^{-3} for bulk and confined water respectively. It was necessary to consider slightly different iso-density surfaces for computational reasons. The results show that the distribution of OW is denser in the hydration structure of bulk H_2S .

that chosen in this study, and at pressures higher than those considered here.

3.4.3 Effect of pore size

To investigate the effect of pore size on the solubility of H_2S in confined water, additional simulations were conducted in silica nanopores of width 1.49 and 2.2 nm. The atomic density profiles for OW and S for these systems are shown in Figure

TABLE 3.9: Composition of the Fluid Systems Simulated at 23 bar in Pores with Period Boundary Conditions Implemented along Both the X and Y Directions as Well as in the Bulk

| Pore size (nm) | Number of H ₂ O molecules | Number of H ₂ S molecules |
|----------------|--------------------------------------|--------------------------------------|
| 1 | 2875 | 28 |
| 1.49 | 4680 | 49 |
| 2.2 | 7140 | 91 |
| Bulk | 2064 | 58 |

3.10. The density profiles for OW do not change significantly as the pressure increases and only one profile is shown. The results reveal that the heights of first and second hydration layers, LO1 and LO2 in Figure 3.10, are similar for both pore sizes. This suggests that the pore hydration structure does not change significantly with pore width for the pores considered in this study. For the two pores presented in Figure 3.10, the results show that water density near the pore center approaches the value expected for bulk liquid water ($0.033 \text{ molecules } \text{\AA}^{-3}$). Layering of H₂S molecules is observed, with the formation of a pronounced H₂S layer (LS1) near the position of the second hydration layer (LO2). The H₂S density increases with pore size and bulk pressure, suggesting that solubility also increases with pore size and pressure. The solubility of H₂S in confined water for all simulated pores is shown in Figure 3.8. The results show that the solubility in confined water at the conditions considered is always lower than the corresponding bulk value and that the solubility increases as pore width increases.

To investigate the increase in H₂S solubility in confined water with pore width, simulations were conducted for water and H₂S confined in infinite pores of width 1.49nm and 2.2nm. The simulations were conducted for 30 ns and the last 4 ns were used for data analysis. The composition of the systems was chosen to mimic

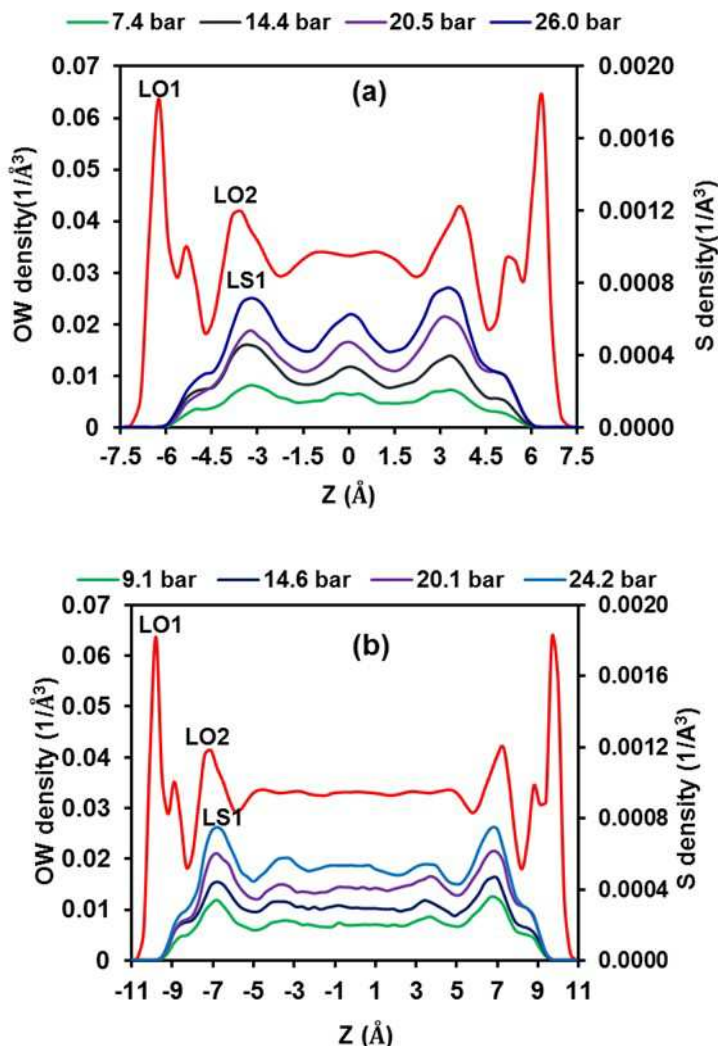


FIGURE 3.10: Density profile of oxygen atoms of H_2O (OW, red line) and sulfur atom of H_2S (S) along the direction perpendicular to the pore surface at different bulk pressures for (a) 1.49nm (b) 2.2nm pores. LS1 denotes the H_2S layer near the second hydration layer. Note that density profiles OW of H_2O (red line) for panels (a and b) are at 26.0 and 24.2 bar respectively

the equilibrated systems at 23 bar (see Table 3.9). Note that more water molecules are required to fill the pores as the pore size increases. The amount of H_2S present within the pores is determined based on the solubility data at 23 bar. While the solubility data point at 23 bar is available for the 1 nm pore, it was obtained by interpolation for the two larger pores based on the simulation results at other pressures. RDF and SDF results are presented in Figure 3.11 and 3.12 respectively.

Note that the RDFs were calculated in 3D for bulk systems and in 2D for confined systems. The first peak in the RDFs is located at the same distance for all systems, but the peak intensity is the lowest for the 1 nm pore and the highest for the bulk system. The heights of the first peak in the RDF for the 1.49 nm and the 2.2 nm pore are similar to that of the bulk, but there is a tendency for the peak intensity to increase with pore width. These results suggest a significant difference in the hydration structure of confined H₂S molecules in 1.0 nm width pore compared to the bulk, but as the pore width reaches ~ 1.5 nm in width the hydration structure approaches that of the bulk. This observation is consistent with the density distributions along the direction perpendicular to the pore surface (see Figures 3.7 and 3.10). The results are also consistent with the fact that the water density near the center of the 2.2 nm wide pore is similar to that of bulk liquid water. The 3D SDF results (Figure 3.12b) confirm that the molecular structure within the first hydration shell of H₂S becomes very similar to that observed in the bulk when the pore width is of 2.2 nm, whereas it is significantly different in 1.0 nm pore. The hydration structure results just discussed are consistent with results for the interaction energies between H₂S and water estimated in bulk water and in water confined in the various pores. The results (shown in Table 3.10) reveal that H₂S has the most attractive interaction with water in the bulk and the least in the 1 nm pore, consistent with the trend of solubility decrease with decreasing pore width.

The results of solubility in confinement presented here are qualitatively consistent with those reported for aqueous NaCl reported by Malani et al.[94] This group

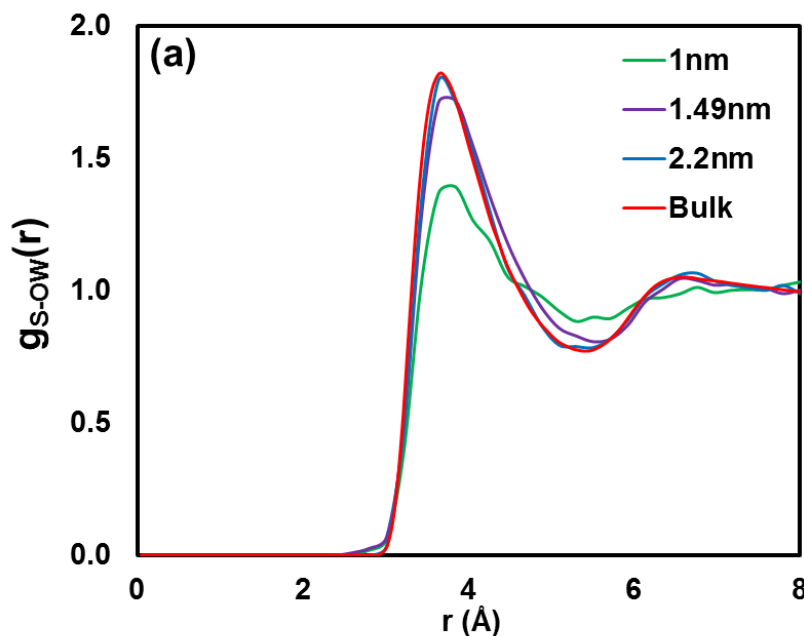


FIGURE 3.11: RDF between sulfur atom of H_2S and water oxygen in all simulated pores and in the bulk

TABLE 3.10: Water- H_2S interaction energies in the bulk and the simulated pores. The errors in the Coulombic and LJ interaction energies are standard deviation from the mean while errors in the total interaction energies were obtained from the errors in Coulombic and LJ interaction energies using error propagation method

| System | Coulombic (kJ/mol) | LJ (kJ/mol) | Total (kJ/mol) |
|--------|--------------------|-----------------|-----------------|
| Bulk | -11.8 ± 0.2 | -13.2 ± 0.1 | -25.0 ± 0.2 |
| 2.2nm | -11.5 ± 0.1 | -12.2 ± 0.2 | -23.7 ± 0.2 |
| 1.49nm | -11.1 ± 0.1 | -11.7 ± 0.3 | -22.8 ± 0.3 |
| 1nm | -10.3 ± 0.1 | -9.8 ± 0.2 | -20.1 ± 0.2 |

reported a lower solubility of NaCl in water confined within graphene pores of width 0.8 nm compared to bulk water and that the solubility increased with pore width. The increase in solubility was attributed to increase in the coordination number of water molecules around the ions as the pore size changed from 0.8 to 2.0 nm. However, NaCl is a salt and therefore rather different from H_2S . It is possible that the mechanisms responsible for the undersolubility in confined water are different in these two cases.

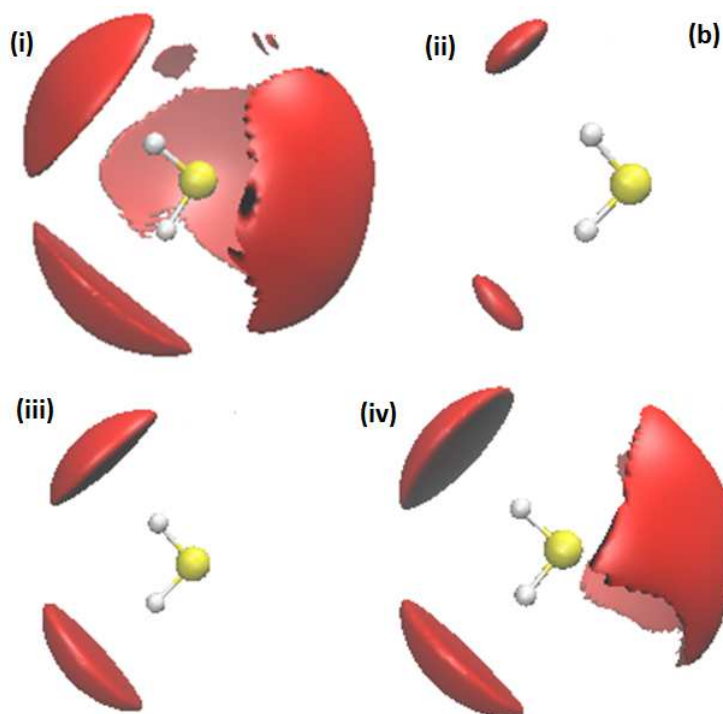


FIGURE 3.12: 3D SDF of water oxygen atoms in the first hydration shell of H_2S in all pores and in bulk water. The iso-density surfaces are drawn at 0.364, 0.303, 0.318 and 0.345 \AA^{-3} for a,b,c and d respectively. For computational reasons, the iso-density surfaces are drawn at slightly different densities

3.4.4 Structural properties

3.4.4.1 Orientation of confined fluid molecules

The density profiles shown in Figure 3.10 reveal layering of H_2O molecules and H_2S molecules. The orientation of H_2O molecules in these layers is quantified by plotting the distribution of the angle theta, formed between the dipole moment vector of H_2O and the normal vector to the surface, and that of the angle between the H–H vector of H_2O and the vector normal to the surface. The result shows that water molecules in LO1 show preferential orientation and lay at $\sim 67^\circ$ to the Z-axis. In this configuration, water molecule preferentially point one of its hydrogen atoms towards the surface, probably in an attempt to form hydrogen

bond with the $-OH$ groups on the silica surface. The density profiles of water oxygen (OW) and water hydrogens (HW) presented in **Figure 3.14** complement the angle distribution results. In **Figure 3.14**, $Z=+5$ and $Z=-5$ denote the pore walls while $Z=0$ is the location of the pore centre. Note that the density profiles are symmetrical about the pore centre reflecting the symmetry of the pore and as a result, only the peaks in the region to left of the line of symmetry are discussed (between $z=-5$ and $z=0$). As shown in **Figure 3.10**, the closest peak to the pore surface in OW density profile (LO1) is located at $\sim 1.25\text{\AA}$ from the surface and the closest peak to the surface in the HW density profile is located at $\sim 0.8\text{\AA}$ from the surface with nearly equal density. This shows that water molecules preferentially orient with one hydrogen pointing towards the surface; this configuration perhaps maximizes the hydrogen bonding formation between water molecules in the first hydration layer and the $-OH$ groups on the silica surface. These results are consistent with prior investigations that interfacial properties of water changes when it interacts with silica surface.[11, 93]

The orientation of confined aqueous H_2S molecules is quantified in terms of the angle formed by the S-M vector, pointing from the sulfur atom to the mid-point (M) of the H-H vector in H_2S , and the surface normal vector, as well as the angle formed by the H-H vector of H_2S and the surface normal vector. The results, shown in **Figure 3.15**, show that there is no preferential orientation for aqueous H_2S in LS1 and at the middle of the pores.

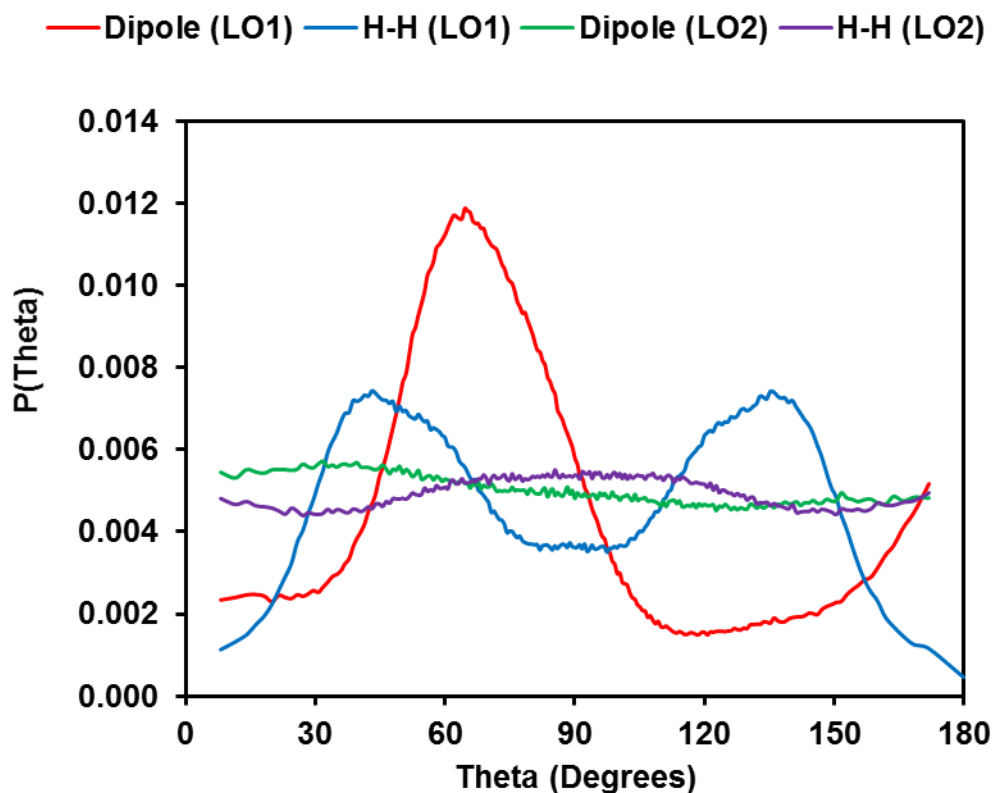


FIGURE 3.13: Distribution of angle theta, formed between the dipole moment vector and H-H vector of water and the vector normal to the surface

3.4.4.2 In-plane density distributions

The in-plane density distributions of oxygen atoms of water OW in layers LO1 and LO2 and that of S atoms of H₂S in layer LS1 were calculated to obtain more information about the structure of the confined fluids. For these calculations, only the pores of width 1.49 and 2.2 nm were considered as layer LS1 is not visible in the 1nm pore (see density profiles in Figure 3.7). Please refer to Figure 3.10 for the positions of layers LO1, LO2, and LS1. The in-plane density distributions of OW and S for 1.49 nm pore are shown in Figure 3.16. Only the results for 1.49nm are shown as they are not significantly different from those obtained for the 2.2nm pore. The simulations were conducted at 26 bar, the highest pressure considered in

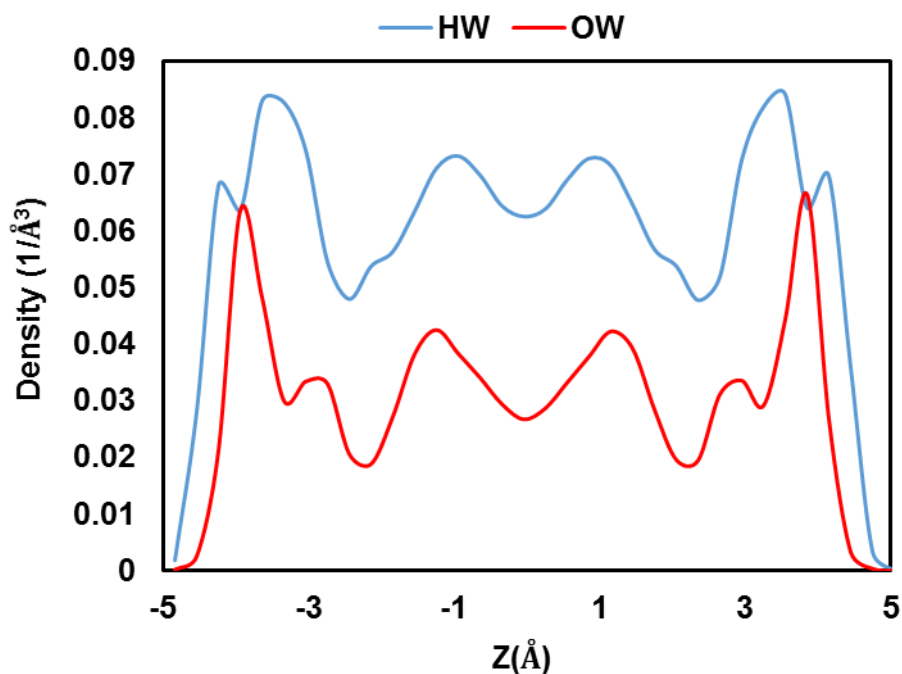


FIGURE 3.14: Density profiles of OW and HW in the direction perpendicular to the pore surface for 1nm pore

the 1.49nm pore. The results present an X–Y section of thickness 1.5 Å centered on the atomic density peak. The contour plots show a well-structured LO1 hydration layer, in which OW atoms distribute near the vertices of the hexagonal rings formed by the silicon atoms in the solid substrate. This observation is consistent with what has been reported previously.[11, 93] Water molecules in layer LO2 show a uniform distribution suggesting that water molecules in this layer are less influenced by the silica substrate. This result is consistent with what has been reported previously in the literature.[11] The in-plane distribution of H₂S molecules in layer LS1 suggests no preferential distribution and tendency of aqueous H₂S aggregation.

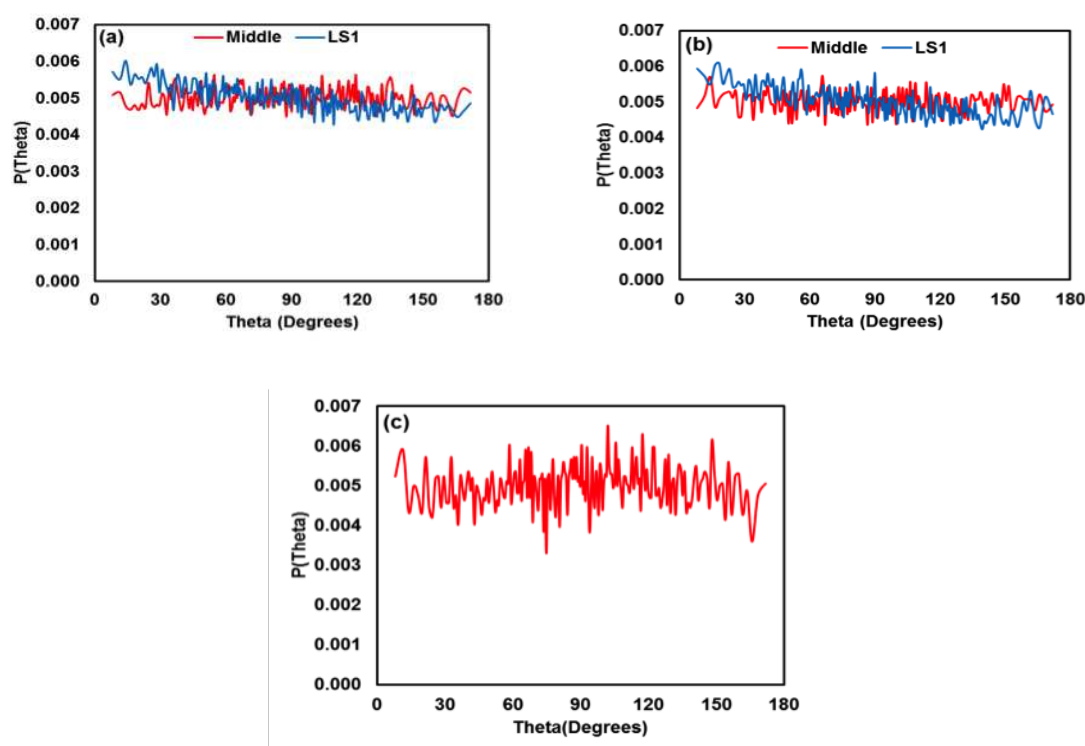


FIGURE 3.15: Distribution of angle theta, formed between the S-M vector and the H-H vector of H_2S and the vector normal to the surface for H_2S molecules in LS1 and middle of the pore for (a) 2.2nm (b) 1.49nm (c) 1nm at 23 bar. For 1nm-size pore, only angle distribution for H_2S molecules at the middle of the pore is shown in panel (c)

3.4.5 Dynamical properties

3.4.5.1 Diffusion coefficients

To study the mobility of H_2S and water through the pores, the mean square displacement (MSD) of the fluid molecules as a function of time was calculated. The MSD plots are shown in Figure 3.17. The systems whose composition is reported in Table 3.9 were used for this calculation. From the MSD data, the diffusion coefficients were calculated for H_2S and water using the Einstein equation

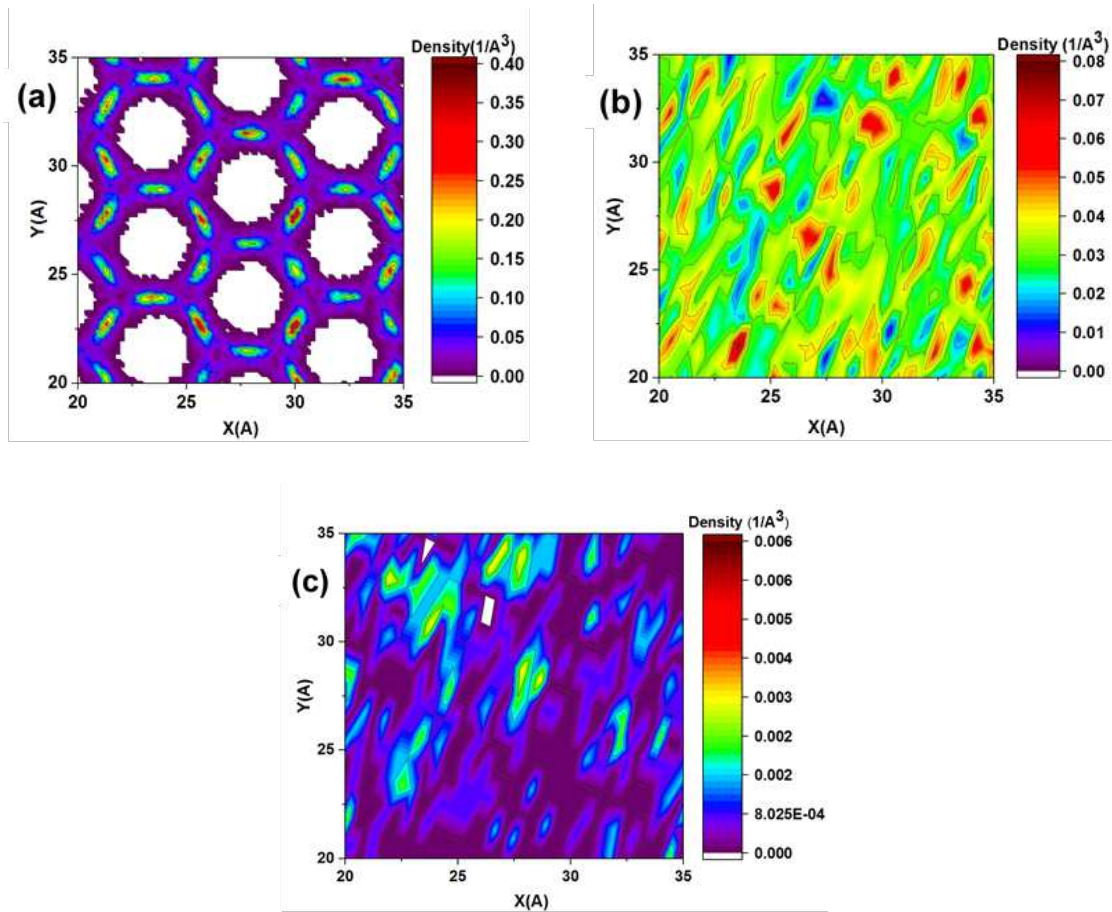


FIGURE 3.16: In-plane density distribution of oxygen atoms of water (OW) in layer LO1 (a) and LO2 (b). In plane density distribution of sulfur atoms of H₂S in layer LS1 (c). The results are obtained for the 1.49 nm-wide silica pore. The pore contains 800 H₂S and 7600 H₂O molecules

shown in Equation 3.2[59]

$$D = \lim_{t \rightarrow \infty} \frac{1}{2dimt} \langle |r_i(t' + t) - r_i(t')|^2 \rangle \quad (3.2)$$

In Equation 3.2, $r_i(t)$ and $r_i(t')$ are the positions of molecule i at time t and time origin t' , respectively, and dim is the dimensionality of the system. The parameter dim equals 2 for H₂S in confined water and 3 in bulk water. The calculated diffusion coefficients are shown in Table 3.11.

The results suggest that confinement slows down the diffusion of aqueous H₂S.

TABLE 3.11: Diffusion coefficients for H₂S in water^a

| System | D (H ₂ S) 10 ⁻⁹ m ² /s | D (H ₂ O) 10 ⁻⁹ m ² /s |
|-------------|---|---|
| 1nm pore | 2.2 ± 0.3 | 1.3 ± 0.2 |
| 1.49nm pore | 2.4 ± 0.2 | 1.9 ± 0.3 |
| 2.2nm pore | 2.7 ± 0.1 | 2.3 ± 0.2 |
| Bulk | 3.0 ± 0.2 | 3.7 ± 0.2 |

^aThe results are shown for the bulk system, as well as for the three confined systems. The bulk pressure is 23 bar

The diffusion coefficient of H₂S has the lowest value in the 1 nm pore. It is worth noting that even though this diffusion coefficient is lower than what was observed in bulk water, it is ~ 3 times faster than that calculated for hydrated CH₄ in the same pore (7.83×10^{-10} m²/s). [26] In the case of H₂S in water, confinement only reduces the diffusion coefficient by $\sim 20 - 30\%$, while for aqueous CH₄ in 1nm silica pore, confinement reduces the diffusion coefficient by $\sim 50 - 60\%$. From the results in Table 3.11, it is also evident that confinement dampens the diffusion of confined water, the observation that has been reported in previous studies.[97] It is noteworthy that in the bulk, the diffusion coefficient of water is higher than that of aqueous H₂S, in confinement however, the opposite is observed. This is likely a consequence of the fact that water molecules adsorbed close to the pore walls have very slow mobility.

To quantify whether the diffusion of H₂S through the hydrated pores is isotropic or anisotropic, positions of H₂S molecules at time t and $t + \Delta t$ ($\Delta t = 250$ ps) were extracted from the simulation trajectory, from which 2D X–Y vectors were calculated. The last 20 ns of the simulations were used for this analysis. The endpoints of the vectors are shown in Figure 3.18. The principal component analysis (PCA) [98] described elsewhere [99] was then applied to calculate the eigenvalues

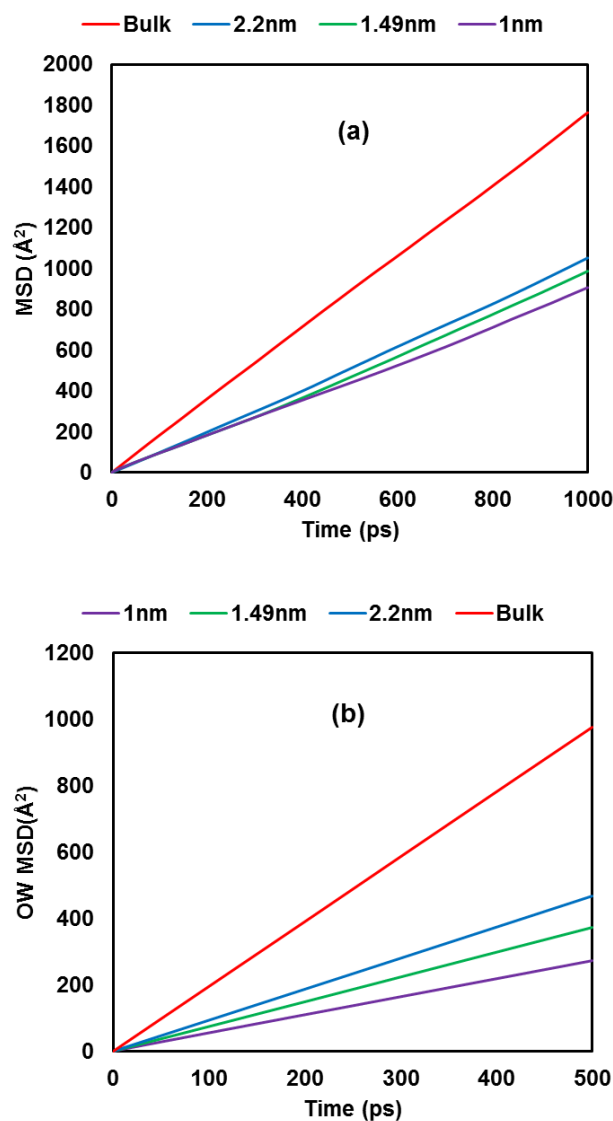


FIGURE 3.17: Mean square displacements of sulphur of H₂S (a) and oxygen of water (b) in the simulated hydrated pores compared with that of bulk water at 23 bar.

and eigenvectors. PCA reduces the datasets to lower dimension that maximizes the variance of the data. When the eigenvalues are similar, the diffusion in X–Y plane is isotropic; when the eigenvalues are different, the diffusion is anisotropic. The eigenvalues for all the simulated pores are reported in 3.12. The results suggest that diffusion of H₂S in all simulated pores is isotropic along X and Y directions, similar to CH₄ diffusion in the hydrated silica pore of width 1 nm.[99]

TABLE 3.12: Eigenvalues from PCA of H₂S diffusion in all hydrated pores

| System | eigenvalue 1 | eigenvalue 2 |
|-------------|--------------|--------------|
| 1nm pore | 1.06 | 0.94 |
| 1.49nm pore | 1.00 | 1.00 |
| 2.2nm pore | 1.01 | 0.99 |

The permeability, P of H₂S in confined water can be obtained from its solubility, S and its diffusion coefficient, D , through the hydrated pore using the relation:[100]

$$P = S \times D \quad (3.3)$$

In Equation 3.3, P is measured in mol/ms, S in mol/m³, and D in m²/s. The estimated permeability of H₂S through the hydrated 1 nm pore is estimated as 8.01×10^7 mol/ms. This value is higher than the permeability of CH₄ through the same hydrated pore estimated as 5.63×10^7 mol/ms. [26] The difference in permeability is due to higher solubility and diffusion coefficient values for H₂S in confined water compared to CH₄. The larger permeability for H₂S compared to methane supports hypothesis by Phan et al.[26] that hydrated nano-pores could be used as perm-selective materials for natural gas sweetening.

3.4.5.2 Residence times and Rotational dynamics

The residence times for individual molecules within layers of interest in the hydrated pores were calculated from the autocorrelation function $C_R(t)$ [101]

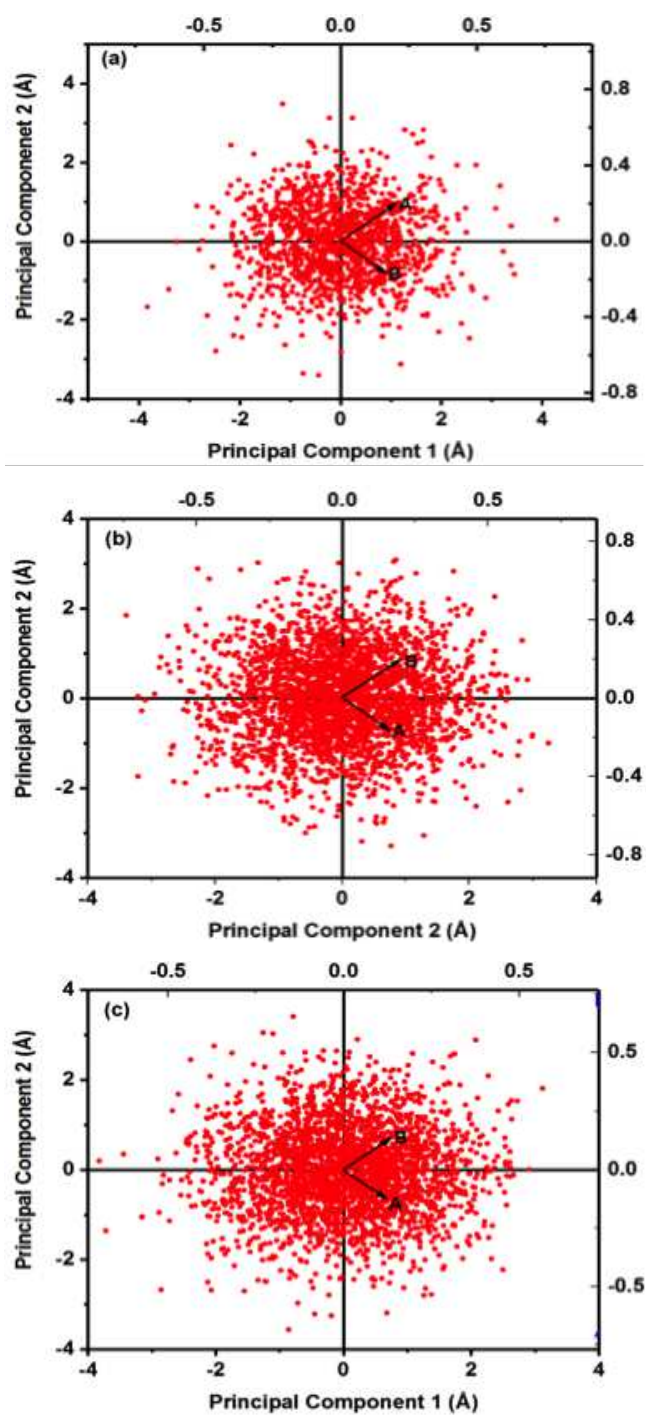


FIGURE 3.18: End point of vectors connecting positions of H₂S molecules at time t and $t + \Delta t$ ($\Delta t = 250$ ps) in (a) 1 nm pore (b) 1.49 nm pore and (c) 2.2 nm pore

$$C_R(t) = \frac{\langle N_i(t)N_i(0) \rangle}{\langle N_i(0)N_i(0) \rangle} \quad (3.4)$$

In Equation 3.4, $N_i(t) = 1$ if molecule i is found in the layer of interest at time t and 0 otherwise. If molecule i belongs to the layer at time $t = 0$, $N_i(0) = 1$ and remains equal to 1 as long as molecule i remains in the layer; but becomes 0 when molecule i leaves the layer of interest. $C_R(t)$ decays from 1 to 0. The faster $C_R(t)$ decays to zero, the faster the molecules leave the layer considered. In Figure 3.19a, $C_R(t)$ for H_2O found within LO1, LO2 and the middle of 1.49 nm pore are shown. The results are compared with $C_R(t)$ for bulk water. In bulk water, the residence time was calculated as the time, on average, spent by water molecules within a slab of the same dimensions as those considered in the pores. In the simulations considered in Figure 3.19, the confined system consists of 800 H_2S molecules and 7600 water molecules, while the bulk system contains 58 H_2S molecules and 2064 water molecules. The thickness of the layers centered on peak positions in LO1 and LO2, as well as those in the bulk used for the $C_R(t)$ calculation is 1.5 Å in all cases. From the $C_R(t)$ curves, the residence times were obtained as the time it takes $C_R(t)$ to decay from 1 to $1/e$ [101]. The residence times are reported in Table 3.13

The residence time results show that H_2O in the first hydration layer (LO1 in Figure 3.19) remain within the layer longer than H_2O in layer LO2 and the middle of the pore. When compared with bulk water, H_2O in all regions of the pore show

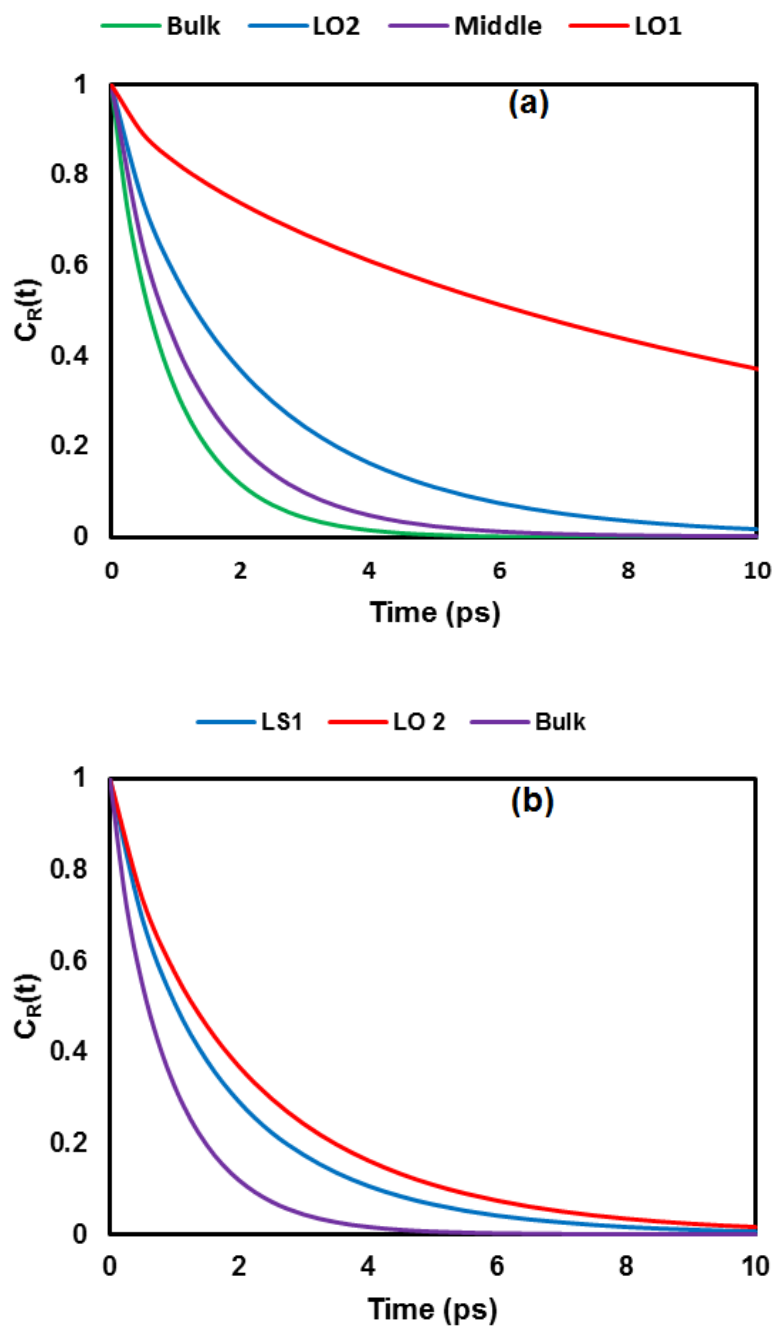


FIGURE 3.19: Residence autocorrelation function for water molecules found within layers LO1, LO2 and in the middle of the pore of width 1.49 nm compared to that of bulk liquid water (a). Residence autocorrelation function for water molecules in layer LO2, H₂S molecules in layer LS1, and bulk water molecules (b). The confined system consists of 800 H₂S and 7600 H₂O molecules. The bulk system consists of 58 H₂S and 2064 H₂O molecules.

TABLE 3.13: Residence times for water and H₂S molecules in different regions in 1.49nm pore and bulk water

| Region | Residence time (ps) |
|--------|---------------------|
| LO1 | 10.0 |
| LO2 | 2.0 |
| LS1 | 1.6 |
| Middle | 1.2 |
| Bulk | 0.9 |

longer residence times. $C_R(t)$ is also computed for H₂S molecules found within a layer of thickness 1.5 Å centered on LS1 located near LO2. The results, presented in Figure 3.19b and Table 3.13, show that H₂S has a shorter residence time than H₂O in the same region. The faster dynamics of H₂S in this region could be due to its limited ability to form hydrogen bonds with water molecules in this layer and its weaker interaction with the silica surface compared to water molecules. The rotational dynamics of the fluid molecules found within layers considered in $C_R(t)$ discussed above is quantified by calculating autocorrelation functions for the dipole moment of water molecules and the S–M vector of H₂S molecules. The S–M vector is the vector pointing from the sulfur atom to the midpoint (M) of the H–H vector of H₂S molecule. The vector–vector autocorrelation function is defined as:[101, 102]

$$C_v(t) = \frac{\langle v_i(t)v_i(0) \rangle}{\langle v_i(0)v_i(0) \rangle} \quad (3.5)$$

In Equation 3.5, $v_i(0)$ is either the dipole moment vector or the S–M vector of molecule i at time $t = 0$. The results are shown in Figure 3.20 and suggest that

water molecules in layer LO1 rotate more slowly than those in layer LO2. Water molecules in LO2 rotates more slowly compared to bulk water. The results are in agreement with prior simulation results [11] and confirms that the interactions of hydration water molecules with the silica surface slow down the rotation of interfacial water molecules. This effect becomes weaker as the distance between water molecules and the solid–liquid interface increases. Figure 3.20 also shows the result obtained for H₂S molecules. When the results for bulk H₂S are compared to those for H₂S molecules in layer LS1, it seems confinement slows down the rotational dynamics of H₂S molecules, but not very significantly. Comparison of the autocorrelation function result obtained for H₂S in layer LS1 with those obtained for H₂O in layer LO2 shows that H₂S molecules rotate much faster than water molecules at this distance from the silica surface. Note that LS1 is located close to LO2. This observation is likely due to H₂S molecules not able to form strong hydrogen bonds with water molecules and is consistent with the residence times results presented in Figure 3.19.

3.5 Conclusions

Atomistic equilibrium MD simulations were conducted for systems composed of different loadings and ratios of water and H₂S in slit-shaped silica pores of different widths at 313 K. The study was performed to investigate the effect of confinement on the solubility of H₂S in water, as well as on structural and dynamical properties of the confined fluids. In all cases, system pressure is manipulated by changing

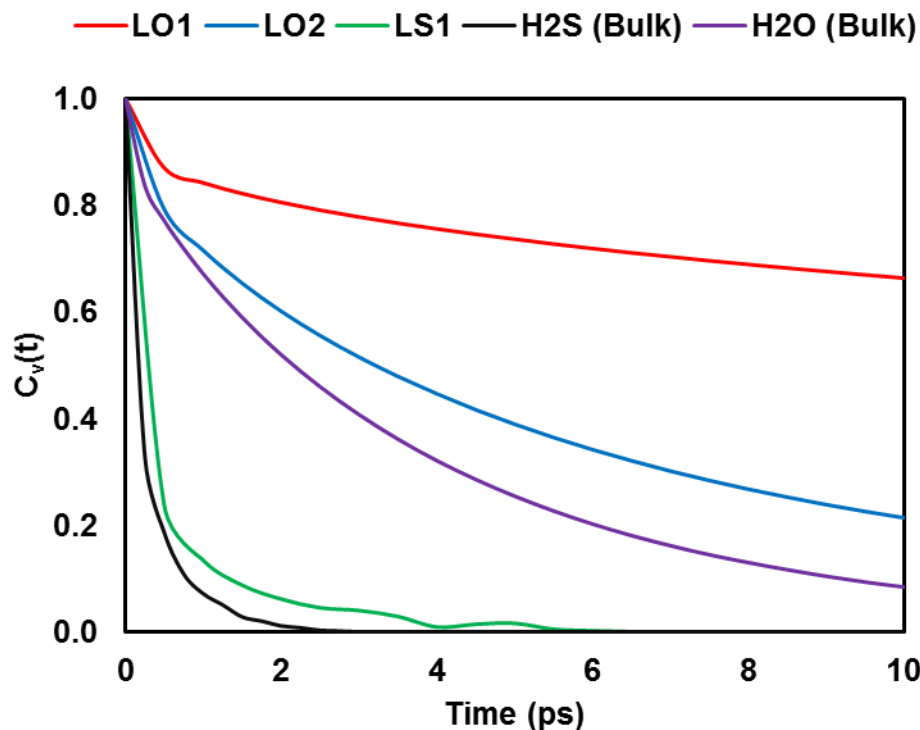


FIGURE 3.20: Vector–vector autocorrelation function for fluid molecules at different regions of the 1.49 nm pore compared with that of bulk water. The systems considered are the same as those in Figure 3.19

the number of H₂S molecules in bulk regions. The simulation results are quantified in terms of atomic density profiles, solvation structure, as well as dynamical properties including permeability of H₂S across the hydrated 1.0 nm–wide pore. The results reveal that confinement reduces H₂S solubility in water. Analysis of the hydration structure suggests that confinement strongly perturbs the hydration of H₂S molecules when the silica pores are narrower than ~ 1.5 nm. The diffusion coefficients computed for H₂S molecules in confined water show that confinement reduces the diffusion coefficient by $\sim 20 - 30\%$ in the narrowest pores considered here compared to bulk values. From the solubility and diffusion coefficient obtained for H₂S molecules in confined water, its permeability through hydrated silica pores was computed. The H₂S permeability in a 1 nm–wide silica

pore filled with water at 313 K was found to be higher than that of CH₄ under similar conditions, suggesting the possibility of using hydrated slit-shaped silica nanopores for natural gas sweetening. The results presented here could contribute to understanding of the behaviour of fluids in subsurface formations.

3.6 Acknowledgements

Generous allocations of computing time were provided by the National Energy Research Scientific Computing Center (NERSC) at Lawrence Berkeley National Laboratory and the University College London High Performance Facility (LEGION@UCL). NERSC is supported by the DOE Office of Science. S.B.B. acknowledges financial support from the Petroleum Technology Development Fund (PTDF). A.S. acknowledges financial support from the European Union via the Marie Curie Career Integration grant no. 2013-CIG- 631435. This research received funding from the European Unions Horizon 2020 research and innovation program under grant no. 640979. D.R.C. was supported by the U. S. Department of Energy, Office of Basic Energy Sciences, Division of Chemical Sciences, Geosciences and Biosciences under grant DE-SC0006878. We are grateful to the group of Dr. Chris Lorenz, in particular Mateusz Bieniek, for sharing Python code to complete the 3D spatial distribution analysis.

Chapter 4

Factors Governing the Enhancement of Hydrocarbon Recovery via Acid Gas Injection: Insights from A Molecular Dynamics Study in Dry Nano-Pores

The material presented in this Chapter was published in **2019** in volume 123, pages 23907-23918 of The Journal of Physical Chemistry C

4.1 Abstract

Although enhanced oil recovery (EOR) is often achieved by CO₂ injection, the use of acid gases has also been attempted, for example in oil fields in west Canada. To design EOR technologies effectively, it would be beneficial to quantify the molecular mechanisms responsible for enhanced recovery under various conditions. Here,

molecular dynamics simulation results that probe the potential of recovering *n*-butane confined from silica, muscovite and magnesium oxide nano-pores, all proxies for sub-surface materials are reported. The three model solid substrates makes it possible to identify different molecular mechanisms that control confined fluid behaviour, and to identify the conditions at which different acid gas formulations are promising. The acid gases considered are CO₂, H₂S, as well as their mixtures. For comparison, in some cases the presence of inert gases such as N₂ is considered. In all cases, the nano-pores are dry. The recovery is quantified in terms of the amount of *n*-butane displaced from the pore surface as a function of amount of gases present in the pores. The results show that the performance of the gas depends on the chemistry of the confining substrate. While CO₂ is more effective at displacing *n*-butane from silica pore surface, H₂S is more effective in muscovite, and both gases show similar performance in MgO. Analysis of the interaction energies between the confined fluid molecules and the surface demonstrates that the performance of the acid gas depends on its interaction with the surface, which suggests experimental approaches that could be used to formulate the gas mixtures for EOR applications. The structure of the acid gas films at contact with the solid substrates is also quantified, as well as the self-diffusion coefficients of the fluid species in confinement. The results reported could contribute to designing strategies for achieving both improved hydrocarbon production and acid gas sequestration.

4.2 Introduction

The growing concern about greenhouse gas emissions has stimulated research into developing new technologies for capturing and sequestering CO₂. CO₂ injection into geological formations has received much attention,[27, 28, 31, 103–106] sometimes as a long-term storage opportunity, while in some other cases, CO₂ has been injected in oil and gas fields to simultaneously achieve enhanced hydrocarbon recovery and CO₂ sequestration.[107] For these strategies to be fully optimized, it is important to understand, and ultimately control the molecular mechanisms that are responsible for rock-fluid interactions, inclusive of fluid sorption, migration, and fixation. Enhanced oil recovery (EOR) is investigated in this Chapter. The EOR methods commonly used in oil and gas production include water, gas, and surfactant injection.[108–111] The technology follows either the flooding or the huff-n-puff mode. The huff-n-puff mode is sometimes preferred for shale formations due to their ultra-low permeability, which delays gas and pressure propagation from the injector to the producer well.[112] It has been reported that waterflooding can yield much lower recovery compared to gas injection, which sometimes justifies the use of gas injection as the preferred option.[29] Several studies have been reported in the literature concerning efforts directed towards understanding the mechanisms responsible for CO₂-based EOR.[31, 36–39, 45, 106, 111, 113, 114] In general, the enhancement of hydrocarbon recovery is either attributed to preferential adsorption of CO₂ on pore surfaces,[30–32, 115] or the dissolution of CO₂ in oil, which swells the oil and reduces its viscosity.[33–35, 105] Previous research by Le et al.[32] reported that CO₂ preferentially adsorbs on silica surfaces, weakening

n-butane adsorption, and effectively acting as a molecular lubricant that lowers the activation energy for *n*-butane diffusion. Santos et al.[39] conducted molecular dynamics simulations in slit-shaped calcite pores to study the effect of CO₂ on *n*-alkanes displacement from the pore surface. They identified several factors that control the preferential adsorption of CO₂ on calcite surface, including the amount of CO₂ present, temperature, hydrocarbon length, and pore size. Wang et al.[113] observed an increase in *n*-decane diffusion as CO₂ loading increases, and reported a maximum diffusion coefficient obtained at high pore loadings due to pore crowding. Experimental studies on CO₂ based EOR have also been reported in literature.[40–43] Jin et al.[40] carried out experimental studies on core samples from the Bakken shale formation, and found that supercritical CO₂ injection facilitates the recovery of up to 65% of hydrocarbon in place; they also reported that CO₂ becomes trapped in the reservoir over a wide pressure range which demonstrates the possibility of CO₂ sequestration. Eide et al.[41] reported experimental results on oil recovery by CO₂ injection into fractured core sample using nuclear magnetic resonance (NMR) and X-ray computed tomography; they reported oil recovery in excess of 90% of the original oil in place. Current research on EOR focuses on CO₂ injection as EOR can then be coupled with CO₂ sequestration. However, sequestering H₂S generated from oil and gas processing into geological formations is also desirable, and could promote hydrocarbon recovery. In fact, acid gases (CO₂+H₂S) have been injected into geological formations to reduce atmospheric emissions and at the same time enhance hydrocarbon recovery.[116] Field tests have been reported where acid gases were injected into geological formations in the Alberta basin of western Canada.[117] However, Khan

et al.[116] performed reservoir simulation studies complemented by experimental data from Clean Gas Technology Australia (CGTA) as input; based on those reservoir simulations, injecting a mixture of CO₂ and H₂S yields a lower recovery factor compared to injecting pure CO₂. Because it is possible that the performance of an EOR strategy depends on the formation features (rocks, pressure, temperature, hydrocarbons in place, porosity, presence of other fluids such as water, etc.), a detailed molecular-level understanding of the mechanisms responsible for EOR is desirable. This could be achieved by extensive molecular simulations. While results have been reported for CO₂, CH₄ and other hydrocarbons in nanopores, few studies explicitly attempted to quantify the behaviour of H₂S and its mixtures with CO₂ within narrow pores. An exception is the study reported in Chapter 3 where it was observed that H₂S solubility in water confined in narrow pores is much lower compared to the H₂S solubility in bulk water because confinement in nano-pores can strongly affect the hydration shell of aqueous H₂S.

This chapter investigates *n*-butane displacement due to pure H₂S, pure CO₂ as well as their mixtures within slit-shaped nano-pores carved out of silica, muscovite, and magnesium oxide (MgO). The three pores are chosen because silica and muscovite are considered representative of many sub-surface formations, while MgO is a model substrate useful for quantifying the molecular phenomena responsible for the results obtained. It should be noted that the MgO surface considered here is not hydroxylated. As such, it provides a model surface useful for understanding the molecular driving forces at play for the systems considered, but it does not provide a good model for real substrates e.g brucite. Because the systems considered

are dry, pH effects on the pore surfaces are not described. An exception is the silica substrate, which is protonated. Since the presence of water would certainly affect the results presented in this Chapter, future studies conducted perhaps with reactive force fields should address such effects. This Chapter focusses on the molecular behaviour of the fluids at the solid-fluid interface, as well as the transport of the confined fluids. Atomistic molecular dynamics (MD) simulations is employed to probe the effect of molecular interactions on the results obtained. While EOR performance cannot be directly quantified by the MD approach implemented here, the results are analysed in terms of the preferential adsorption of *n*-butane versus acid gases on the solid surfaces. The implicit assumption is that the dislocation of *n*-butane from the proximity to the solid substrates promotes EOR.

4.3 SIMULATION MODELS AND METHODOLOGY

4.3.1 Simulation set up

Molecular dynamics (MD) simulations were conducted for binary and ternary fluid systems composed of systems of C_4H_{10} - H_2S , C_4H_{10} - CO_2 , C_4H_{10} - N_2 , C_4H_{10} - H_2S - CO_2 and C_4H_{10} - acid gas - N_2 at various compositions confined within slit-shaped pores of width 22\AA carved out of silica, muscovite, and MgO. These substrates are representatives of many minerals or mineral components found in sub-surface formations. The silica surface was obtained by cutting β -cristobalite crystal along

the (1,1,1) crystallographic plane. The non-bridging oxygen atoms were fully protonated yielding a reasonable proxy for hydrophilic surfaces.[118] The resulting -OH surface density is 4.54 per square nanometer. The model MgO slab was obtained from the space group Fm3m replicated along the (001) plane.[119, 120] The exposed MgO surface was not hydroxylated. While this model might not be realistic, it makes it possible to quantify the mechanisms responsible for preferential adsorption. Muscovite was considered a model for clays and it has been used in previous studies. Details regarding this substrate have been documented in literature.[121–123] Brief description of muscovite is given as thus: Muscovite is a phyllosilicate mineral with structure similar to illite.[124] In muscovite, an interlayer of potassium ions holds a Tetrahedral-Octahedral-Tetrahedral (T-O-T) structure of Al-centred octahedral sheet sandwiched between two Si-centred tetrahedral sheets in which one Al atom substitutes one out of every four Si atoms. The potassium ion-bearing interlayer balances the negative charge due to Al substitution and holds the T-O-T layers via electrostatic interactions.[121] Each octahedral sheet contains two oppositely pointing -OH groups. The surface of each muscovite slab is not protonated, but it contains potassium ions resulting from cleavage along its basal plane (001). Muscovite with this surface termination has been used in several studies.[121–123, 125–127]. No water is considered in this study, although it would certainly affect the result, for example through potassium ion solvation. All solid substrates bear no net charge and were kept rigid throughout the simulation. Exceptions were the surface hydrogen atoms on silica surface and potassium ions on muscovite, which were allowed to vibrate. Each solid slab was maintained parallel to the X-Y plane of the simulation box. The X and Y dimensions for

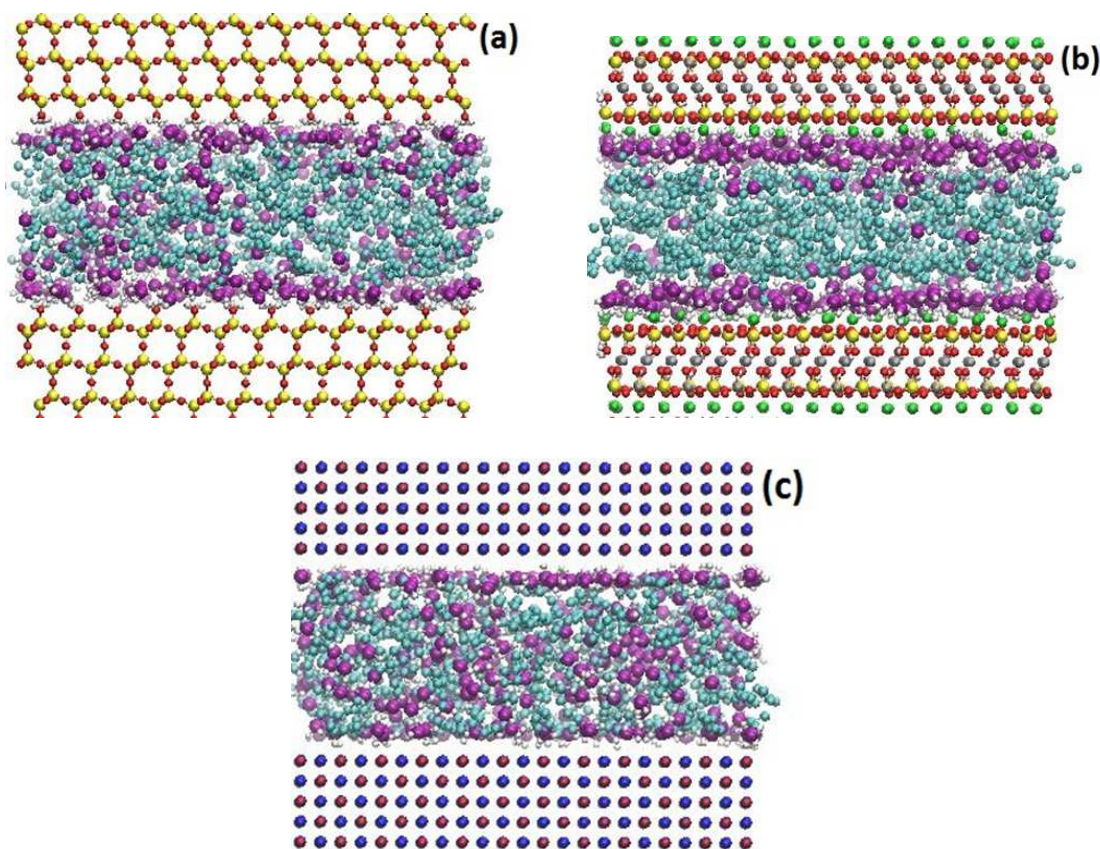


FIGURE 4.1: Simulation snapshots for binary systems containing *n*-butane and H₂S in silica (a) MgO (b) and muscovite (c). All systems shown contain 300 *n*-butane and 500 H₂S molecules. Cyan spheres are -CH₃ and -CH₂ in *n*-butane, purple are sulphur, white are hydrogen, red are oxygen, yellow are silicon, green are potassium, grey are aluminium, blue are magnesium

the three systems were 51.7×100.8 , 47.2×73.4 , and $47.2 \times 73.6 \text{ \AA}^2$ for silica, muscovite and MgO, respectively. The Z dimension of the simulation box was set to 54.92 , 58.3 and 53.52 \AA for silica, muscovite, and MgO, respectively. These dimensions yield slit-shaped pores of width 22\AA , measured as the shortest centre-to-centre distance between the oxygen atoms of the -OH groups on silica slabs, surface potassium ions in muscovite slabs and magnesium atoms in MgO across the pore volume. Because periodic boundary conditions (PBC) were applied in all directions, the simulated systems are infinitely long in X and Y directions. The initial configuration of the pure *n*-butane system was built by loading the pores

with 300 *n*-butane molecules. This number of *n*-butane molecules is estimated to correspond to approximately 60% of *n*-butane maximum loading in silica pore. Details regarding the simulations and the maximum amount of *n*-butane, CO₂ and H₂S that can fill the pores are reported in section B.1 of Appendix B. Binary systems containing *n*-butane and H₂S were simulated at different compositions: 300 molecules of *n*-butane were diluted with H₂S at different loadings. These are systems 1-3 in Table 4.1. Note that the number of *n*-butane molecules is kept constant for all these simulations. Snapshots for *n*-butane-H₂S systems for the maximum acid gas loading in all simulated substrates are shown in **Figure 4.1**.

Binary systems of *n*-butane-CO₂ and *n*-butane-N₂ were also simulated at different compositions: 300 molecules of *n*-butane were diluted with CO₂ and with N₂ at different loadings. These are systems 4-6 and 7-9 respectively, in Table 4.1. Representative snapshots for *n*-butane-CO₂ and *n*-butane-N₂ systems confined in the three pores are shown in **Figure 4.2** and in **Figure B.2** of Appendix B respectively. The results obtained from the systems described above are compared with a system of pure *n*-butane containing 300 molecules. To study the effect of H₂S-CO₂ mixture and the presence of an inert gas (nitrogen) on the displacement of *n*-butane from the pore surface, ternary systems of *n*-butane - H₂S - CO₂ with varying composition of the acid gases were simulated. These are systems 10-12 in Table 4.1. *n*-butane - acid gas - N₂ systems are systems 13-16 in Table 4.1.

The pressure of the various systems will change as the number of molecules confined in the pores changes. To relate the system composition to bulk pressure, simulations were performed in which the pores are exposed to bulk reservoirs. The

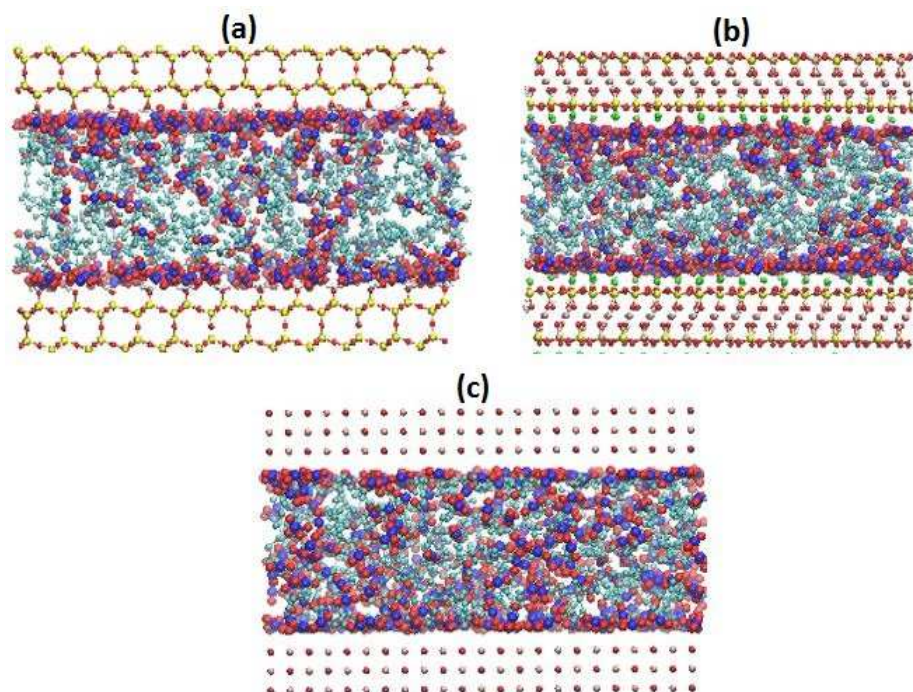


FIGURE 4.2: Simulation snapshots for binary systems containing *n*-butane and CO₂ in silica (a) MgO (b) and muscovite (c). All systems shown contain 300 *n*-butane and 500 H₂S molecules. Cyan spheres are -CH₃ and -CH₂ in *n*-butane, purple are sulphur, white are hydrogen, red are oxygen, yellow are silicon, green are potassium, grey are aluminium, blue are magnesium

number of *n*-butane was constrained inside the pore, while CO₂ or H₂S molecules were allowed to exchange between the pores and the reservoirs. The reservoirs contain H₂S or CO₂ molecules. The bulk pressure was calculated from the density in the reservoir. Details of these simulations are available in section B.2 of Appendix B. The range of pressure for binary systems of *n*-butane–H₂S and *n*-butane–CO₂ in silica, muscovite and MgO are reported in Table 4.2. Pressures for muscovite and MgO pores were similar, while silica pores were at somewhat lower pressures.

TABLE 4.1: Composition of all simulated systems

| System | No of <i>n</i> -butane | No of H ₂ S | No of CO ₂ | No of N ₂ |
|--------|------------------------|------------------------|-----------------------|----------------------|
| 1 | 300 | 200 | - | - |
| 2 | 300 | 375 | - | - |
| 3 | 300 | 500 | - | - |
| 4 | 300 | - | 200 | - |
| 5 | 300 | - | 375 | - |
| 6 | 300 | - | 500 | - |
| 7 | 300 | - | - | 300 |
| 8 | 300 | - | - | 500 |
| 9 | 300 | - | - | 700 |
| 10 | 300 | 250 | 250 | - |
| 11 | 300 | 125 | 250 | - |
| 12 | 300 | 250 | 125 | - |
| 13 | 300 | 400 | - | 100 |
| 14 | 300 | 300 | - | 200 |
| 15 | 300 | - | 400 | 100 |
| 16 | 300 | - | 300 | 200 |

TABLE 4.2: Bulk Pressure corresponding to the system summarised in Table 4.1. For each pore, the lower and upper pressures are reported, as estimated at increasing acid gas loading. For details, please refer to Appendix B2

| Substrate | Pressure/MPa (<i>n</i> -butane-H ₂ S) | Pressure/MPa (<i>n</i> -butane-CO ₂) |
|-----------|---|---|
| Silica | 14.2 ± 0.3 - 7.8 ± 0.3 | 14.0 ± 0.2 - 7.6 ± 0.3 |
| Muscovite | 21.0 ± 0.2 - 11.2 ± 0.2 | 19.2 ± 0.1 - 10.9 ± 0.2 |
| MgO | 23.2 ± 0.2 - 12.1 ± 0.3 | 20.1 ± 0.1 - 11.2 ± 0.2 |

4.3.2 Force field

The CLAYFF force field was implemented to model silica, muscovite, and MgO.[48] N-Butane, and CO₂ were modeled using the TraPPE force field.[49] In TraPPE, CO₂ is rigid with all atoms on a straight line forming a bond angle of 180°. N-butane is flexible, described by angle bending and dihedrals. The united-atom formalism was implemented to describe -CH₃ and -CH₂ groups of *n*-butane. H₂S was described by the model developed by Kamath and Potoff.[51] Nitrogen (N₂) was described as a single LJ sphere without coulombic interactions.[52] The N₂

model implemented here was found to reasonably reproduce the experimental adsorption isotherm of N_2 in silica pores [52]. In all cases, non-bonded interactions were modeled by dispersive and electrostatic interactions. The electrostatic interactions were described by Coulombic potential and the dispersive interactions by 12-6 Lennard-Jones (LJ) potentials. The LJ parameters for unlike atoms were obtained using Lorentz-Berthelot combination rules.[47] The cut-off distance for all interactions was set to 14Å. The particle mesh Ewald method was implemented for long-range corrections to electrostatic interactions.[75]

4.3.3 Algorithms

All simulations were performed within the canonical ensemble, in which the number of molecules, volume, and temperature were maintained constant (NVT). The simulation package GROMACS, version 5.1.2,[76, 77] was used for conducting the simulations. Numerical integration of Newton's equations of motion was carried out using the leapfrog algorithm with a time step of 1fs. The temperature of the solid substrates and of the fluid molecules were controlled separately using two Nosé–Hoover thermostats with relaxation times of 200fs. The simulations were conducted at 350K, a temperature representative of depths between 11,000 and 15,000 feet in sub-surface formations. The total simulation time for each system was in the range of 60-80 ns, depending on the system and the loading. The system was considered equilibrated when *n*-butane and acid gas densities fluctuates around constant value, and the system energy fluctuates within 10% of its average value. Representative data for interaction energy as a function of time for the last

10ns of the simulation for the systems are reported in **Figure B.3** of Appendix B. The results confirms the equilibration of the systems as interaction energy remains stable. The production run was conducted after equilibration and data analysis was performed over the last 10 ns of each simulation.

4.4 RESULTS AND DISCUSSION

4.4.1 Binary Systems: Enhancement of butane displacement by H₂S and CO₂

4.4.1.1 Density profiles

The distribution of fluid molecules in the pore is quantified in terms of the molecular density profiles along the direction orthogonal to the pore surface. The density profiles calculated for the centre of mass (COM) of *n*-butane for pure *n*-butane system and the binary systems at different H₂S, CO₂ and N₂ loadings are shown in **Figure 4.3**. The density profile results show preferential adsorption of *n*-butane on the pore surfaces, as evidenced by the high peak density. The height of the density peak closest to the solid substrate reduces as the H₂S density in the system increases, suggesting that the amount of *n*-butane at contact with the pore surface decreases. The results in **Figure 4.3** also show that adding CO₂ reduces the intensity of the density peak closest to the solid substrate. Conversely, addition of N₂ leaves the density profile relatively unchanged. The density profiles of the hydrogen and sulphur atoms of H₂S and of the carbon and oxygen atoms of CO₂

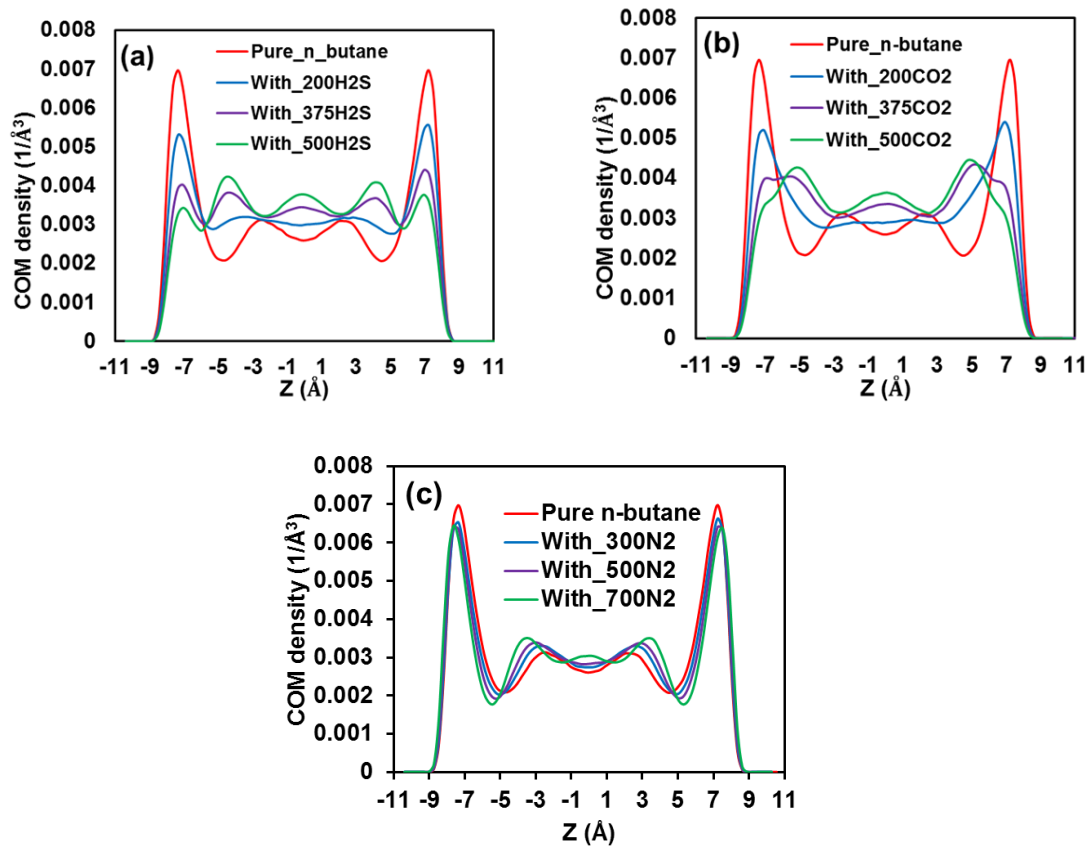


FIGURE 4.3: Density profile of the COM of *n*-butane in the binary system with H₂S loading (a), CO₂ loading (b) and N₂ loading (c). The density profile for a system with pure *n*-butane is also shown for comparison. All systems contain 300 *n*-butane molecules

and of N atom of N₂ in the binary systems considered in **Figure 4.3** are shown in **Figure 4.4**. The distribution of H₂S in the pore is similar to that of CO₂ in the binary systems. At low loading, most of the H₂S and CO₂ in the pore are adsorbed close to the pore surface while at higher loadings, some H₂S and CO₂ molecules occupy regions close to the pore centre, as the pore surface becomes more saturated. The amount of acid gas in the layer close to the pore surface increases with acid gas loading. The density profile of H of H₂S shows that H₂S molecules in the first layer lay with one hydrogen pointing towards the surface while CO₂ molecules lay slightly inclined to the surface. The orientation of the adsorbed acid gases is described in section 4.4.4. To quantify *n*-butane dislocation from silica

TABLE 4.3: Percentage of *n*-butane removed from FAL with H₂S and CO₂ loading

| Loading | % removal (CO ₂ loading) | % removal (H ₂ S loading) |
|---------|-------------------------------------|--------------------------------------|
| 200 | 28 | 34 |
| 375 | 48 | 55 |
| 500 | 58 | 65 |

pore surface, the percentage of *n*-butane removed from the first adsorbed layer (FAL) is calculated using Equation 4.1:

$$\eta_{displaced} = \frac{N_{initial} - N_{gas}}{N_{initial}} \quad (4.1)$$

In Equation 4.1, $N_{initial}$ and N_{gas} represent the amount of *n*-butane in the first adsorbed layer in the system without acid gas and with acid gas respectively. $\eta_{displaced}$ is calculated within the narrow region confined between the position of the first peak in *n*-butane COM density profile and the pore surface. The results are shown in Table 4.3 and confirm that both CO₂ and H₂S aid removing *n*-butane from the pore surfaces. It appears that CO₂ is slightly more effective than H₂S at displacing *n*-butane from silica surface. For completeness, systems of *n*-butane in silica pores in the presence of N₂ were also simulated, without acid gases. The density profiles of COM of *n*-butane and N of N₂ for the binary systems are shown in **Figure 4.3c** and **4.4e**, respectively. The *n*-butane density profiles remain almost unchanged despite the presence of N₂. Even though N₂ density profile in **Figure 4.4e** show adsorption of N₂ close to the pore surface, it is not effective at displacing *n*-butane from the surface. Comparing the density profiles of the acid

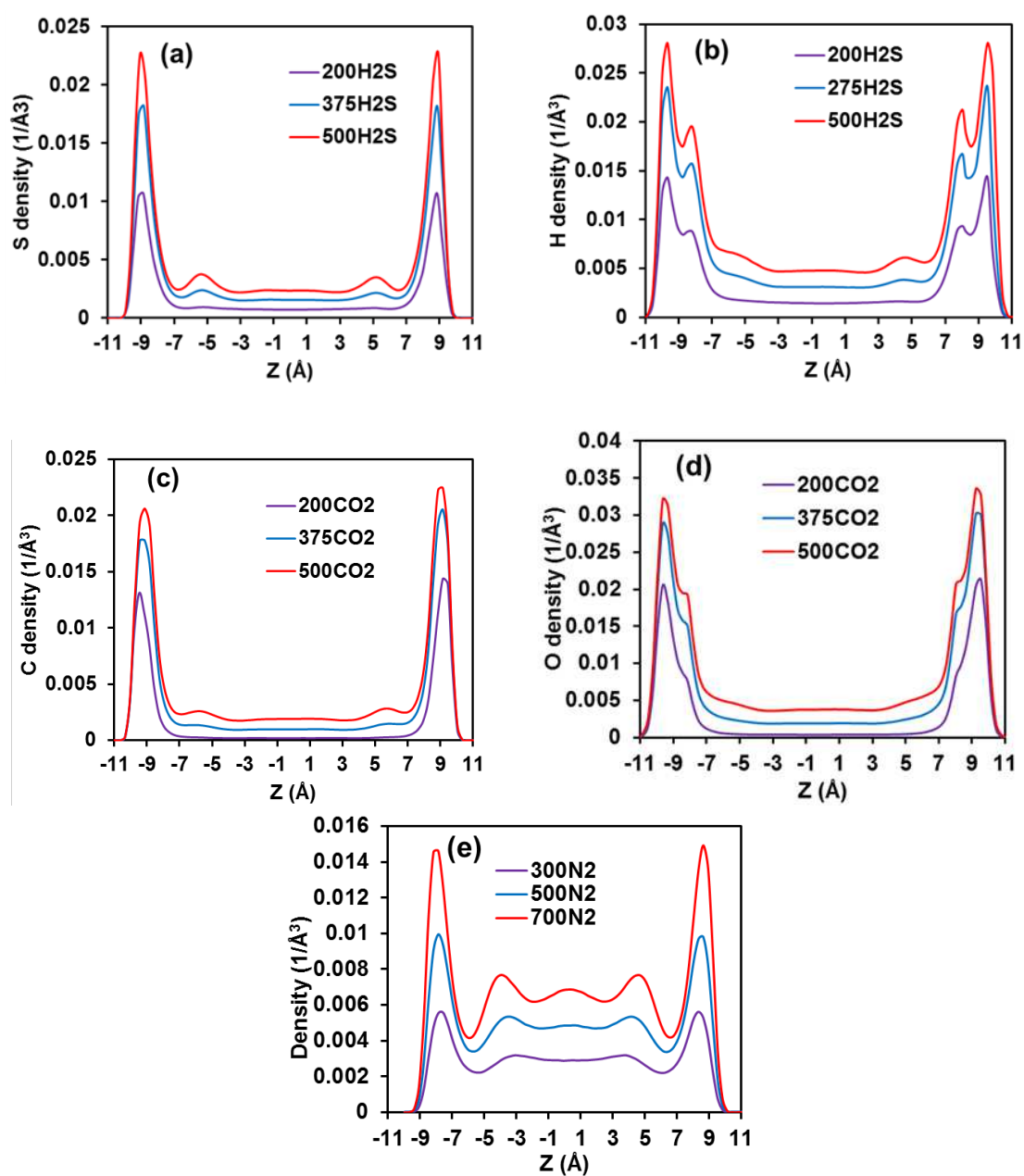


FIGURE 4.4: Density profile of S of H₂S (a) H of H₂S (b) C of CO₂ (c) O of CO₂ (d) and N of N₂ (e) in the binary systems at different acid gas and N₂ loadings in silica pores.

gases in **Figure 4.4a** and **4.4c** to that of N_2 in **Figure 4.4e** shows that the acid gases are more strongly adsorbed on the silica surface than N_2 . The density profile of N_2 in **Figure 4.4e** shows that more N_2 occupy the middle of the pore, where it probably mixes with *n*-butane and potentially reduces its viscosity. To test this latter possibility, bulk systems with densities approximately equal to those in the middle of the pore were simulated. viscosity of *n*-butane was calculated using the procedure described elsewhere, [128] and 0.16cP was obtained for pure *n*-butane and 0.21cP for *n*-butane- N_2 systems containing 200 *n*-butane and 200 N_2 . These results suggest that N_2 increase the viscosity in the simulated pores, which is opposite of what was expected. This however is probably a consequence of the increased density of the confined systems upon N_2 addition.

4.4.1.2 Interaction energy in silica pores

To quantify the fundamental mechanism responsible for the results summarized in Table 4.3, the interaction energy between selected fluid molecules and the silica substrate were calculated. For the *n*-butane-surface interaction energy, corresponding LJ potential was calculated. The Coulombic potential was not considered as *n*-butane molecule is not charged. Plots of interaction energy against time for all fluid molecules over the last 10ns of the simulation times are shown in **Figure B.3** of Appendix B, and show that the interaction energy is stable. The *n*-butane-surface interaction energy normalised by the amount of *n*-butane is shown in Table 4.4. The results are consistent with an attraction between *n*-butane and the pore surfaces (negative interaction energies). The magnitude of the interaction energy

quantifies the strength of the attraction. As H₂S or CO₂ are added to the system, the *n*-butane–surface interaction energy becomes less attractive. This result is qualitatively consistent with the percentage displacement of *n*-butane shown in Table 4.3, as higher percentage displacement correlates with less attractive interaction energy. The interaction of the acid gases with the pore surface is quantified by calculating CO₂–surface and H₂S–surface interaction energies ($E_{CO_2-surface}$ and $E_{H_2S-surface}$). For acid gas–surface interaction energy, both LJ and electrostatic contributions to the interaction energy were considered. The results are normalised by the amount of CO₂ or H₂S in the system. The results, presented in Table 4.5 show that CO₂ is more strongly attracted to the pore surfaces than H₂S. This difference could explain why CO₂ is slightly more effective than H₂S at reducing *n*-butane density near the silica pore surface. The results also indicate that the normalised interaction energy is more attractive when fewer acid gas molecules are present in the system. This is consistent with previous reports for CO₂–CH₄ confined in calcite [30] and in silica pores,[129] and suggest that the first acid gas molecules in the system adsorb on the preferential adsorption sites, possibly via electrostatic interactions related to hydrogen bonds. The formation of hydrogen bonds between the acid gases and the –OH groups on the surface was not analysed in this study. It has been reported that CO₂ can form hydrogen bond with water [130], suggesting the possibility of hydrogen bonding between CO₂ and –OH groups on silica surface. For the specific conditions considered, the preferential adsorption sites are expected to be the –OH groups on the silica surface. Analysis of the simulations suggests that 232 CO₂ and 238 H₂S molecules saturate each of the two pore surfaces available on the silica substrate. Density profiles in **Figure**

TABLE 4.4: N-butane interaction energy with the silica surface. All systems contain 300 *n*-butane molecules

| Acid gas loading | With H ₂ S (kJ/mol) | With CO ₂ (kJ/mol) |
|-----------------------|--------------------------------|-------------------------------|
| 200 | -3.13 ±0.01 | -3.11 ±0.01 |
| 375 | -2.65 ±0.02 | -2.51 ±0.02 |
| 500 | -2.37 ±0.02 | -2.23 ±0.01 |
| Pure <i>n</i> -butane | -3.74 ±0.01 | |

4.4 show that some CO₂ or H₂S molecules occupy the region close to the centre of the pore even before the surface becomes saturated due to increase in peak intensity in the density profiles with acid gas loading, suggesting some exchange between gas molecules adsorbed on the pore surfaces and those at the middle of the pore.

4.4.1.3 Residence times

To further characterise the systems considered in **Figure 4.3**, the residence time correlation function (RCF), $C_R(t)$, for *n*-butane molecules found within a layer of thickness 5Å from the pore surface was calculated. Molecules found in this region belong to the first adsorbed layer. The $C_R(t)$ is defined as[131]:

$$C_R(t) = \frac{\langle N_i(t)N_i(0) \rangle}{\langle N_i(0)N_i(0) \rangle} \quad (4.2)$$

In Equation 4.2, $N_i(t)=1$ if molecule *i* resides in the layer considered at time *t*, and 0 otherwise. $N_i(0)=1$ if molecule *i* belongs to the layer at time *t*=0 and becomes 0 only when molecule *i* leaves the layer and remains equal to zero even though the molecule returns to the layer. The faster $C_R(t)$ decays from 1 to 0 the faster molecules leave the layer considered, which is the first adsorbed layer. The

COM of butane is used to represent the position of one *n*-butane molecule in this calculation. The calculated $C_R(t)$ for *n*-butane molecules in the first layer as a function of H₂S and CO₂ loading are shown in **Figure 4.5** (a and b) respectively. The results show that in both *n*-butane – H₂S and *n*-butane – CO₂ systems, the autocorrelation functions decay to zero faster as the acid gas loading increases. Comparing results obtained for H₂S with that of CO₂ at the same loading shows faster decays in the presence of CO₂. This suggests that the interactions between CO₂ and the pore surface weaken the *n*-butane–surface interactions more effectively than those between H₂S and the surface. This supports the claim earlier made that CO₂ is slightly more effective at displacing *n*-butane from silica surface.

The $C_R(t)$ for H₂S and CO₂ molecules in the first adsorbed layer are shown in **Figure 4.5c** and d. The C of CO₂ and the S of H₂S were chosen to identify CO₂ and H₂S respectively for the $C_R(t)$ calculation. The results show that the residence times of acid gas molecules in the first adsorbed layer decreases as acid gas loading increases. This is probably due to fast exchange between acid gas molecules in the adsorbed layer and those close to the centre of the pore. This observation is consistent with previous reports in literature [32], with the density profiles, and also with the interaction energies discussed in section 4.4.1.2 above.

TABLE 4.5: Acid gas – Surface interaction energy in silica pores normalised by acid gas loading

| Loading | H ₂ S | | CO ₂ | |
|---------|------------------------|-------------|------------------------|-------------|
| | Electrostatic (kJ/mol) | LJ (kJ/mol) | Electrostatic (kJ/mol) | LJ (kJ/mol) |
| 200 | -10.63 ±0.09 | -2.77 ±0.01 | -18.0 ±0.1 | -4.1 ±0.02 |
| 375 | -9.31 ±0.05 | -2.57 ±0.01 | -13.5 ±0.1 | -3.4 ±0.01 |
| 500 | -8.54 ±0.03 | -2.42 ±0.01 | -11.2 ±0.2 | -2.9 ±0.01 |

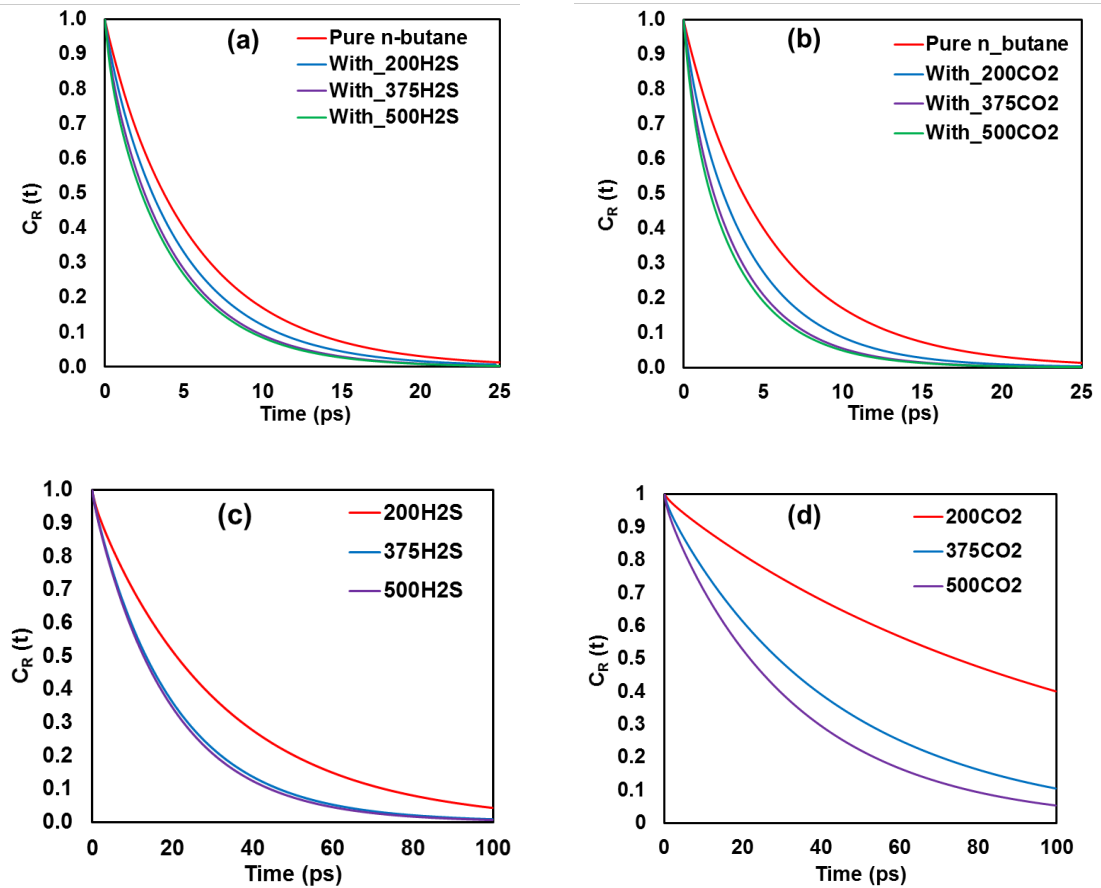


FIGURE 4.5: RCF for n -butane molecules in the first layer at different H₂S loading (a) and CO₂ loading (b). The RCF for system containing pure n -butane is also shown for comparison. RCF of H₂S molecules in the first layer at different loading are shown in (c) and for CO₂ molecules at different loading in (d)

4.4.2 Ternary systems

4.4.2.1 Effect of H₂S-CO₂ mixture on *n*-butane displacement

To investigate whether mixtures of H₂S and CO₂ could act synergistically in terms of *n*-butane displacement from the pore surfaces, the effect of 50%-50% mixtures of CO₂ and H₂S in the presence of *n*-butane (system 10 in Table 4.1) was quantified. The density profiles for *n*-butane in these systems are compared in **Figure 4.6a**. The results show that the distribution of *n*-butane in the presence of the H₂S-CO₂ mixture is between those obtained when either CO₂ or H₂S is present at similar loading, yielding a % removal of $\sim 62\%$. Therefore, the results suggest that mixing the acid gases is not synergistic, but rather reduces the ability of CO₂ to displace *n*-butane from the pore surfaces by $\sim 5\%$. This is consistent with the report of Khan et al.,[116] who used reservoir simulations to quantify the effect of acid gas injection on enhanced gas recovery. Results for the *n*-butane $C_R(t)$, shown in **Figure 4.6b**, are also consistent with the density profiles of *n*-butane just discussed.

To further understand the performance of H₂S-CO₂ mixtures at the displacement of *n*-butane from silica pore surfaces, additional ternary systems with fraction of the acid gas varied were simulated while maintaining a constant acid gas loading of 375 molecules. CO₂:H₂S ratios of 1:2 and 2:1 were considered. These systems are 11 and 12 in Table 4.1. The density profiles for the systems are presented in **Figure 4.6c** and show that the higher the CO₂ fraction in the acid gas mixture, the better the performance of the acid gas mixture at displacing *n*-butane from

silica surface. This is consistent with the claim that CO₂ is better at displacing *n*-butane from silica surface than H₂S.

4.4.2.2 Effect of acid gas-N₂ mixture on *n*-butane displacement

The results discussed so far in this Chapter suggest that the ability of CO₂ and H₂S to displace hydrocarbons from silica surface is related to their strong attractions with the pore walls, sometimes due to electrostatic interactions. To further test this observation, additional simulations were conducted in which an inert

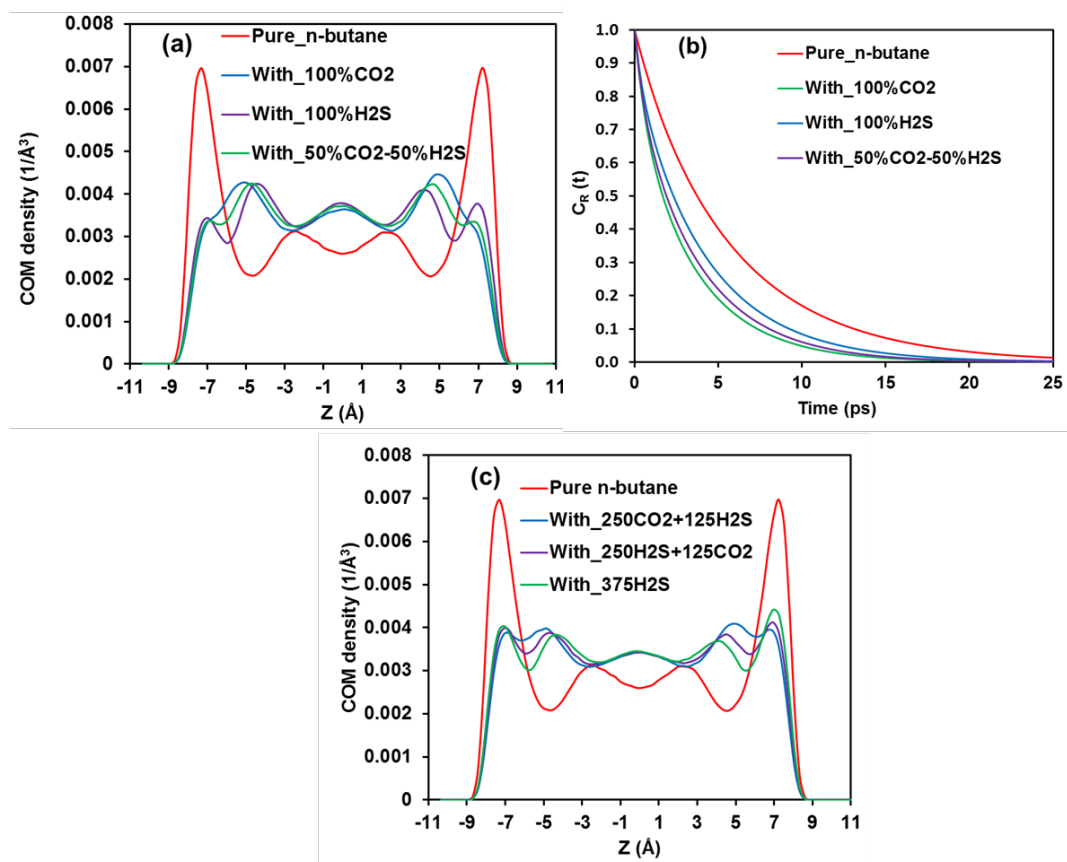


FIGURE 4.6: Comparison of density profiles of *n*-butane in the presence of pure acid gas and their mixture (a) and RCF for the same system (b). The binary systems comprises 300 *n*-butane and a total of 500 molecules of the acid gas. The mixture comprises 250 molecules of each acid gas. Density profiles of *n*-butane for varying composition of acid gas is shown in (c). The systems in (c) have a total acid gas loading of 375 and 300 molecules of *n*-butane

gas (nitrogen) was added to various binary systems. Simulations were conducted for 80%CO₂-20%N₂ and 60%CO₂-40%N₂ for a total gas loading of 500 molecules (systems 15 and 16 shown in Table 4.1). The same set of simulations were also conducted for mixture of H₂S and N₂ (systems 13 and 14 of Table 4.1 for composition). The results are shown in **Figure 4.7**. The density profiles for COM of *n*-butane are shown in **Figure 4.7** (a and b) and those for C of CO₂, S of H₂S and N of N₂ in **Figure 4.7** (c and d). The estimated % removal for the various systems is shown in **Figure 4.7** (e and f). The results show that as N₂ fraction in the mixture increases, the % removal decreases suggesting that N₂ does not contribute to the displacement of *n*-butane from silica surface.

4.4.3 Effect of Pore Surface Chemistry

4.4.3.1 Density profiles and percentage removals

It is possible that the behaviour of fluids confined within narrow pores depends on the nature of the confining surface. To investigate whether the performance of the acid gases depends on the nature of the substrate, additional simulations were performed in muscovite and magnesium oxide (MgO). The system composition is the same as in the case of silica reported in Table 4.1. The number of *n*-butane molecules was kept at 300. It should be noted that the bulk pressures for *n*-butane – CO₂ and *n*-butane – H₂S are similar (see Table 4.2). The density profiles for *n*-butane at different acid gas and N₂ loadings in muscovite and MgO are shown in **Figure 4.8**. The calculated % removals of *n*-butane from the pore surfaces

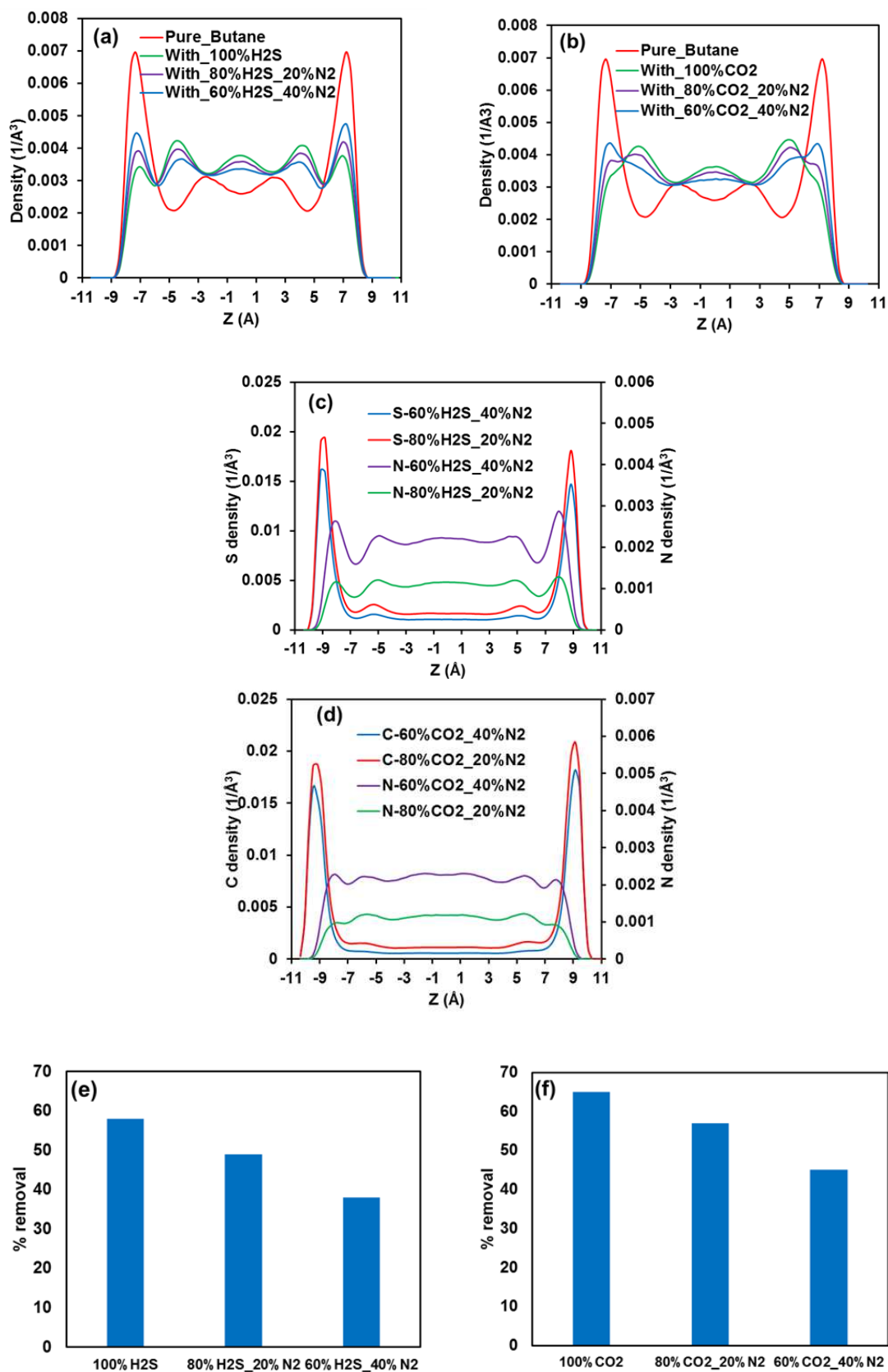


FIGURE 4.7: Density profiles for COM of *n*-butane for (a) H₂S - N₂ system (b) CO₂ - N₂ system. Density profiles for N of N₂ for (c) H₂S - N₂ (d) CO₂ - N₂ systems. There are 300 *n*-butane molecules in all cases. The total number of gas molecules is 500. Percentage of hydrocarbon displaced is also shown for H₂S - N₂ (e) and CO₂ - N₂ systems (f)

based on the density profiles are presented in Table 4.6. The results show that addition of H₂S into muscovite pores displaced up to 98 % of original *n*-butane in the FAL, while in MgO, only about 21 % of the original *n*-butane in the FAL is displaced. Addition of CO₂ displaces about 86% and 21% of original *n*-butane in FAL in muscovite and MgO respectively. The results in Table 4.6 demonstrate that H₂S performs better than CO₂ at displacing *n*-butane in muscovite, while CO₂ performs better than H₂S in silica as previously explained in this Chapter. Both CO₂ and H₂S show similar performance in MgO pores. It is obvious from the density profiles in **Figure 4.8** (e and f) that addition of N₂ into muscovite and MgO does not result in displacement of *n*-butane from the surface. Hence, N₂ is not efficient for displacing *n*-butane from the surfaces. Similar result was obtained for systems containing N₂ in silica pores (see **Figure 4.3c**). It should be noted that the pressures considered in the silica substrate (see Table 4.2) are somewhat different compared to those considered in the other two substrates. However, because the results are due to preferential fluid–surface interactions, this difference is not expected to affect qualitatively the results presented. These results are certainly dependent on the protonation states of the surfaces considered here, as these affect the interactions between the various fluid molecules and the pore surfaces. Because water was not considered in all systems, effect of varying surface protonation on the results is not explicitly quantified.

The density profiles of carbon and oxygen of H₂S, sulphur and hydrogens of H₂S and N of N₂ for binary systems in muscovite and MgO pores are presented in **Figure 4.9** and **Figure 4.10** respectively. In all cases, H₂S and CO₂ are preferentially

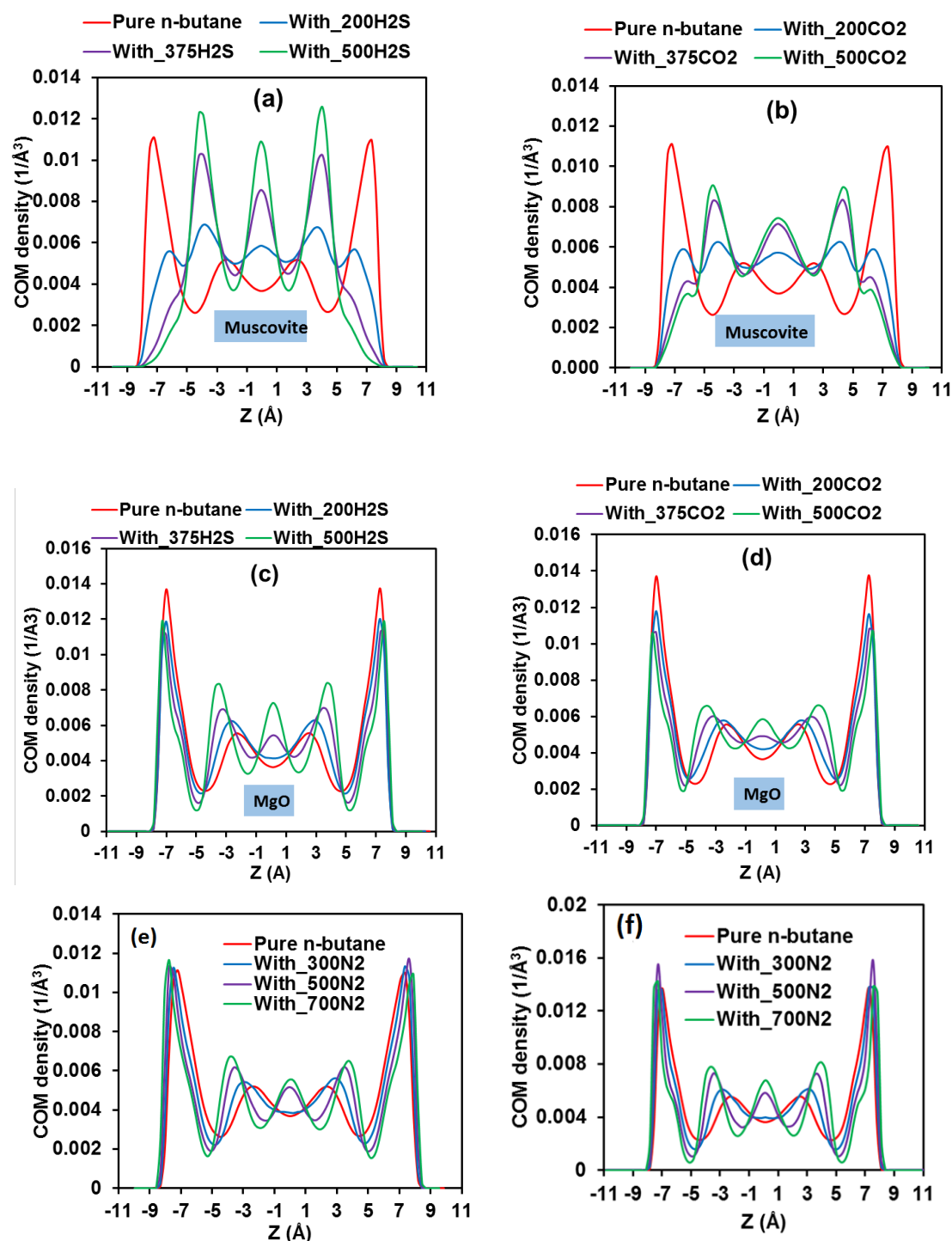
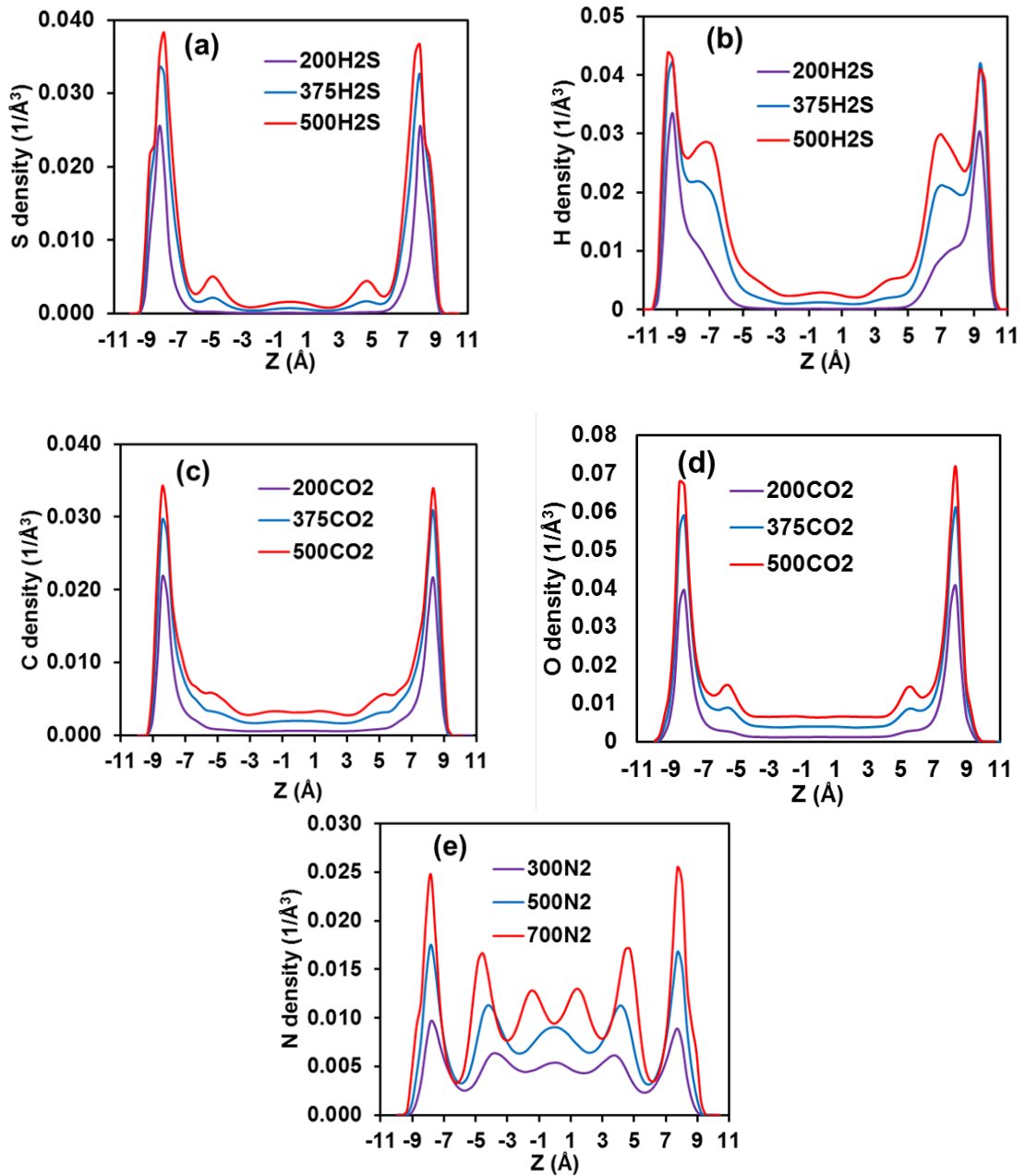


FIGURE 4.8: N-butane density profiles at different acid gas loadings for H₂S in muscovite (a) CO₂ in muscovite (b) H₂S in MgO (c) and CO₂ in MgO (d). Density profiles of *n*-butane at different N₂ loadings in muscovite (e) and MgO (f). All systems comprises 300 *n*-butane molecules

TABLE 4.6: Percentage of *n*-butane displaced from FAL in all simulated substrates for acid gas injection at different acid gas loading

| Loading | Muscovite | | Magnesium oxide | | Silica | |
|---------|------------------|-----------------|------------------|-----------------|------------------|-----------------|
| | H ₂ S | CO ₂ | H ₂ S | CO ₂ | H ₂ S | CO ₂ |
| 200 | 73 | 62 | 13 | 11 | 28 | 34 |
| 375 | 94 | 81 | 16 | 17 | 48 | 55 |
| 500 | 98 | 86 | 21 | 24 | 58 | 65 |

FIGURE 4.9: Density profile of S of H₂S (a) H of H₂S (b) C of CO₂ (c) O of CO₂ (d) and N of N₂ (e) in the binary systems at different acid gas and N₂ loadings in muscovite pores.

adsorbed on the surfaces. The results in general show that the acid gases show preferential adsorption on muscovite and MgO pore surfaces while fewer molecules occupy the middle of the pores. The amount of acid gas adsorbed on the surfaces and in the middle of the pore increases with acid gas loading. The results in **Figure 4.9** and **4.10** show that H₂S and CO₂ adopt different orientation on muscovite and MgO surface similar to that of silica. This is discussed in details in the later section of this chapter.

4.4.3.2 Interaction energy

Results for *n*-butane–surface interaction energies (shown in **Figure 4.11**) show that both CO₂ and H₂S reduce *n*-butane–surface attractions in all substrates considered as *n*-butane interaction energy decreases with acid gas loading. The reduction in *n*-butane–surface interaction energy upon acid gas addition is somewhat not significant in MgO. The results for the normalised interaction energies between the acid gases and the substrates are shown in **Figure 4.12** and show that while CO₂ is more strongly attracted to silica than H₂S, H₂S is more strongly attracted to muscovite than CO₂. Both acid gases have similar interaction with MgO. These results suggest that the more strongly a gas is attracted to a porous substrate, the more effective that gas is expected to be at displacing hydrocarbons from the corresponding pore surface.

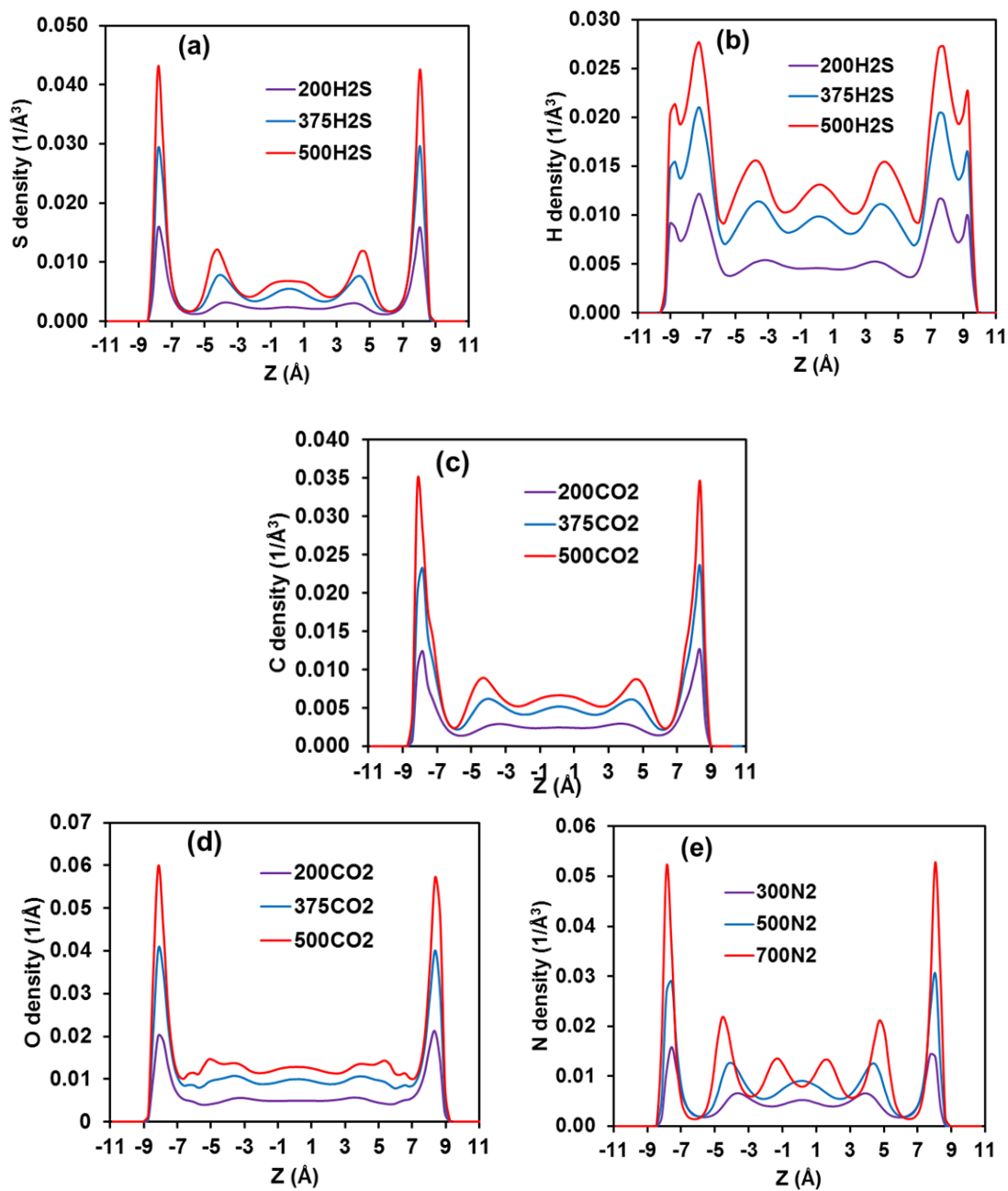


FIGURE 4.10: Density profile of S of H_2S (a) H of H_2S (b) C of CO_2 (c) O of CO_2 (d) and N of N_2 (e) in the binary systems at different acid gas and N_2 loadings in MgO pores.

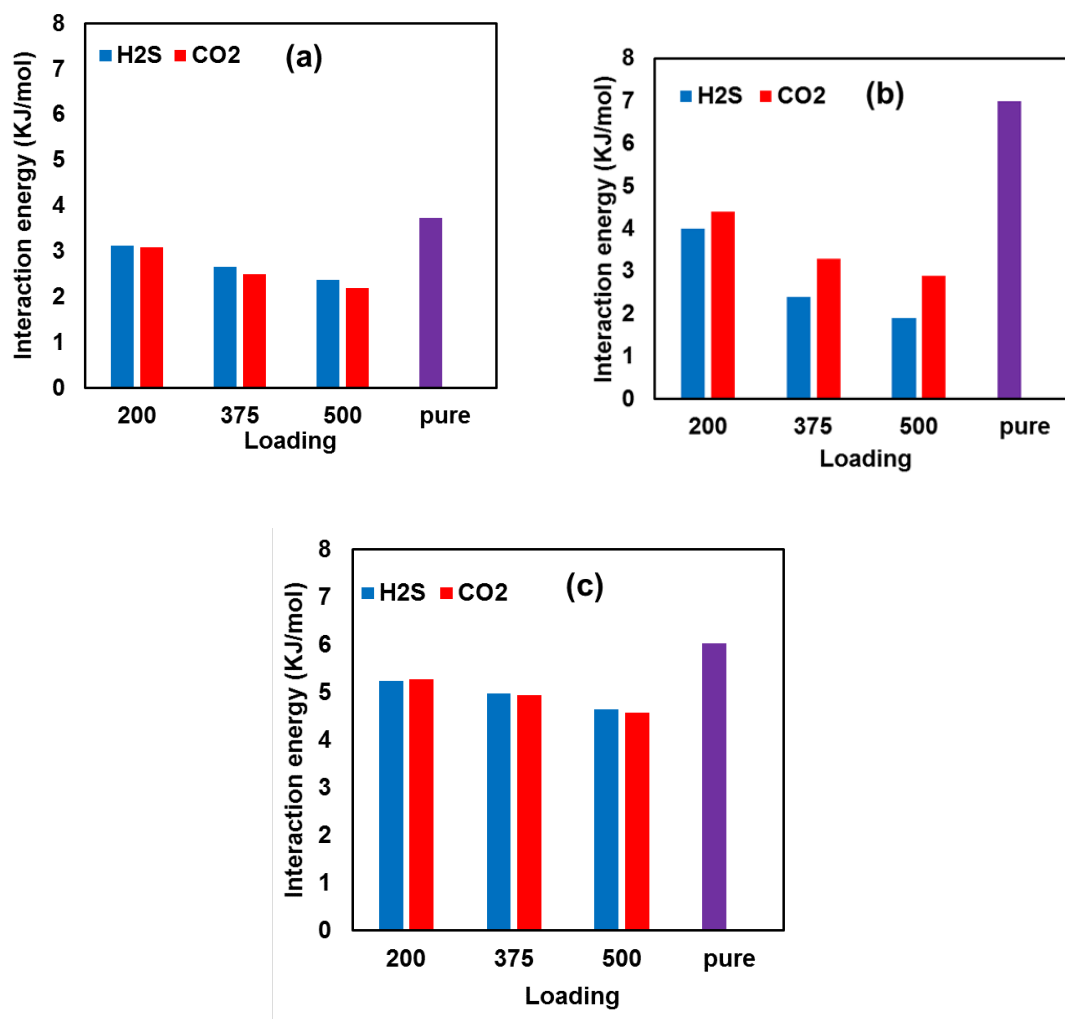


FIGURE 4.11: Magnitude of total interaction energy of *n*-butane at different acid gas loading for silica (a) muscovite (b) and MgO (c). The systems comprise 300 *n*-butane molecules and each of the acid gas. The interaction energies are normalised by the number of *n*-butane molecules in the system. The interaction energy shown is only due to van der Waals interaction as *n*-butane molecules bear no charge

4.4.3.3 Residence times

The RCF for *n*-butane in muscovite and MgO pores are shown in **Figure B.4** of Appendix B. In muscovite, *n*-butane residence time decreases with H₂S loading while RCF curves essentially overlap with CO₂ loading, suggesting that *n*-butane exchange between adsorbed molecules close to the pore walls and at the pore centre occurs at the same frequency irrespective of the amount of CO₂ in the

system. However, the residence times are always less than that of pure *n*-butane for all loadings considered. On the other hand, in MgO, residence times of *n*-butane increases with CO₂ and H₂S loading and always greater than the residence time of pure *n*-butane. For silica (previously discussed), residence time of *n*-butane decreases with CO₂ and H₂S loading and always less than residence time of pure *n*-butane. The residence time results in the various substrate could in part, explain why the acid gases perform relatively better in silica and muscovite with maximum percentage removal of 98% and 65% in muscovite and silica respectively. In MgO, the maximum percentage removal obtained was 24%. The results just discussed suggests that the interaction between adsorbed *n*-butane molecules in the first layer and those near the middle of the pore affects the residence time of *n*-butane in the first layer. In silica and muscovite, addition of the acid gases results in significant increase in the density of *n*-butane close to the centre of the pore due to substantial displacement of the adsorbed *n*-butane molecules. In MgO, the density of *n*-butane at the middle of the pore remains relatively unchanged, and the residence time of *n*-butane in the first layer increases upon CO₂ and H₂S loading. This increase might be a consequence of overall increase in the density of fluid confined within the pores.

In general, the results discussed so far in this Chapter suggests that for dry systems, it is possible to discover gases that could effectively displace short linear hydrocarbon from pore surfaces by considering the interactions of such gases with the solids. The gases that are more strongly attracted to the pore surfaces are

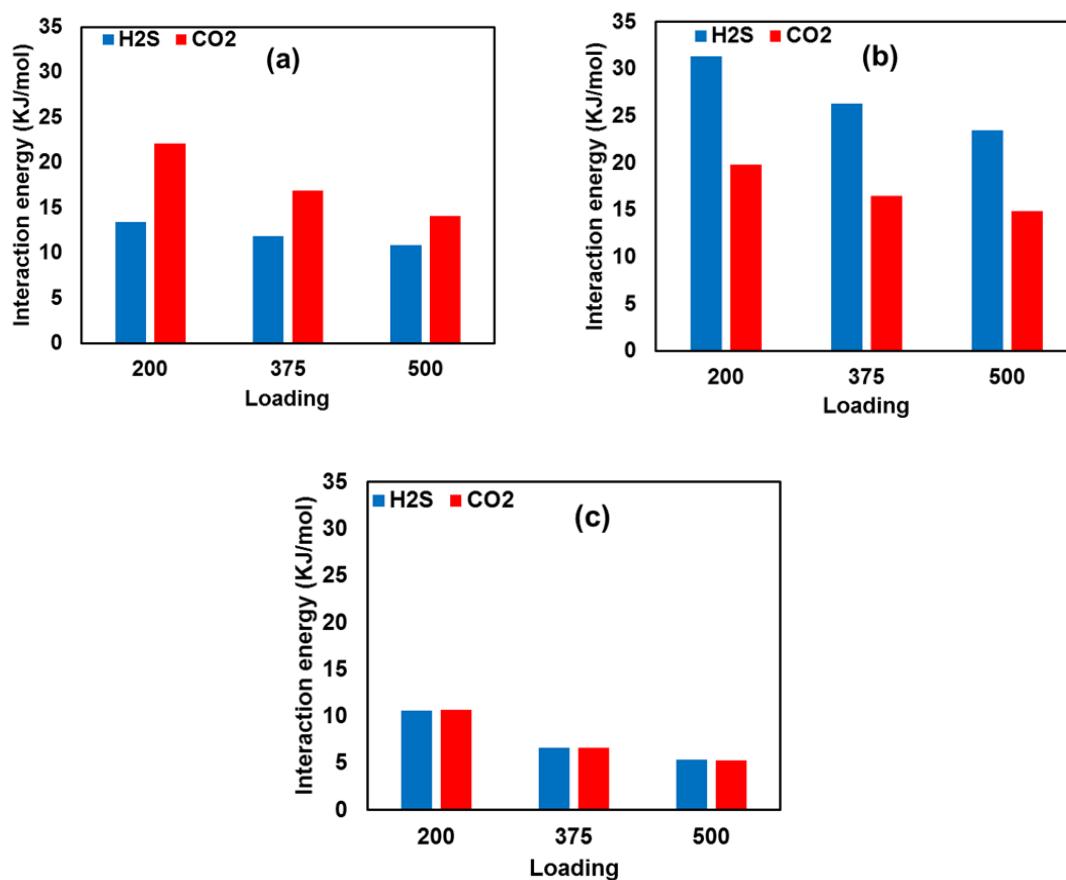


FIGURE 4.12: Magnitude of total interaction energy of acid gases at different acid gas loading for silica (a) muscovite (b) and MgO (c). The systems comprise 300 *n*-butane molecules and each of the acid gas. The interaction energies are normalised by the number of acid gas molecules in the system. The interaction energy shown is the sum of the LJ and electrostatic contributions.

likely to be more effective at displacing the hydrocarbons. Because realistic materials are heterogeneous, lab-scale experimental tests should be conducted before field campaigns.

4.4.3.4 Effect of Nitrogen

Additional simulations were conducted in which nitrogen was added to *n*-butane confined in muscovite and MgO. The density profiles shown in **Figures B.5** and **B.6** of Appendix B, are consistent with those discussed for silica pores as density

profiles seem to overlap with N₂ loading. The results suggest that N₂ has little or no effect on *n*-butane displacement from the pore surfaces. In all cases, nitrogen seems to preferentially distribute near the pore centre.

4.4.4 Molecular Structure of Adsorbed Gases

The results discussed in previous sections demonstrate that different gases can have various effects in displacing short linear hydrocarbons from pore surfaces because of their different interactions with the pore surfaces. Because the interaction energies depend on the various chemical species found on the pore surface, it is of fundamental interest to quantify how the various fluid molecules assemble within a pore, with relevance to the distribution of the atomic species on the solid substrate. Gas molecules adsorbed within the FAL were considered because of the relevance of the FAL in determining the distribution and the diffusion coefficients of various fluid molecules within narrow pores.[32]

4.4.4.1 Orientation of adsorbed gases in the first adsorbed layer

To gain insight into the relation between the structure of adsorbed acid gas and its ability to displace *n*-butane from the pore surface, preferential orientation of the adsorbed CO₂ and H₂S molecules in contact with all simulated substrates was calculated. The results are shown in **Figure 4.13**. The molecules considered in the calculation are those found within 2Å from silica and muscovite surface and 5Å from MgO surface. The results are obtained at the pore maximum loading

condition. The thickness of the adsorbed layers considered (5\AA and 2\AA) are chosen based on the density profiles of the gas molecules to focus on the FAL. The orientation of CO_2 molecules were quantified in terms of the distribution of the angle θ , formed between CO_2 backbone and the normal to the surface. If θ is equal to 0° or 180° , CO_2 is perpendicular to the surface, when it is 90° , CO_2 lays parallel to the surface. For H_2S , the distribution of the angle θ , formed between the vector pointing from S to the midpoint of the H-H vector and the normal to the surface is presented. When θ is equal to 0° , H_2S points the two hydrogens away from the surface, and when it is equal to 180° , H_2S points both hydrogens towards the surface. When θ is 90° , H_2S either points one hydrogen to the surface or lays parallel to the surface. **Figure 4.13** show that the acid gases adopt different orientation on each of the substrate. In the bulk, where there is no preferred orientation, the angle distribution is expected to be isotropic, and the corresponding angle distribution is also shown in **Figure 4.13** for comparison. On silica, CO_2 lays at an angle of $\sim 75^\circ$ to the surface. A similar orientation of CO_2 has been previously reported for silica.[114] For muscovite and MgO , in the models considered here, CO_2 lays parallel to the surface. On the other hand, H_2S on muscovite is almost in 2-hydrogen down orientation, while on silica and MgO , its orientation seems to be with either one hydrogen towards the surface or parallel to it. Both CO_2 and H_2S molecules adsorbed close to each of the surfaces considered show anisotropy in the angle distribution when compared to an isotropic distribution, and this indicates that there is preferred orientation for the adsorbed gases. The results in general show that the nature of the substrates dictates the structure of the adsorbed gas, which could influence the EOR performance of the

gas. For example, H_2S tends to perform better than CO_2 in muscovite where it almost points its two hydrogen atoms towards the surface when compared to its performance in silica where it preferentially points one hydrogen down or lays parallel to the surface. Note that CO_2 performs better than H_2S in silica. This suggests that H_2S could be effective at displacing hydrocarbons from substrates in which active sites are available on the solid surfaces where both hydrogen atoms of H_2S could be strongly attracted.

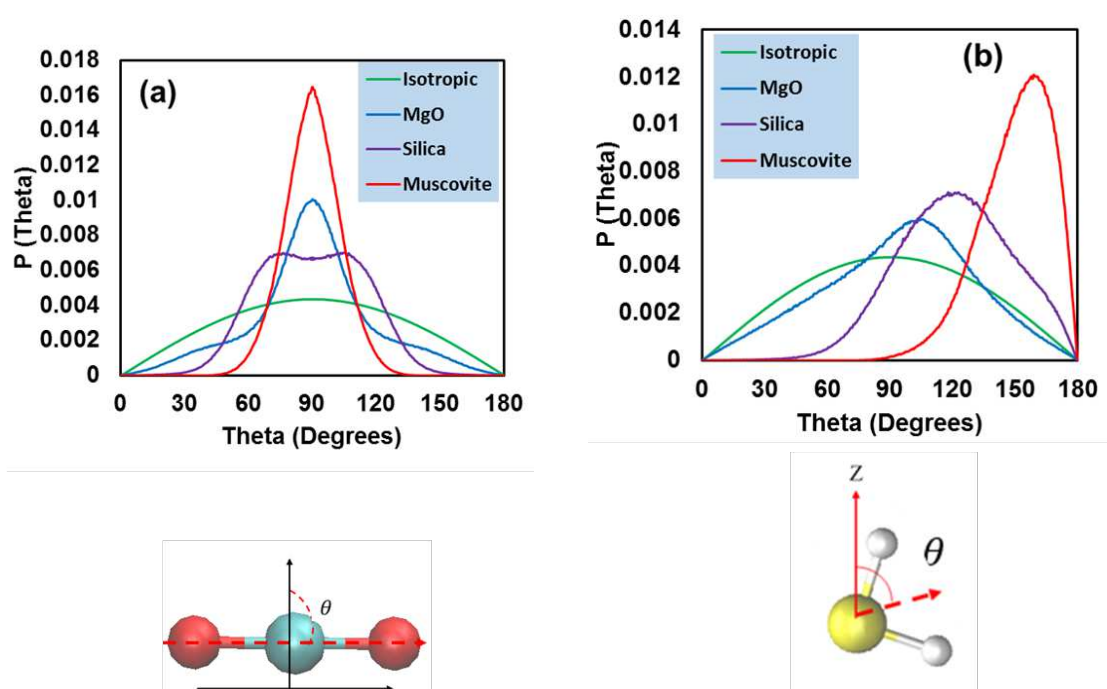


FIGURE 4.13: Probability distribution of angle theta for CO_2 molecules (a) and H_2S molecules (b) adsorbed within 2\AA from silica and muscovite surfaces and 5\AA from MgO surface. The results are compared with the isotropic distribution. All systems contain 300 *n*-butane and 500 acid gas molecules

4.4.4.2 Planar density distribution

To further quantify how the solid substrates determine the distribution of H_2S and CO_2 within the FAL, the in-plane density distributions of the gases are calculated which are then related to the distribution of atoms on the surfaces. In **Figure 4.14**,

the in-plane density distribution of sulphur (S) of H₂S in all simulated substrates is shown. The correspondent results for hydrogen atoms (H) of H₂S are shown in **Figure B.7** of Appendix B. The results reveal preferential adsorption sites for H₂S and CO₂. For example, in silica, S of H₂S preferentially interacts with the vertices of the hexagonal ring formed by the silicon atoms of the substrate. In muscovite, it preferentially adsorbs on the hydroxyl groups in muscovite interlayer. On the other hand, for MgO, S of H₂S adsorbs near the oxygen atoms on the surface.

The in-plane distribution of C of CO₂ in all simulated substrates is shown in **Figure 4.15**. The distribution of the oxygen atoms of CO₂ are shown in **Figure B.8** of Appendix B. In silica and muscovite, the high density regions correspond to the location of silicon atoms in both substrates. In MgO, these regions correspond to the region between two oxygen atoms in the substrate as the oxygen atoms of CO₂ preferentially adsorb close to the oxygen atoms in MgO (see **Figure B.8**). The density of the gas on the various substrates correlates with the strength of interaction with the surface, which could influence its performance at *n*-butane displacement from the surface. The results in **Figures 4.14** and **4.15** show that fewer acid gas molecules are adsorbed on MgO surfaces compared to other substrates and that could explain why the acid gases perform poorly at *n*-butane displacement from MgO surfaces.

4.4.4.3 Diffusion Coefficient of confined fluids

To quantify diffusion coefficients, mean square displacements (MSDs) were calculated following established procedures.[59] From the MSD of the COM of *n*-butane,

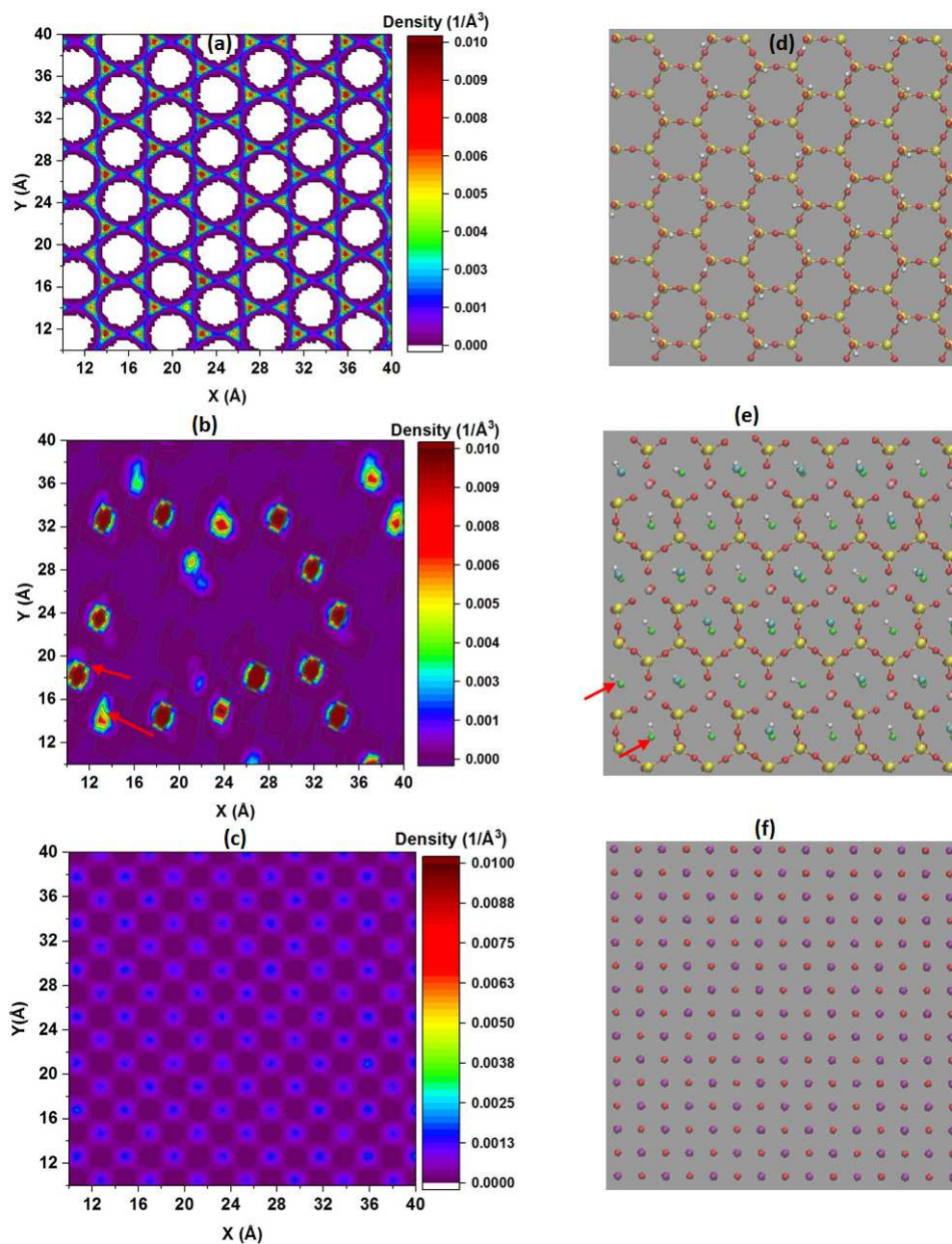


FIGURE 4.14: In-plane density distribution of S of H₂S in silica (a) muscovite (b) and MgO (c). Snapshot of a section of silica (d) muscovite (e) and MgO (f) are also shown. All systems contain 500 H₂S and 300 *n*-butane

acid gases, and N₂ as a function of time, diffusion coefficients were determined.

It should be noted that simulation box size affects diffusion coefficient estimates from MD simulation [132–134] and an analytical correction that is proportional to $N^{-1/3}$ (N is number of molecules) has been proposed.[133] The MSD of COM of *n*-butane for binary systems of *n*-butane–H₂S and *n*-butane–CO₂ in all substrates

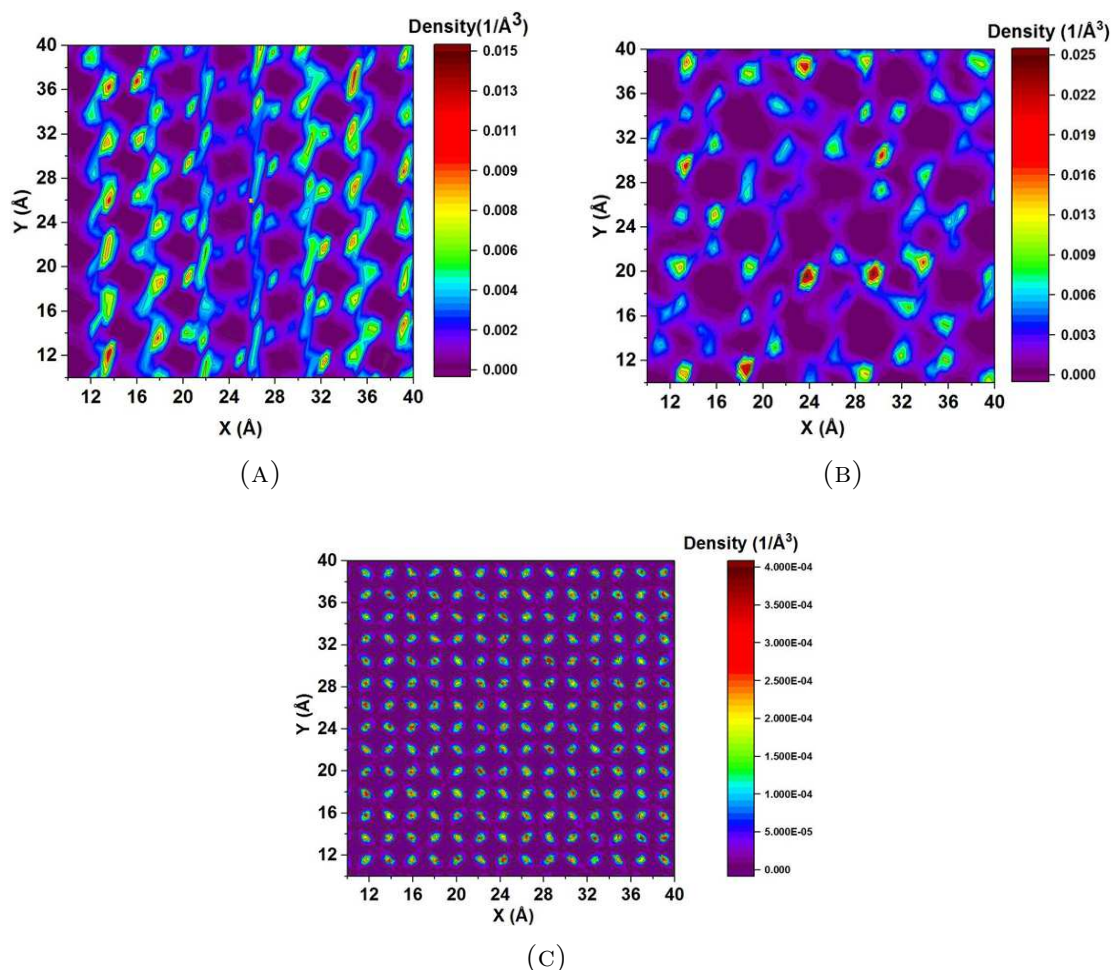


FIGURE 4.15: In-plane density distribution of C of CO₂ in silica (a) muscovite (b) and MgO (c). All systems contain 500 H₂S and 300 *n*-butane

are shown in **Figure 4.16**. The MSD plots of CO₂ and H₂S are shown in **Figure B.9** of Appendix B and those of *n*-butane and N₂ for *n*-butane–N₂ systems are shown in **Figure B.10** of Appendix B. The diffusion coefficients calculated from the MSD plots are shown in Tables 4.7 – 4.9. The results show that CO₂, H₂S and N₂ in general, slow down the diffusion of *n*-butane in all simulated substrates probably due to pore crowding. An exception is in the case of the lowest CO₂ loading (200 CO₂) in silica, wherein the self diffusion coefficient obtained for *n*-butane is slightly higher than that observed for pure *n*-butane when no CO₂ is present.

TABLE 4.7: Self-diffusion coefficient for *n*-butane, acid gases and N₂ in silica pores. The system composition is shown in Table 4.1

| System | D(<i>n</i> -butane) (10 ⁻⁸ m ² /s) | D(H ₂ S) (10 ⁻⁸ m ² /s) | D (CO ₂) (10 ⁻⁸ m ² /s) | D (N ₂) (10 ⁻⁸ m ² /s) |
|-----------------------|--|---|--|---|
| 1 | 6.5 ±0.1 | 1.8 ±0.02 | - | - |
| 2 | 6.2 ±0.2 | 1.5 ±0.02 | - | - |
| 3 | 5.5 ±0.2 | 1.3 ±0.04 | - | - |
| 4 | 7.0 ±0.4 | - | 0.6 ±0.03 | - |
| 5 | 6.4 ±0.3 | - | 1.0 ±0.01 | - |
| 6 | 6.6 ±0.4 | - | 1.1 ±0.01 | - |
| 7 | 5.8 ±0.2 | - | - | 4.2 ±0.05 |
| 8 | 5.8 ±0.2 | - | - | 2.6 ±0.04 |
| 9 | 5.2 ±0.1 | - | - | 2.0 ±0.04 |
| Pure <i>n</i> -butane | 6.5 ±0.2 | - | - | - |

To check whether CO₂ could enhance the *n*-butane diffusion at lower loading (molecular lubrication), additional systems where 300 *n*-butane molecules were diluted with either 125 or 75 CO₂ molecules were simulated. The results obtained are 6.4 x 10⁻⁸ and 6.5 x 10⁻⁸ m²/s for *n*-butane diffusion coefficient when 75 and 125 CO₂ molecules were present within the silica pore respectively. These results are similar to those obtained for pure *n*-butane, suggesting that CO₂ could enhance *n*-butane mobility, but pore crowding quickly suppresses this effect, at the conditions considered in this report. For completeness, the self-diffusion coefficients obtained for CO₂ when either 75 or 125 CO₂ molecules were present in silica pores containing 300 molecules of *n*-butane were found to be 2.7 x 10⁻⁹ and 3.9 x 10⁻⁹ m²/s, respectively.

The results in Tables 4.7 – 4.9 show that H₂S and CO₂ have lower self-diffusion coefficients than *n*-butane reflecting the stronger interaction of the gases with the substrates than *n*-butane, as discussed above. The results suggest that H₂S travels faster than CO₂ through the silica pores, consistent with the weaker attraction to

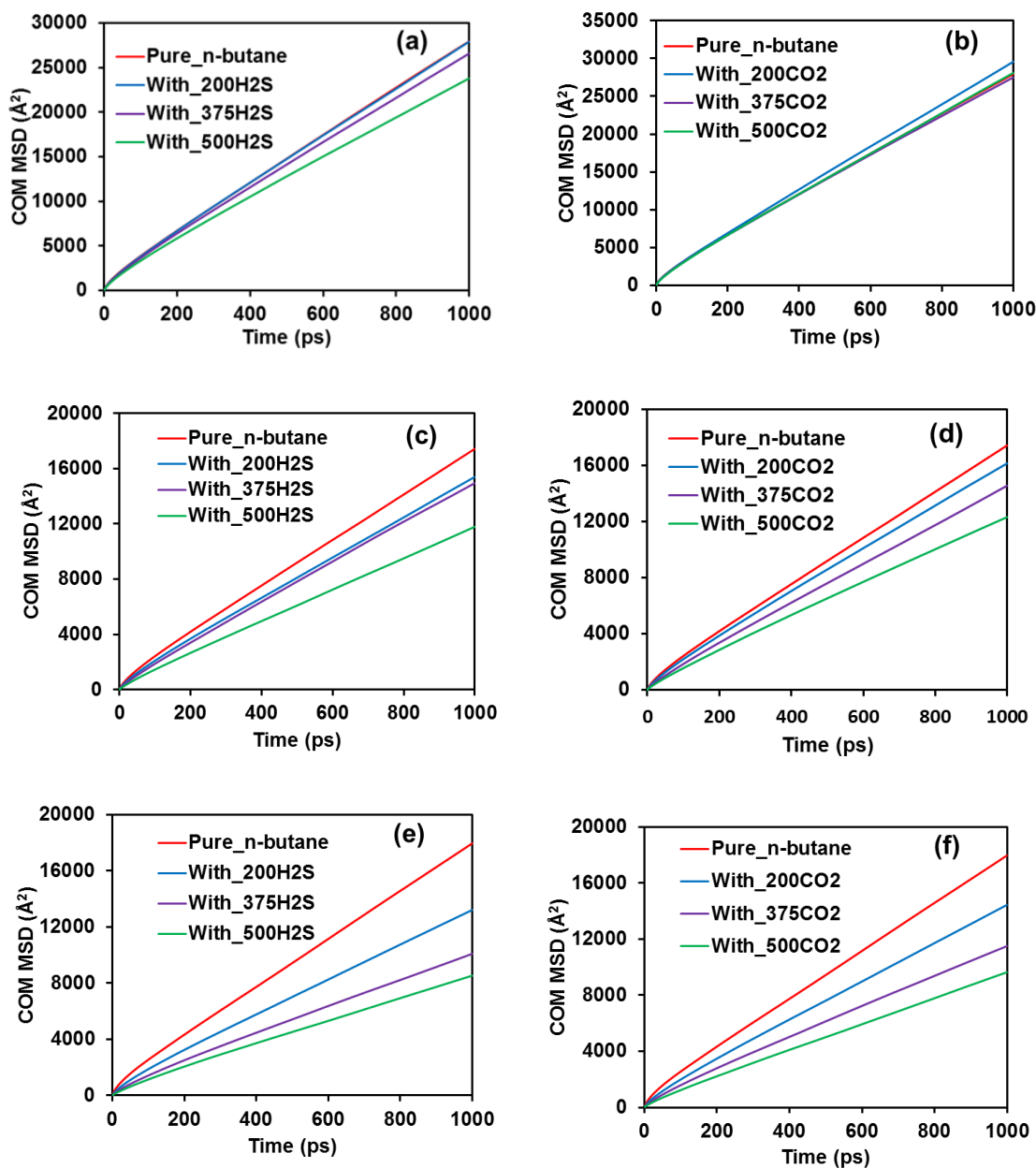


FIGURE 4.16: COM MSD for binary systems of *n*-butane and (a) H₂S in silica (b) CO₂ in silica (c) H₂S in muscovite (d) CO₂ in muscovite (e) H₂S in MgO (f) CO₂ in MgO pores

TABLE 4.8: Self-diffusion coefficient for *n*-butane, acid gases and N₂ in muscovite pores. The system composition is shown in Table 4.1

| System | D(<i>n</i> -butane) (10 ⁻⁸ m ² /s) | D(H ₂ S) (10 ⁻⁹ m ² /s) | D (CO ₂) (10 ⁻⁹ m ² /s) | D (N ₂) (10 ⁻⁹ m ² /s) |
|-----------------------|--|---|--|---|
| 1 | 3.7 ±0.1 | 3.7 ±0.1 | - | - |
| 2 | 3.5 ±0.3 | 3.1 ±0.1 | - | - |
| 3 | 2.9 ±0.2 | 1.9 ±0.1 | - | - |
| 4 | 3.8 ±0.3 | - | 4.8 ±0.1 | - |
| 5 | 3.5 ±0.2 | - | 3.4 ±0.1 | - |
| 6 | 2.9 ±0.1 | - | 2.5 ±0.1 | - |
| 7 | 0.9 ±0.2 | - | - | 5.3 ±0.3 |
| 8 | 0.9 ±0.1 | - | - | 2.6 ±0.2 |
| 9 | 0.7 ±0.1 | - | - | 1.0 ±0.2 |
| Pure <i>n</i> -butane | 4.1 ±0.2 | - | - | - |

TABLE 4.9: Self-diffusion coefficient for *n*-butane, acid gases and N₂ in MgO pores. The system composition is shown in Table 4.1

| System | D(<i>n</i> -butane) (10 ⁻⁸ m ² /s) | D(H ₂ S) (10 ⁻⁹ m ² /s) | D (CO ₂) (10 ⁻⁹ m ² /s) | D (N ₂) (10 ⁻⁹ m ² /s) |
|-----------------------|--|---|--|---|
| 1 | 3.1 ±0.2 | 11.4 ±0.2 | - | - |
| 2 | 2.3 ±0.1 | 5.9 ±0.1 | - | - |
| 3 | 2.0 ±0.2 | 3.7 ±0.1 | - | - |
| 4 | 3.4 ±0.3 | - | 11.3 ±0.1 | - |
| 5 | 2.7 ±0.1 | - | 5.9 ±0.1 | - |
| 6 | 2.3 ±0.2 | - | 3.7 ±0.1 | - |
| 7 | 3.3 ±0.2 | - | - | 16.5 ±0.4 |
| 8 | 2.1 ±0.2 | - | - | 8.1 ±0.3 |
| 9 | 2.4 ±0.1 | - | - | 3.1 ±0.2 |
| Pure <i>n</i> -butane | 4.2 ±0.3 | - | - | - |

this substrate. In muscovite pores, CO₂ travels faster than H₂S while both CO₂ and H₂S has similar diffusion coefficient in MgO pores. These results are consistent with interaction energy results presented in **Figure 4.12**. Results in Tables 4.7 – 4.9 also show that N₂ travels faster than H₂S and CO₂ especially at low N₂ loading, perhaps due to smaller size of N₂ molecule and also reflecting the weak adsorption of N₂ on the pore surfaces in the systems considered here.

Some prior studies reported an enhancement of the mobility of hydrocarbons within model pores upon low CO₂ loading.[32, 115, 135] This was not observed in

the present simulations, because the systems considered here are very dense, and pore crowding is expected to inhibit diffusion. In fact, prior studies have reported a decrease in hydrocarbon mobility at higher CO₂ loadings.[\[135\]](#)

4.5 Conclusions

Equilibrium MD simulations were performed to investigate the energetics, structure and transport properties of *n*-butane confined within slit-shaped nano-pores of width 2.2nm carved out of silica, muscovite and MgO surfaces in the presence of CO₂, H₂S, N₂ and their mixtures at 350K. The study was performed to compare the performance of H₂S with that of CO₂, the effect of the presence of an inert gas (N₂), and the effect of pore-surface chemistry on the behaviour of the confined hydrocarbon. Because all the pores considered are dry, pH effects on the pore surfaces were not investigated. The results show that CO₂ is more efficient than H₂S in displacing *n*-butane from silica pore surface, while H₂S performs better than CO₂ in muscovite pores. The two acid gases show similar performance in MgO. Analysis of the fluid-substrate interaction energy reveals that the results strongly correlate with the attraction between each acid gas and the pore surfaces. While H₂S is more strongly attracted to muscovite surface compared to CO₂, it is more weakly adsorbed on silica. Both gases show similar interaction with MgO. The results also show that mixtures of CO₂ and H₂S do not yield synergetic effects in displacing *n*-butane. The orientation and planar distribution of the adsorbed acid gases on the three solid surfaces further reinforce the observation that the nature of the pore surface dictates the structure of the adsorbed fluids, thus affecting how the acid gases control the structure of confined hydrocarbons. In most cases considered, it was observed that the self-diffusion coefficient of *n*-butane decreases when the gases are added probably due to pore-crowding effect. The results could

contribute to the design of enhanced oil recovery strategies for improvement in hydrocarbon production and in acid gas sequestration. Future investigations should address the effect of water and the presence of ions on the results presented.

4.6 Acknowledgements

Generous allocations of computing time were provided by the National Energy Research Scientific Computing Center (NERSC) at Lawrence Berkeley National Laboratory. NERSC is supported by the DOE Office of Science. S.B.B. acknowledges financial support from the Petroleum Technology Development Fund (PTDF). This research received funding from the European Unions Horizon 2020 research and innovation program under Grant No. 764810. D.R.C. was supported by the U. S. Department of Energy, Office of Basic Energy Sciences, Division of Chemical Sciences, Geosciences and Biosciences under grant DE-SC0006878. We are grateful to Adrian Gregory for insightful discussions.

Chapter 5

Competitive Adsorption and Mobility:

N-Octane, CO₂ and H₂S in Alumina and

Graphite Pores

The material presented in this Chapter is in preparation for submission to The Journal of Molecular Physics.

5.1 Abstract

Because gas injection into geological formations is often practiced to achieve enhanced oil recovery (EOR), it is important to understand at the molecular level the relations between competitive adsorption and fluid mobility at the single-pore level. To achieve such an understanding, here, molecular dynamics simulation results are reported to document structural and dynamical properties of *n*-octane, CO₂ and H₂S confined in slit-shaped alumina and graphite pores. The substrates

are chosen as proxy models for inorganic and carbon substrates. It was found that CO₂ and H₂S could displace *n*-octane from alumina surface but not from graphite surface. Analysis of the results shows that the stronger attractions between *n*-octane and graphite than CO₂/H₂S and graphite are responsible for this observation, with the opposite observed in alumina pores. In all pores, the results suggest that, limited to the conditions chosen for this study, adding CO₂ or H₂S enhances the diffusion of *n*-octane. The mechanisms responsible for this observation are however different, as preferential adsorption sites are evident on the alumina surface for both CO₂ and H₂S, but not on graphite. The results could contribute to the design of advanced EOR technologies through the proposed possible molecular mechanisms.

5.2 Introduction

The quest for sustainable and environmental-friendly energy sources coupled with depletion of global oil reserves has stimulated research into shale gas production. Shale rocks consist mainly of clay, quartz, pyrites, carbonates (inorganic) and kerogen (organic) with many pores in nanometer size range.[4, 136, 137] Pores found in shale have poor connectivity resulting in low permeability. To overcome the challenge of low permeability of shale, hydrocarbon production from shale plays is achieved via horizontal drilling and hydraulic fracturing, although most of the hydrocarbons remain in place and production rate drops rapidly.[112] Enhanced oil recovery (EOR) has been proposed for increasing hydrocarbon production from shale formations, and it is also widely practiced in conventional formations across

the world. The use of supercritical CO₂ in EOR could help to achieve CO₂ sequestration in geological formations while contributing to hydrocarbon production. In **Chapter 4**, Molecular Dynamics (MD) simulation was employed to study whether CO₂ and/or H₂S could displace *n*-butane from silica, muscovite and MgO surfaces. It was found that both gases perform reasonably well in silica and muscovite, but poorly in model MgO substrate. The study showed that the results depend on competitive adsorption among the confined fluids (hydrocarbon and acid gases) on the substrate. To complement the results presented in **Chapter 4**, where only inorganic substrates were considered, in this Chapter, the ability of CO₂ and H₂S to displace *n*-octane from surfaces of different chemistry is investigated. Because hydrocarbons are more strongly attracted to carbon-based substrates, CO₂ and H₂S might not be as effective in carbon pores as they are in inorganic ones. To test this hypothesis, graphite was chosen as a simple model for carbon pore, and alumina for inorganic pores. It should be noted that graphite has been extensively used to model the organic matter present in shale.[138–143]

Several studies have been conducted for CO₂–hydrocarbon systems confined in inorganic[32, 36, 38, 39, 45, 113–115] and carbon nanopores.[37, 138, 143–146] Yuan et al.[144] performed MD simulations to study methane (CH₄) and CO₂ confined in carbon nanopores and found that CO₂ is more strongly adsorbed on graphite than CH₄, resulting in CO₂ displacing CH₄ from graphite surface. They found an optimal pore diameter for CH₄ recovery. Liu et al.[138] studied binary systems of CH₄ and CO₂ in graphite nanochannel and found that CO₂ shows preferential adsorption on graphite surface and has longer residence times close to

the surface. Wu et al.[143] found that both CO₂ and N₂ could displace adsorbed CH₄ from the surface of carbon nanochannel. They reported that while CO₂ replaced the adsorbed CH₄, N₂ enhanced CH₄ displacement by lowering its partial pressure. Sun et al.[45] studied CH₄ and CO₂ confined in silica, calcite and graphite nanopores and found that CH₄ is more strongly adsorbed on graphite compared to silica and calcite, and that CO₂ is more strongly attracted to calcite than silica and graphite. Although most studies focussed on CH₄, a few considered longer alkane molecules on graphite.[147–149] To complement those studies as well as the results reported in **Chapter 4** on confined *n*-butane and acid gases, *n*-octane, CO₂ and H₂S are simulated.

In this chapter, the displacement of *n*-octane from alumina and graphite surfaces due to CO₂ and H₂S is investigated, including the structural and dynamical properties of the confined fluids. The pores simulated do not contain water and therefore, pH effect on the pore surfaces are not considered. The remaining sections of this Chapter are organized as thus: Simulation models and algorithms are explained in the next section. Then, the results are presented followed by summary of main findings.

5.3 Simulation Methods and Algorithms

5.3.1 Simulation set up

Equilibrium molecular dynamics (MD) simulations were conducted for binary mixtures of CO_2 - n - C_8H_{18} and H_2S - n - C_8H_{18} confined within slit-shaped alumina and graphitic pores of width 2.2nm at 350 K. The pore width is chosen as it has been documented that pores found in shale are in the range of 1.7 – 20nm.[150] The simulations were conducted to investigate the effect of the addition of CO_2 or H_2S on the behaviour of the confined n -octane. In **Chapter 4**, MD simulations were conducted to investigate the displacement of n -butane from silica, muscovite and MgO surfaces by addition of CO_2 or H_2S . All surfaces considered in **Chapter 4** were inorganic, where it found that the effectiveness of the gas at displacing n -butane from the surfaces depends on gas–surface interactions. In this Chapter, an inorganic pore (alumina) and a carbon–based pore (graphite) are considered. It is of interest to understand the interaction of the gases with the surfaces and the implication on the behaviour of the confined n -octane. Alumina is chosen as a representative inorganic component of shale and graphite as a simple model for carbon–based pores. Alumina slabs are modelled as crystallographic faces of sapphire α - Al_2O_3 with space group R3c and C plane (0001). Two alumina slabs facing each other within the simulation box form the slit shaped pore. The pore width is the centre-to-centre distance between the hydroxyl groups on the two alumina slabs across the pore volume. All the non-bridging oxygen atoms were protonated yielding a realistic model for alumina surface.[151] Slit-shaped alumina pores have

been used in several studies.[102, 152–154] Graphite pores were obtained from two 4-layered graphite slabs with interlayer spacing of 0.34nm facing each other, with slab-to-slab separation equal to the pore width of 2.2nm. The pore width of the graphitic pore is defined as the distance between the planes passing through the outermost graphene layers of the two slabs. The planar dimensions of each alumina and graphite slab are 47.6 x 90.68 Å² and 48.92 x 90.86 Å² respectively yielding alumina and graphite pores of approximately equal pore volume. Each slab of the substrate is parallel to the X-Y plane of the simulation box. The Z-dimension of the simulation box was set to 45.82 and 42.05 Å for alumina and graphite respectively. All atoms of the solid substrates were fixed except the OH groups on alumina, which were allowed to vibrate. Due to the application of periodic boundary conditions, the systems are infinitely long in X and Y directions and the pore width is defined along Z direction.

Binary systems of *n*-C₈H₁₈ – CO₂ and *n*-C₈H₁₈ – H₂S were simulated at different gas loadings and constant number of *n*-C₈H₁₈ molecules. The composition and system pressure obtained from average pore density of *n*-octane and gas at the middle of the pores using Peng-Robinson equation of state implemented in REFPROP software version 9.1 are reported in Table 5.1. Figure 5.1 shows representative snapshots for *n*-octane – H₂S and *n*-octane – CO₂ systems for maximum gas loading in alumina and graphite pores.

TABLE 5.1: Estimated pressure and composition of all simulated systems in this work. In all cases, the simulation temperature was 350K (a = alumina and b = graphite)

| System | No of <i>n</i> -octane | No of CO ₂ | No of H ₂ S | P (MPa) ^a | P (MPa) ^g |
|--------|------------------------|-----------------------|------------------------|----------------------|----------------------|
| 1 | 200 | 200 | - | 6.0 | 7.5 |
| 2 | 200 | 350 | - | 39.2 | 17.5 |
| 3 | 200 | 500 | - | 177.3 | 73.6 |
| 4 | 200 | - | 200 | 1.9 | 3.0 |
| 5 | 200 | - | 350 | 28.3 | 5.8 |
| 6 | 200 | - | 500 | 120.0 | 60.1 |
| 7 | 200 | - | - | 0.02 | 0.02 |

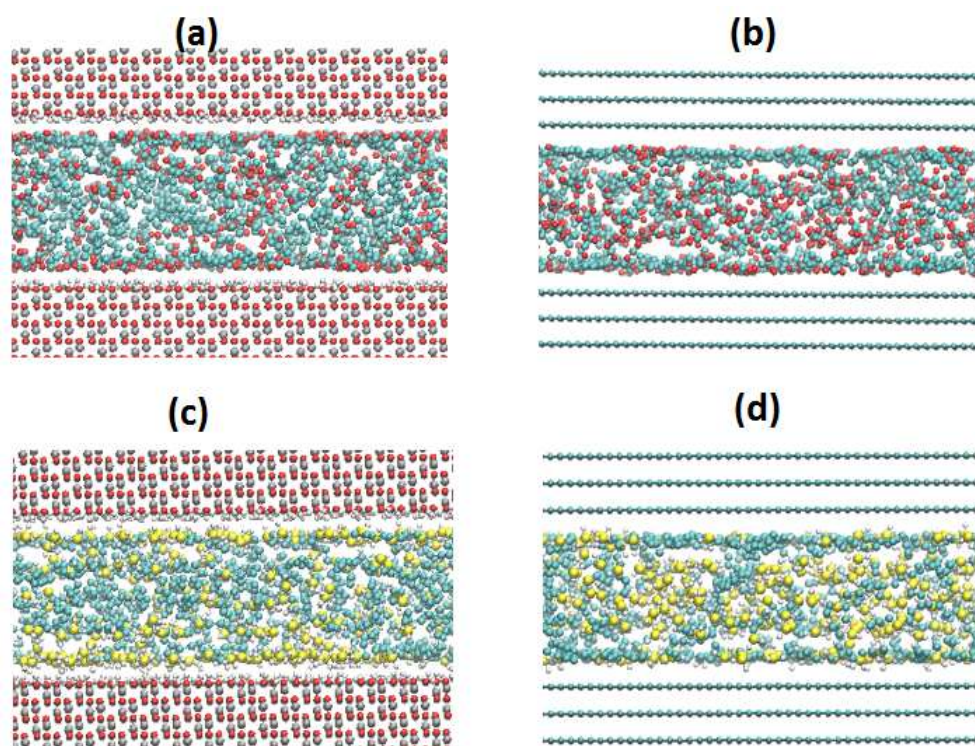


FIGURE 5.1: Simulation snapshots for *n*-octane - CO₂ systems in (a) alumina (b) graphite. Snapshots for *n*-octane-H₂S systems in (c) alumina (d) graphite. All systems shown contain 200 *n*-octane and 500 gas molecules. Cyan spheres are -CH₃ and -CH₂ in *n*-octane, yellow are sulphur, white are hydrogen, red are oxygen and grey are aluminium. For clarity, only a portion of the solid substrates are shown. Please refer to Section 5.3.1 for the simulation boxes.

5.3.2 Force fields

Alumina and graphite were modelled with the CLAYFF[48] force field and the model developed by Steele[155] respectively. *N*-octane was modelled using TRAPPE-UA force field,[49] CO₂ with the EPM2 force field[50], and H₂S with the model of Kamath and Potoff.[51] *n*-octane is flexible, and is described by angle bending and dihedrals. -CH₃ and -CH₂ groups in *n*-octane were described using the united atom formalism. Non-bonded interactions were modelled by electrostatic and dispersive interactions. The dispersive interactions were described by 12-6 Lennard Jones potential and the electrostatic interactions were modelled by Coulombic potential. There is no electrostatic interactions between CO₂ or H₂S molecules and graphite surface as graphite contains no charge. Lorentz-Berthelot combination rules[47] were used to obtain LJ parameters for unlike atoms. The cut-off distance for all interactions was set to 14Å. The particle mesh Ewald method was used for long range corrections to electrostatic interactions.[75]

5.3.3 Algorithms

All simulations were performed using the simulation package GROMACS version 5.0.4, [76, 77] in the canonical ensemble (NVT) at 350K. The temperature of the systems was controlled using the Nosé – Hoover thermostat [57, 58] with a relaxation time of 200fs. The temperature of the solid substrate and that of the fluid molecules were controlled separately using two thermostats. The total simulation time for each system was 60ns. Each system was considered equilibrated when

densities of fluid molecules fluctuates around a constant value, and the system energy fluctuates within 10% of the average value. The last 10ns was used for data analysis.

5.4 Results and Discussion

5.4.1 Density Profiles

The density profiles of confined fluid molecules in the direction normal to the pore surfaces is used to quantify the distribution of fluid molecules within the pores. The density profiles of the centre of mass (COM) of *n*-octane at different H₂S and CO₂ loadings in alumina and graphite pores are shown in Figure 5.2. The result reveals preferential adsorption of *n*-octane on the pore surfaces, especially when neither CO₂ nor H₂S is present as shown by high peak positions close to the pore walls compared to the middle of the pore. The adsorption of *n*-octane onto graphite is stronger than on alumina pore as evidenced by the density of the first adsorption layer in Figure 5.2. This result is consistent with the report of Wang et al.[37] who observed higher peak density for *n*-octane confined in graphite than in silica pore and signifies strong interaction and preferential adsorption of *n*-octane within carbon nanopores. The results in Figure 5.2 show that addition of H₂S or CO₂ to a system containing pure *n*-octane results in the displacement of *n*-octane from alumina surface as revealed by the decrease in the first peak height in the density profiles. In graphite however, the reduction in the peak height only occurs when 200 gas molecules were added and remains relatively unchanged with

further increase in gas loading. This suggests that CO_2 and H_2S are not effective at displacing *n*-octane from graphite. The behaviour of *n*-octane in graphite pore just described is in contrast with the results obtained for *n*-butane in silica, muscovite pore and MgO pores reported in **Chapter 4** where the addition of the CO_2 or H_2S resulted in the continuous reduction in the density of *n*-butane molecules in the first adsorbed layer for the loadings considered, indicating continuous displacement of *n*-butane from the surfaces.

The density profiles of sulphur (S) of H_2S and carbon (C) of CO_2 in alumina and graphite pores are shown in Figure 5.3. The density profiles of hydrogen (H) of

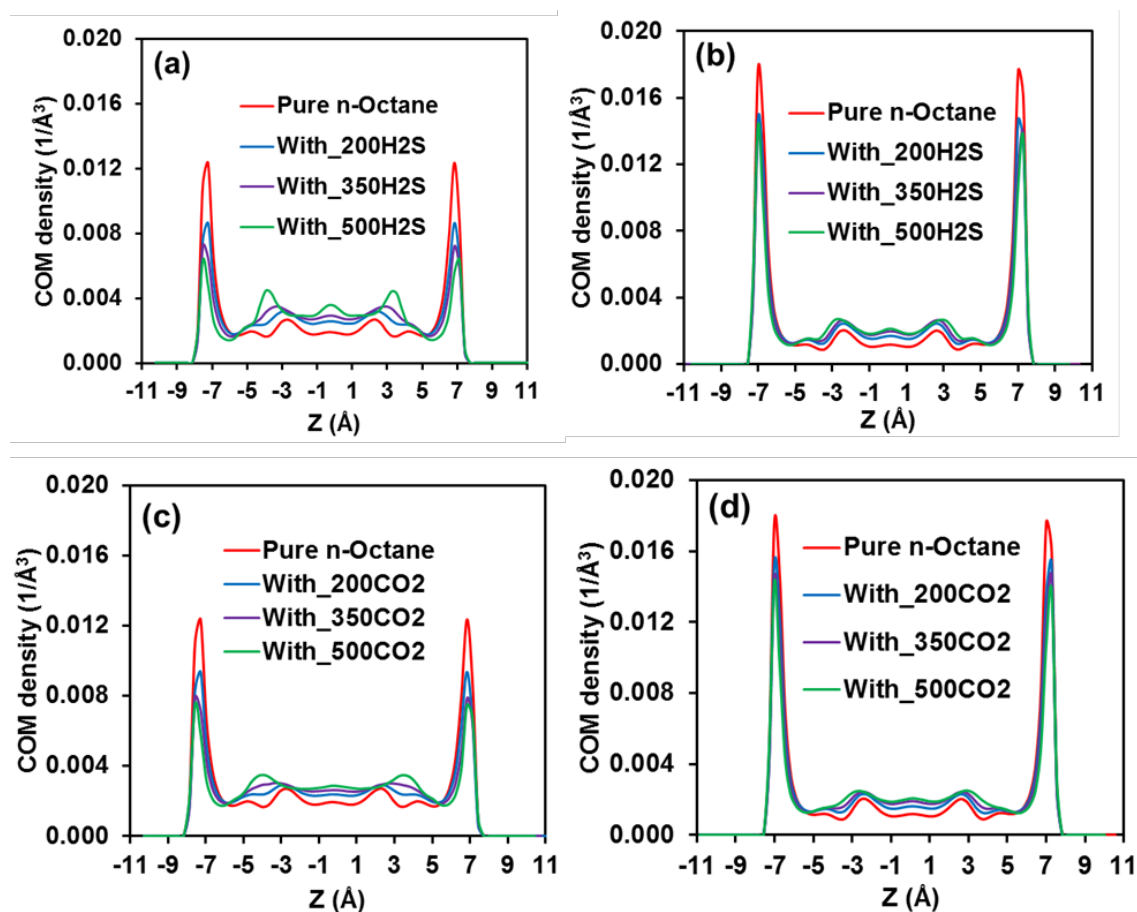


FIGURE 5.2: Density profiles of *n*-octane in (a) alumina (b) graphite at different H_2S loadings and density profiles of COM of *n*-octane at different CO_2 loadings in (c) alumina and (d) graphite. All systems contain 200 molecules of *n*-octane

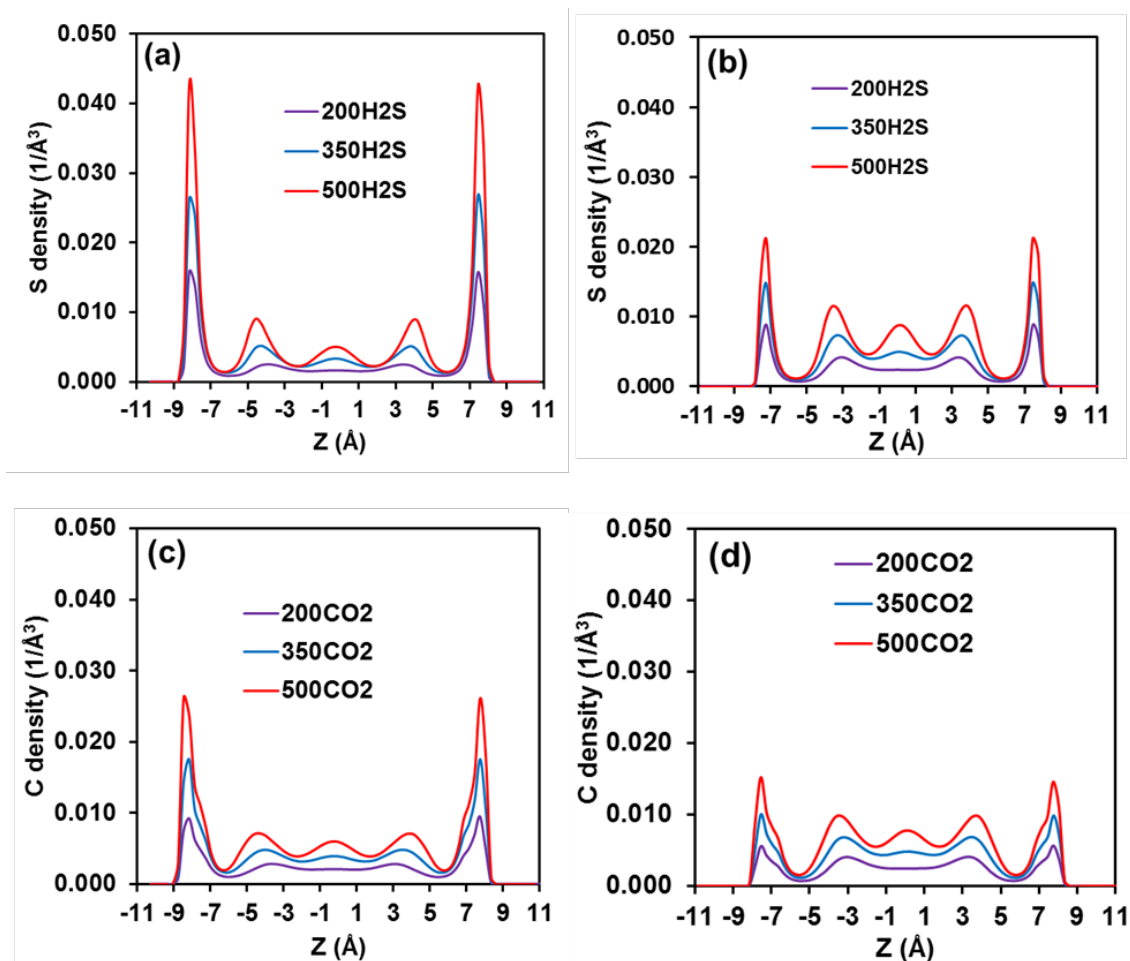


FIGURE 5.3: Density profiles of S of H₂S in (a) alumina (b) graphite and density profiles of C of CO₂ in (c) alumina (d) graphite at different acid gas loadings. All system contain 200 molecules of *n*-octane

H₂S and oxygen (O) of CO₂ are presented in **Figure 5.4**.

The results in **Figure 5.3** show that CO₂ and H₂S gases are more strongly adsorbed on alumina surface than graphite surface. This is due to electrostatic interactions between the pore surfaces and the gas molecules which are possible in alumina but not in graphite. The stronger attraction between the gases and alumina surface correlates with their ability to displace *n*-octane from alumina surface. Although it appears that more H₂S molecules are adsorbed in the first layer in graphite pores than CO₂ based on the peak feature in **Figure 5.3**, the number of H₂S and CO₂ at the same loading obtained from the integral of the first peak is similar.

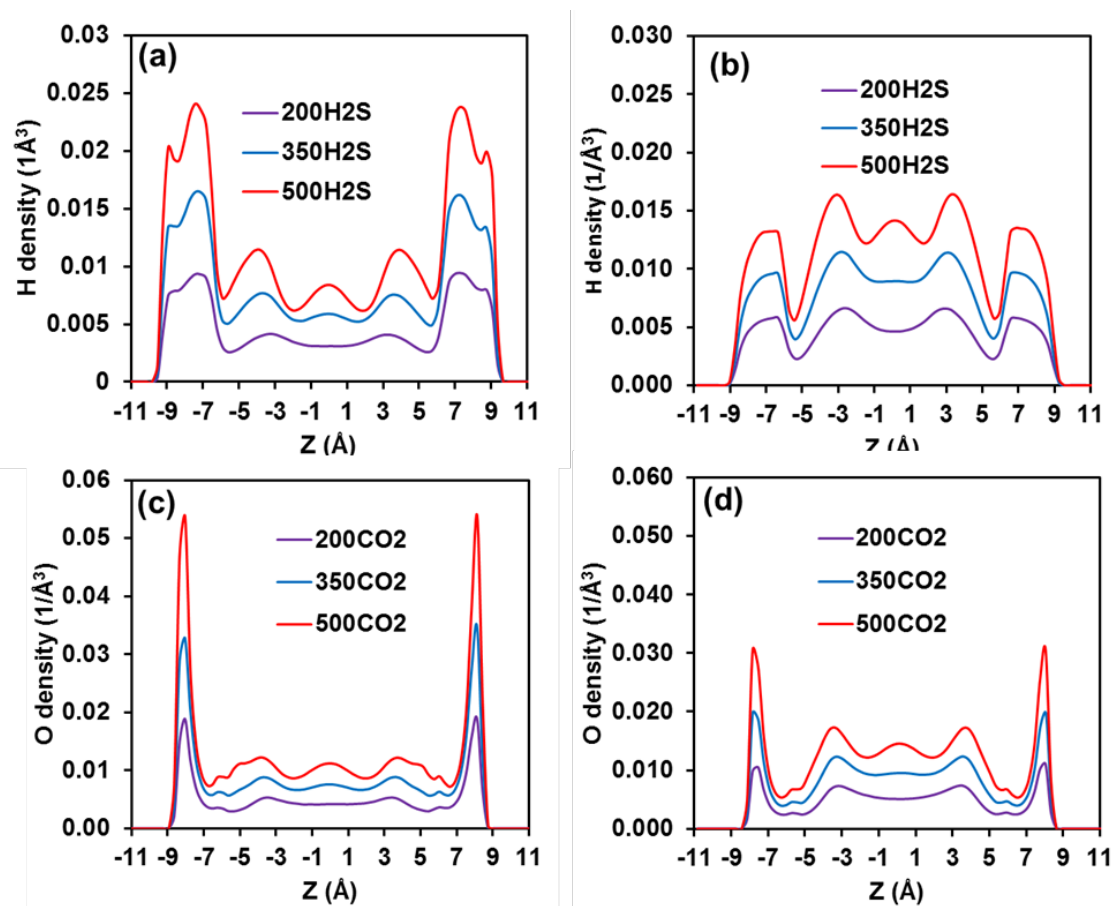


FIGURE 5.4: Density profiles of S of H_2S in (a) alumina (b) graphite and density profiles of C of CO_2 in (c) alumina (d) graphite at different acid gas loadings. All system contain 200 molecules of *n*-octane

5.4.2 Interaction Energy

To understand preferential adsorption of the confined fluid molecules the interaction energy of respective fluid molecules with alumina and graphite surfaces were calculated. Figure 5.5 shows *n*-octane–surface interaction energy in the binary systems of *n*-octane– H_2S and *n*-octane– CO_2 at different loadings. The results are normalised by the number of molecules in the system. As *n*-octane bears no charge, there is no electrostatic contribution to the interaction energy. The negative sign signifies attraction between *n*-octane and the pore surfaces. The results show that *n*-octane is more strongly attracted to graphite than alumina. The

results also indicate that *n*-octane interaction energies do not change significantly with gas loading especially at higher gas loading. The stronger interaction between *n*-octane and graphite surface correlates with the poor performance of the gases at displacing *n*-octane from graphite as shown in the density profiles in Figure 5.2 (b and d).

The gas–surface interaction energies are shown in Figure 5.6. The interaction energy is the sum of LJ and electrostatic contributions for calculations in alumina

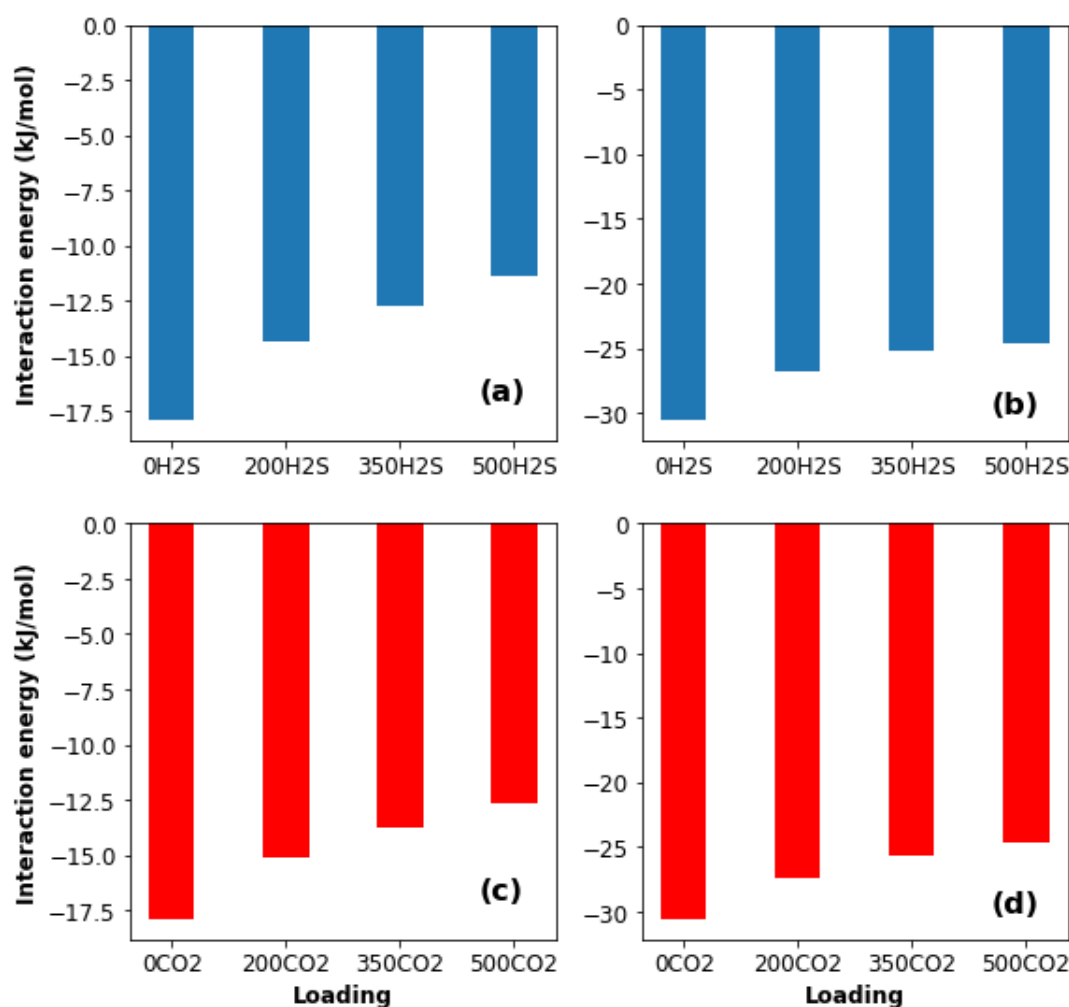


FIGURE 5.5: *n*-octane–surface interaction energy for binary systems of *n*-octane–H₂S in (a) alumina (b) graphite and for binary systems of *n*-octane–CO₂ in (c) alumina (d) graphite. All systems contain 200 *n*-octane molecules. The interaction energies are normalised by the number of *n*-octane in the system

pores. There is no electrostatic interactions between the gases and graphite pores as graphite bears no charge. The results show that the acid gases are more strongly attracted to alumina than graphite due to higher magnitude of interaction energy in alumina. The results also show that the interaction energies does not change significantly with acid gas loading especially in graphite pore. The stronger interaction of the acid gases with alumina pores than graphite pores is consistent with *n*-octane density profiles in Figure 5.2, where the gases show better performance at displacing *n*-octane from alumina surface than graphite surface.

5.4.3 Structure of adsorbed acid gas

5.4.3.1 In-plane density distribution

The results discussed previously in this chapter show that CO₂ and H₂S displaced *n*-octane from alumina surface but not from graphite surface. The difference in behaviour of the gases at the solid-fluid interface is attributed to different interactions of each gas with the respective solid substrates. As reported in **Chapter 4**, the in-plane density distribution of gas molecules adsorbed on a solid substrate reveals preferential adsorption sites on the substrate. Here, the in-plane density distribution of CO₂ and H₂S molecules adsorbed on the layer closest to alumina and graphite surfaces are reported. A layer of 2Å was selected for this calculation and the COM of each gas molecule was used to identify its position. As shown in Figure 5.7, the results of this calculation reveal preferential adsorption sites on alumina as high density regions correspond to location of these sites. On the other

hand, the distribution of the gases is random on graphite and suggests absence of sites where the gas molecules preferentially adsorb. The results just discussed corroborates the claim made in **Chapter 4** that the presence of adsorption sites where gas molecules could be preferentially adsorbed promotes the ability of the gas to displace hydrocarbon from the surface.

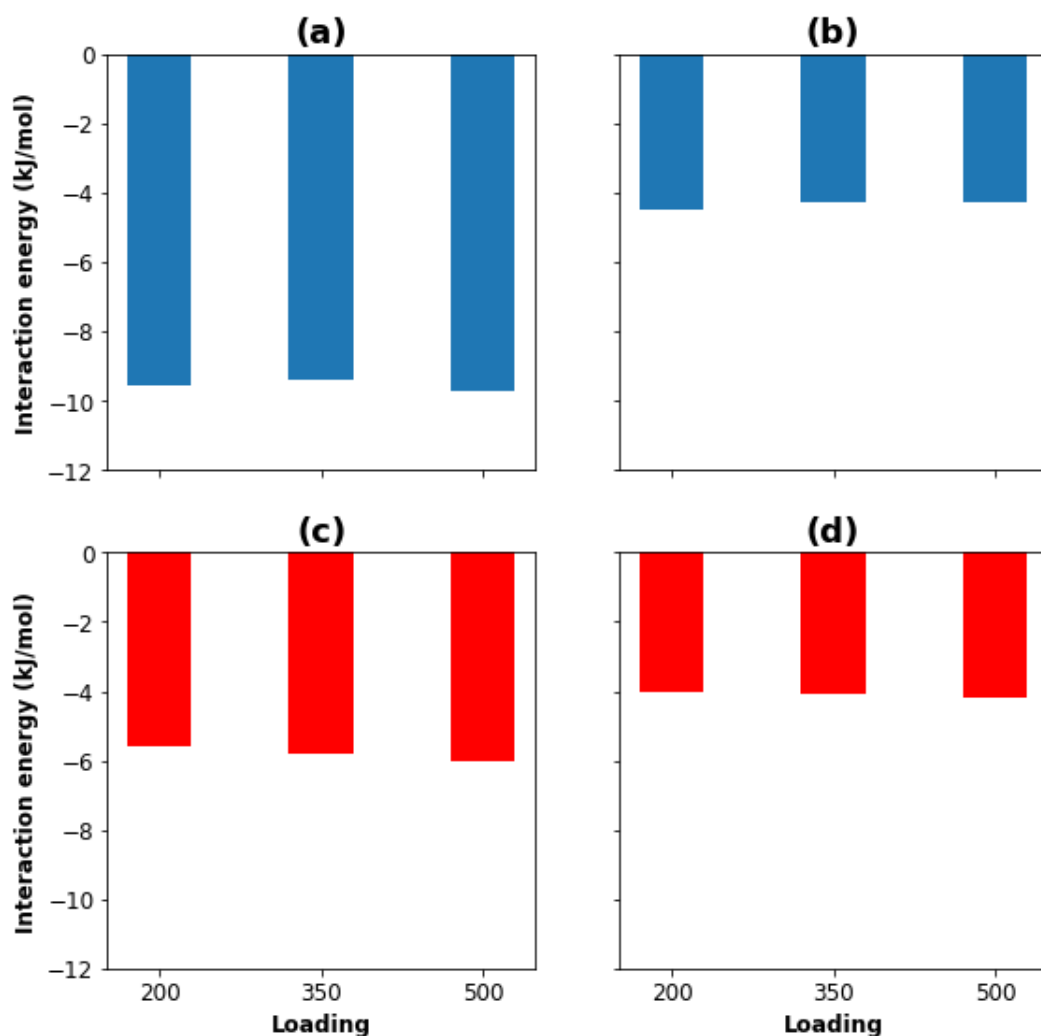


FIGURE 5.6: H₂S–surface interaction energy for binary systems of *n*-octane – H₂S in (a) alumina (b) graphite and CO₂–surface interaction energy for binary systems of *n*-octane – CO₂ in (c) alumina (d) graphite. All systems contain 200 *n*-octane molecules at 350K. The interaction energies are normalised by the number of H₂S or CO₂ in the system

5.4.3.2 Molecular Length and Orientation of *n*-octane

To quantify the structure of adsorbed *n*-octane and those at the middle of the pore, the probability distribution of the angle (θ_1) formed between the C1-C8 vector of *n*-octane and the normal to the surface, the angle (θ_2) formed between the orthogonal vector to the plane formed by C1-C8 vector and C1-C2 vector are calculated. When θ_1 is 90° and θ_2 is 0, all *n*-octane atoms are on the same plane and parallel to the surface; when θ_1 is 0 and θ_2 is 90° , the plane is orthogonal to the surface.

The change in the end-to-end distance of *n*-octane, L defined as equation 5.1 is also calculated to investigate the effect of *n*-octane–surface interactions on the

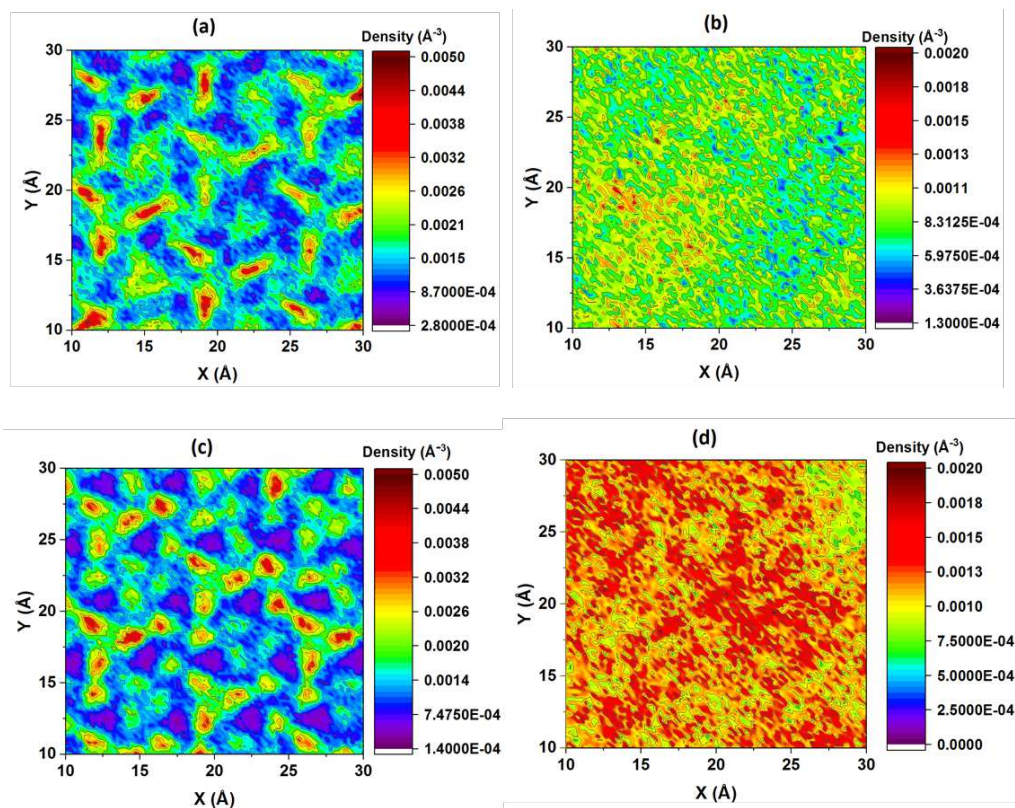


FIGURE 5.7: In-plane density distribution of COM of CO_2 in (a) alumina (b) graphite and same result for H_2S in (c) alumina (d) graphite. All systems contain 200 *n*-octane molecules and 500 molecules of the gas

structure of confined *n*-octane. In all cases, *n*-octane molecules found within 5Å in the first layer is considered for the calculation while the middle *n*-octane are those found within a layer of 8Å centred at the middle of the pore. L describes how the molecular length of *n*-octane changes during the simulation. The results are shown in Figure 5.8.

$$L = \frac{l - l_0}{l_0} \quad (5.1)$$

In Equation 5.1, l is the end-to-end distance of single *n*-octane molecule in the simulations and l_0 is the end-to-end distance in free state (8.81Å). The free state of *n*-octane refers to when it is a straight chain. The results in Figure 5.8, panel (a and b) show that *n*-octane molecules in the layer close the pore surfaces lay parallel to the surface and it appears that the molecules are more parallel to graphite surface than alumina surface. This has been previously observed for *n*-octane confined in silica pore.[142] At the middle of the pore, *n*-octane still prefers to lay parallel to the surface, although the carbon atoms are more out-of-plane and there is wider distribution of the angles. This is probably due to small size of the pores and *n*-octane being a relatively long molecule when compared to the size of the pores. The distribution of the angles is similar at the middle of graphite and alumina pores which suggests that the pore chemistry has little or no effect on the structure of *n*-octane at the middle of the pores. The distribution of L presented in Figure 5.8, panel (c and d) shows that *n*-octane molecules in the first layer are more folded on graphite than on alumina surface. There is no difference in the folding degree for *n*-octane molecules at the middle of graphite and alumina

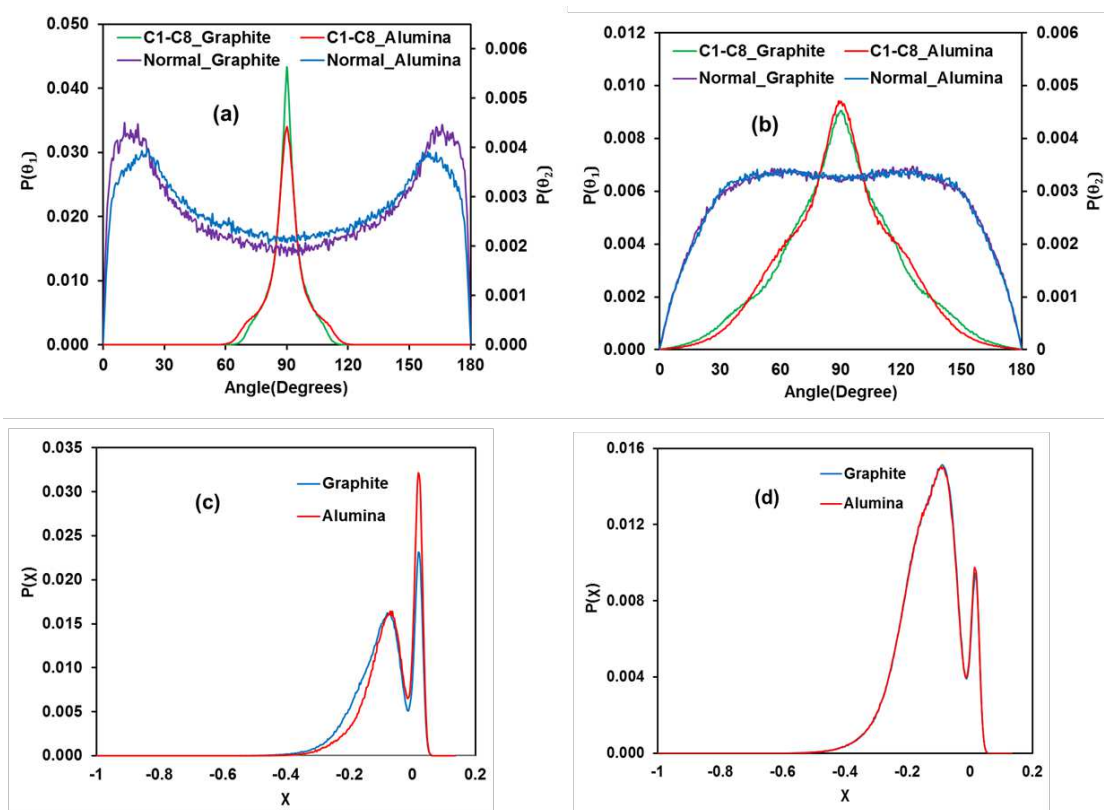


FIGURE 5.8: Probability distribution of angle between C1-C8 vector and normal to the surface and the angle between the orthogonal vector to the plane of C1-C8 vector and C1-C2 vector and the normal to the surface for *n*-octane occupying (a) first layer (b) middle region. Probability distribution of χ for *n*-octane occupying (c) first layer (d) middle region. The results are shown for *n*-octane-H₂S in graphite and alumina pores for 500H₂S loading

pores. The results also show that *n*-octane molecules at the middle of the pore are more folded than those adsorbed close to the pore walls. The results just discussed suggests that the chemistry of both substrates influences the structure of *n*-octane differently only in the layer closest to the surface and this difference vanishes close to the middle of the pore.

5.4.4 Diffusion coefficient of confined fluids

The self-diffusion coefficients of confined fluid molecules were calculated from COM mean square displacement (MSD) of *n*-octane, CO₂ and H₂S following established

TABLE 5.2: Self-diffusion coefficient for *n*-octane, CO₂ and H₂S in graphite pores. The system composition is shown in Table 4.1

| System | D(<i>n</i> -octane) (10 ⁻⁸ m ² /s) | D (CO ₂) (10 ⁻⁸ m ² /s) | D(H ₂ S) (10 ⁻⁸ m ² /s) |
|-----------------------|--|--|---|
| 1 | 1.3 ±0.2 | 3.5 ±0.1 | - |
| 2 | 1.1 ±0.1 | 2.4 ±0.1 | - |
| 3 | 0.7 ±0.1 | 1.3 ±0.1 | - |
| 4 | 2.1 ±0.2 | - | 3.4 ±0.1 |
| 5 | 2.1 ±0.1 | - | 2.5 ±0.1 |
| 6 | 0.9 ±0.1 | - | 1.3 ±0.1 |
| Pure <i>n</i> -octane | 3.9 ±0.2 | - | - |

procedures.[59] As previously mentioned in **Chapter 4**, the diffusion coefficient results depend on the system size but it is not checked in this study. The results obtained for fluids confined in graphite and alumina pores are shown in Table 5.2 and 5.3 respectively. The results show that diffusion coefficient of *n*-octane is higher when CO₂/H₂S is present in both graphite and alumina pores than in pure *n*-octane systems. This suggests that CO₂/H₂S enhances the diffusion of *n*-octane at the condition of our simulations. The results also show that within graphite, *n*-octane diffusivity enhancement is larger for *n*-octane–CO₂ systems than *n*-octane–H₂S systems. In alumina, *n*-octane diffusion coefficient seems to be higher for *n*-octane–H₂S systems than *n*-octane–CO₂ systems especially at higher gas loadings. On the other hand, the diffusion coefficients of CO₂ and H₂S are similar in both graphite and alumina for the same gas loading. The results in Table 5.2 and 5.3 show that *n*-octane diffusion coefficients are about 3 orders of magnitude higher than those of CO₂ and H₂S in both graphite and alumina pores.

TABLE 5.3: Self-diffusion coefficient for *n*-octane, CO₂ and H₂S in alumina pores. The system composition is shown in Table 4.1

| System | D(<i>n</i> -octane) (10 ⁻⁹ m ² /s) | D (CO ₂) (10 ⁻⁸ m ² /s) | D(H ₂ S) (10 ⁻⁸ m ² /s) |
|-----------------------|--|--|---|
| 1 | 7.9 ±0.2 | 1.4 ±0.2 | - |
| 2 | 4.6 ±0.2 | 0.9 ±0.1 | - |
| 3 | 2.8 ±0.1 | 0.5 ±0.1 | - |
| 4 | 8.8 ±0.2 | - | 1.5 ±0.1 |
| 5 | 5.0 ±0.1 | - | 1.0 ±0.1 |
| 6 | 2.7 ±0.1 | - | 0.5 ±0.1 |
| Pure <i>n</i> -octane | 15.9 ±0.2 | - | - |

5.5 Conclusions

Equilibrium MD simulations were conducted to study energetics, structure and transport properties of *n*-octane confined within slit-shaped alumina and graphite nano-pores of width 2.2 nm in the presence of CO₂ and H₂S of different loadings at 350K. The study compares the effect of the presence of H₂S vs. that of CO₂, effect of pore-surface chemistry on the behaviour of confined *n*-octane. The effect of pH on the systems are not considered because the pores are dry. Our results revealed that H₂S and CO₂ are more efficient at displacing *n*-octane from alumina pore surfaces than graphite pore surface because *n*-octane–surface interactions are much stronger in graphite than in alumina pores and the gas–surface interactions are much more attractive in alumina than in graphite pores. Analysis of in-plane distribution of gas molecules at the solid–gas interface reveals presence of adsorption sites on alumina but not on graphite and facilitates stronger interaction of gas molecules with alumina pores which correlates with their ability to displace *n*-octane from alumina surface. The structure of *n*-octane adsorbed at the solid–fluid interface is more perturbed compared to in the middle of the pores due to the

difference in the extent of stretching for *n*-octane present in the various regions. At the condition of our simulations, addition of CO₂ or H₂S enhances the mobility of *n*-octane as revealed by increases diffusion coefficients with gas loading. Our results could contribute to the design of enhanced oil recovery and gas sequestration technologies.

Chapter 6

Summary and Outlook

The study of confined fluid behaviour is crucial to better understand adsorption and interfacial phenomena and their effects on properties of fluids such as solubility, transport and structure. Gaining atomic level information about the behaviour of fluid molecules at different conditions could help in the design of new technologies and improvement of existing ones. This thesis provides molecular level insights into structural and dynamical properties of selected fluid molecules such as water, H₂S, CO₂, N₂, *n*-butane and *n*-octane. Silica, muscovite, magnesium oxide, alumina and graphite are solid substrates used throughout this thesis. Equilibrium molecular dynamics (EMD) simulations were performed using GROMACS and in some cases, it was integrated with PLUMED.

In **Chapter 3**, EMD simulations were employed to investigate effects of confinement on the solubility, structural and dynamical properties of aqueous H₂S in silica pores. Lower solubility of H₂S in confined water compared to the bulk was observed. Analysis of the hydration shell of H₂S revealed that the lower solubility of

H₂S under confinement is due to strong perturbation of water coordination in the first hydration shell of H₂S. This perturbation reduces as pore size increases resulting in increase in H₂S solubility with pore size. The in-plane density distribution and the probability distribution of angles of fluid molecules in the first hydration layer close to the pore walls revealed that confinement perturbs the structural and dynamical properties of water and H₂S. Comparison of the diffusivity and permeability of H₂S through hydrated silica pore with that of CH₄ revealed that H₂S permeates hydrated silica pore faster than CH₄.

Chapter 4 investigates the effect of CO₂, H₂S and N₂ injection on *n*-butane displacement from silica, muscovite and MgO surfaces. This chapter contributes to Enhanced Oil Recovery (EOR). The results show that CO₂ and H₂S can effectively displace *n*-butane from the pore surfaces as the amount of *n*-butane adsorbed in the first layer close to the pore walls decreases with gas loading. However, N₂ could not displace *n*-butane from all surfaces considered. Analysis of the gas – surface interaction energies shows correlation of the performance of the gas with the interaction energy which consequently revealed the dependence of the performance of the gas on the chemistry of the confining substrate. While CO₂ is more effective at displacing *n*-butane from silica surface than H₂S, it is less effective in muscovite and both gases show similar performance in MgO. The interaction of the gases with the surface influences the orientation of gas molecules in the first adsorbed layer (FAL) close to the pore walls. Analysis of the distribution of angles formed by gas molecules in FAL shows that the assembly of the gas at the fluid-wall interface could influence the performance of the gas. For example, H₂S

is in one-hydrogen down configuration in silica and it is less effective compared to CO₂, but in two-hydrogen down configuration in muscovite and it is more effective than CO₂.

The results presented in **Chapter 5** complement those in **Chapter 4** as it was found that the efficacy of a gas for EOR applications depends on the fluid–surface interactions. Consequently, simulations were conducted in which CO₂ and H₂S were added to alumina and graphite pores to compare the ability of the gases at displacing *n*-octane from the surfaces, and it was found that the gas could displace *n*-octane from inorganic surface (alumina) and not from the organic one (graphite). The enhancement of *n*-octane mobility was also observed.

The results presented in **Chapter 4** and **Chapter 5** were obtained in dry pores in the absence of water. Future investigations should consider the effect of water and the presence of ions on the results presented in these chapters. Since the focus of these Chapters was on the fluid-wall interface, future study should also consider the effect of the gas molecules coexisting with hydrocarbon at the middle of the pore to better understand the mechanism of enhanced diffusion reported in **Chapter 5**. Pores larger than 2.2nm could be used for this study with simulations performed at lower densities to eliminate crowding effect.

As a concluding remark, the results presented in this thesis were obtained from MD simulations at atomistic scale and give insightful observations about fluid behaviour in nanopores. Experimental studies should be performed at conditions of the simulations (moderate temperatures and pressures) to validate the results before field applications. To validate results presented in Chapter 3, *microvolumetry*

or ^1H NMR experiments could be performed to study oversolubility or undersolubility of gases in confined liquids. For more information about the experimental set up, please refer to these references.[\[18, 19\]](#) For results reported in Chapter 4 and 5, *core flooding* can be performed. This experimental approach is usually employed to study CO_2 -based EOR. The experiment provides information about the mechanism of CO_2 -rock interactions, distribution of CO_2 and long-term immobilization of injected CO_2 . For details about the experimental set up, please refer to this reference [\[44\]](#)

Appendix A

Methodology

Force field parameters

TABLE A.1: Intramolecular interaction parameters (Bond)

| Species | i | j | $K_{ij}(\text{kJ/mol})$ | $r^0(\text{nm})$ |
|-------------------|--------|--------|-------------------------|------------------|
| Silica | nO | H | 463700 | 0.1 |
| Butane | CH_3 | CH_2 | - | 0.154 |
| | CH_2 | CH_2 | - | 0.154 |
| Carbon Dioxide | C | O | - | 0.116 |
| Water | Ow | Hw | - | 0.1 |
| Hydrogen Sulphide | S | H | - | 0.134 |

TABLE A.2: Intramolecular interaction parameters (Angle)

| Species | i | j | k | $K_{ijk}(\text{kJ/mol})$ | $\theta^0(\text{degrees})$ |
|-------------------|--------|--------|-------------|--------------------------|----------------------------|
| Silica | Si | nO | H | 251.04 | 109.5 |
| Butane | CH_3 | CH_2 | CH_2/CH_3 | 519.6417 | 114 |
| | CH_2 | CH_2 | CH_2 | 519.6417 | 114 |
| Carbon Dioxide | O | C | O | - | 180 |
| Water | Hw | Ow | Hw | - | 109.47 |
| Hydrogen Sulphide | H | S | H | 272.548 | 92.5 |

TABLE A.3: Intermolecular interaction parameters

| Molecule | Atom | Symbol | $\epsilon(kJ/mol)$ | $\sigma(nm)$ | q (e) |
|------------------|---------------------|-----------------|--------------------|--------------|---------|
| Silica | Silicon | Si | 7.7E-06 | 0.3302 | 2.1 |
| | Bridging oxygen | bO | 0.6502 | 0.3166 | -1.05 |
| | Non-bridging oxygen | nO | 0.6502 | 0.3166 | -0.95 |
| | Hydrogen | H | 0.000 | 0.000 | 0.425 |
| Muscovite | Silicon | Si | 7.7E-06 | 0.3302 | 2.1 |
| | Bridging oxygen | bO | 0.6502 | 0.3166 | -1.05 |
| | Non-bridging oxygen | nO | 0.6502 | 0.3166 | -0.95 |
| | Hydrogen | H | 0.000 | 0.000 | 0.425 |
| Alumina | Silicon | Al | 5.5639E-06 | 0.4271 | 1.575 |
| | Bridging oxygen | O | 0.6502 | 0.3166 | 0.000 |
| | Non-bridging oxygen | nO | 0.6502 | 0.3166 | -0.95 |
| | Hydrogen | H | 0.000 | 0.000 | 0.425 |
| MgO | Magnesium | Mg | 3.778E-06 | 0.5264 | 1.050 |
| | Oxygen | O | 0.6502 | 0.3166 | -1.050 |
| Graphite | Carbon | C | 0.23305 | 0.34000 | 0.0000 |
| CO ₂ | Carbon | C | 0.2245 | 0.280 | 0.70 |
| | Oxygen | O | 0.6568 | 0.305 | -0.35 |
| H ₂ S | Sulphur | S | 1.9289 | 0.3720 | -0.37 |
| | Hydrogen | H | 0.0000 | 0.000 | 0.19 |
| H ₂ O | Oxygen | Ow | 0.6502 | 0.3166 | -0.8476 |
| | Hydrogen | Hw | 0.0000 | 0.000 | 0.4238 |
| <i>n</i> -butane | Methyl group | CH ₃ | 0.8148 | 0.3750 | 0.0000 |
| | Methylene group | CH ₂ | 0.3824 | 0.3950 | 0.0000 |
| <i>n</i> -octane | Methyl group | CH ₃ | 0.8148 | 0.3750 | 0.0000 |
| | Methylene group | CH ₂ | 0.3824 | 0.3950 | 0.0000 |

Appendix B

Supporting Information for

Chapter 4

B.1 Determination of the required number of fluid molecules

The number of n-butane and gas molecules used for the simulations were determined by running simulations in finite pores for the pure fluids (system similar to the one shown in Figure [B.1](#), except that pure fluids are considered and no artificial constraints are imposed on them). The pores are open at both ends and exposed to bulk reservoirs. Initial configurations were obtained by placing fluid molecules in the reservoirs. As the simulations progress, an exchange of fluid molecules occurs between the reservoirs and the pores. The amount of fluids in the reservoir is increased until the amount of fluid molecules adsorbed in the pores

reaches a plateau. The correspondent number of fluid molecules adsorbed in the pore is considered to be the maximum amount that fills the pore. The values are reported in Table B.1, together with the correspondent density in the reservoir.

These simulations are conducted at 350 K.

TABLE B.1: Composition of all simulated systems in this work. In all cases, the simulation temperature was 350K

| Substrate | $N_{but-pore}$ | $\rho_{but-res}$ | N_{CO_2-pore} | ρ_{CO_2-res} | $N_{H_2S-pore}$ | ρ_{H_2S-res} |
|-----------|----------------|------------------|-----------------|-------------------|-----------------|-------------------|
| Silica | 437 | 6.8 | 1214 | 7.1 | 1276 | 5.7 |
| Muscovite | 351 | 4.7 | 1020 | 9.8 | 905 | 11.6 |
| MgO | 386 | 5.3 | 1062 | 9.9 | 962 | 11.9 |

KEY

$N_{but-pore}$ = Number of *n*-butane in the pore

$\rho_{but-res}$ = Density of *n*-butane in the reservoir

N_{CO_2-pore} = Number of CO₂ in the pore

ρ_{CO_2-res} = Density of CO₂ in the reservoir

$N_{H_2S-pore}$ = Number of H₂S in the pore

ρ_{H_2S-res} = Density of H₂S in the reservoir

Unit of density = (1/Å)(10⁻³)

B.2 Pressure calculation

The number of fluid molecules simulated inside each pore is related to the pressure in the reservoir. To estimate such pressure, we considered the system shown in Figure S1. The pores are open at both ends to a reservoir. We implemented the flat-bottomed potentials (artificial walls) using GROMACS integrated with

PLUMED, version 2.3.4, for a total of 70 ns of simulations. 300 n-butane molecules were constrained within the pores by artificial walls at the pore entrances. CO_2 and H_2S molecules were allowed to exchange between pores and reservoir. The amount of fluid molecules in the system is manipulated until the desired amount adsorbed within the pore. The bulk pressure is calculated from the reservoir density as obtained in the last 5 ns of the simulations using the Peng-Robinson equation of state. Snapshots representative of the highest pressures considered for CO_2 in contact with n-butane filled pores carved out of (A) silica, (B) muscovite, and (C) MgO are shown in Figure S1.

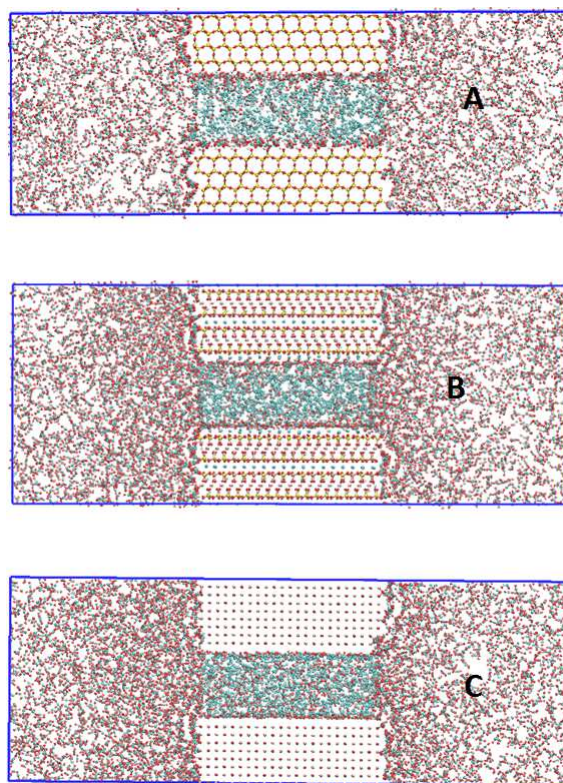


FIGURE B.1: Snapshots for simulation set ups used for pressure calculation in (A) Silica (B) Muscovite (C) MgO. All systems contain 300 n-butane molecules, constrained within the pore. There are 3310, 4138 and 4459 CO_2 molecules in A, B and C respectively. The number of CO_2 molecules in the pore is ~ 500 in A, B and C

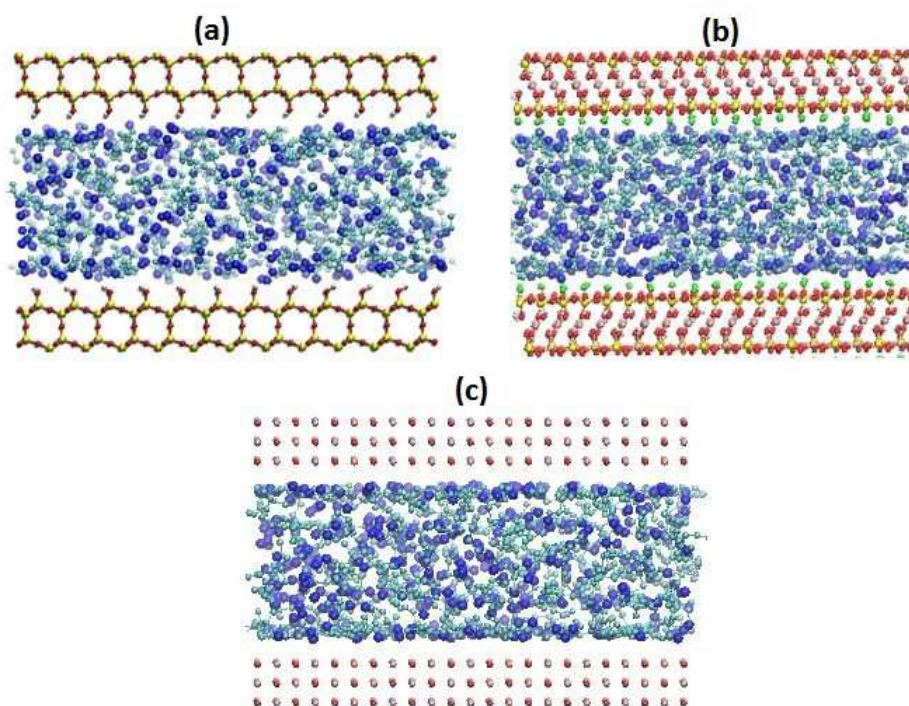


FIGURE B.2: Simulation snapshots for binary systems containing *n*-butane and N₂ in silica (a) Muscovite (b) and MgO (c). All systems shown contain 300 *n*-butane and 500 H₂S molecules. Cyan spheres are -CH₃ and -CH₂ in *n*-butane, purple are sulphur, white are hydrogen, red are oxygen, yellow are silicon, green are potassium, grey are aluminium, blue are magnesium

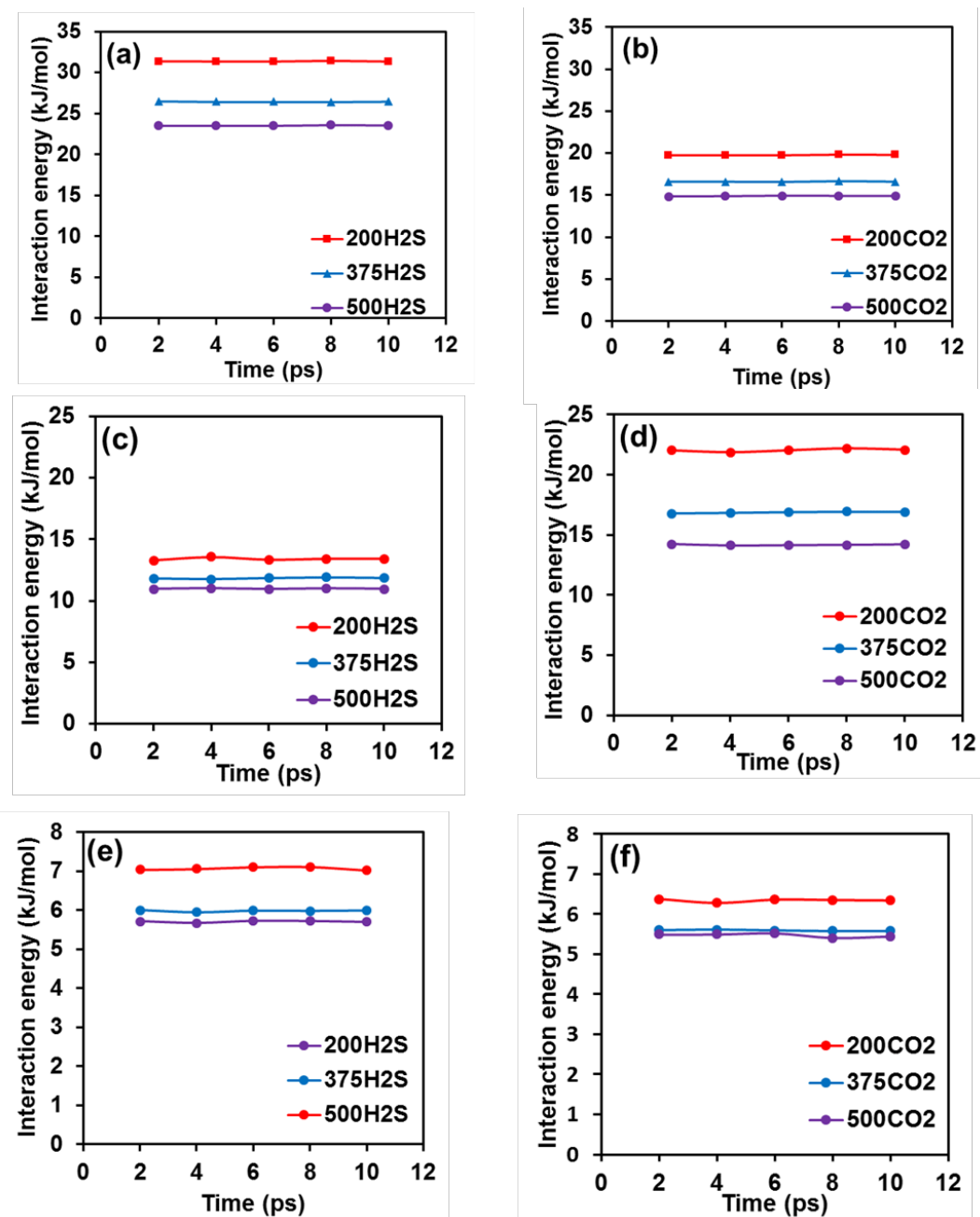


FIGURE B.3: Interaction energy as a function of time over the last 10ns of the simulation for (a) H₂S in muscovite (b) CO₂ in muscovite (c) H₂S in silica (d) CO₂ in silica (e) H₂S in MgO (f) CO₂ in MgO

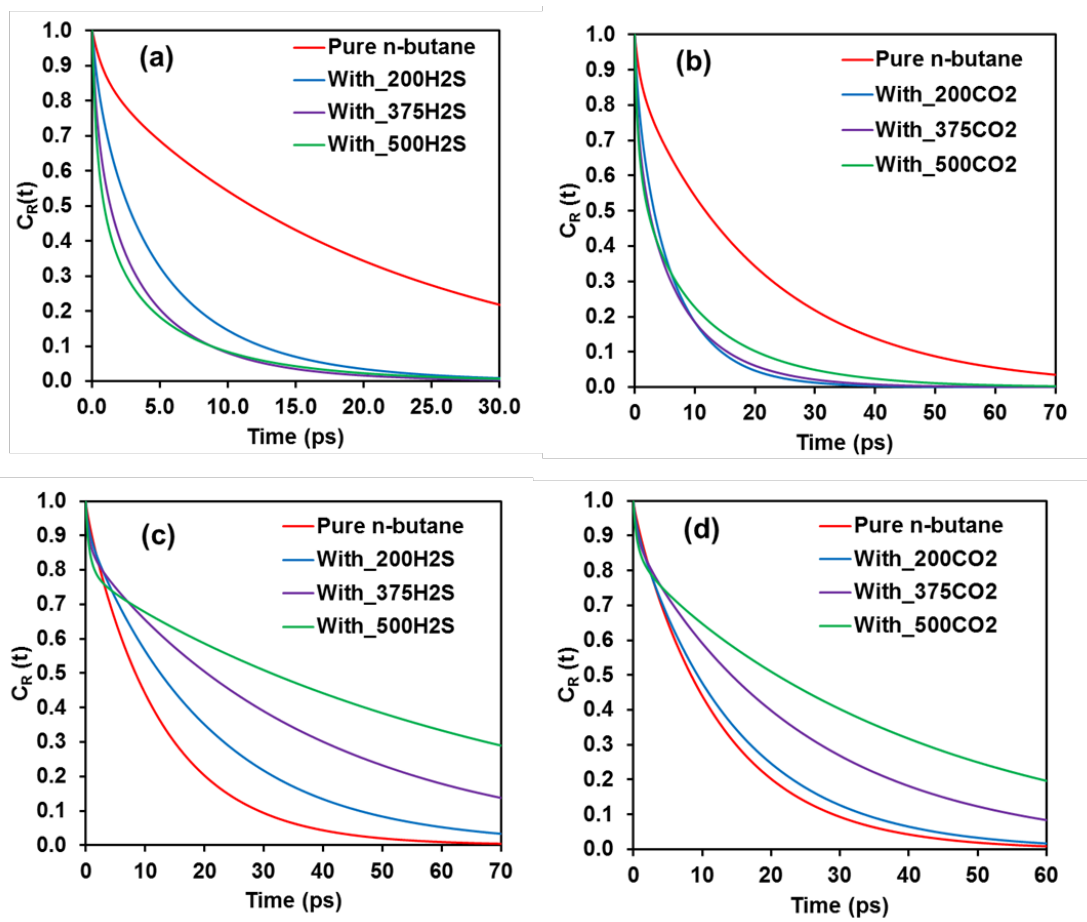


FIGURE B.4: N-butane residence time for binary system of n -butane- H_2S in (a) muscovite (c) MgO and binary systems of n -butane- CO_2 in (b) muscovite (d) MgO.

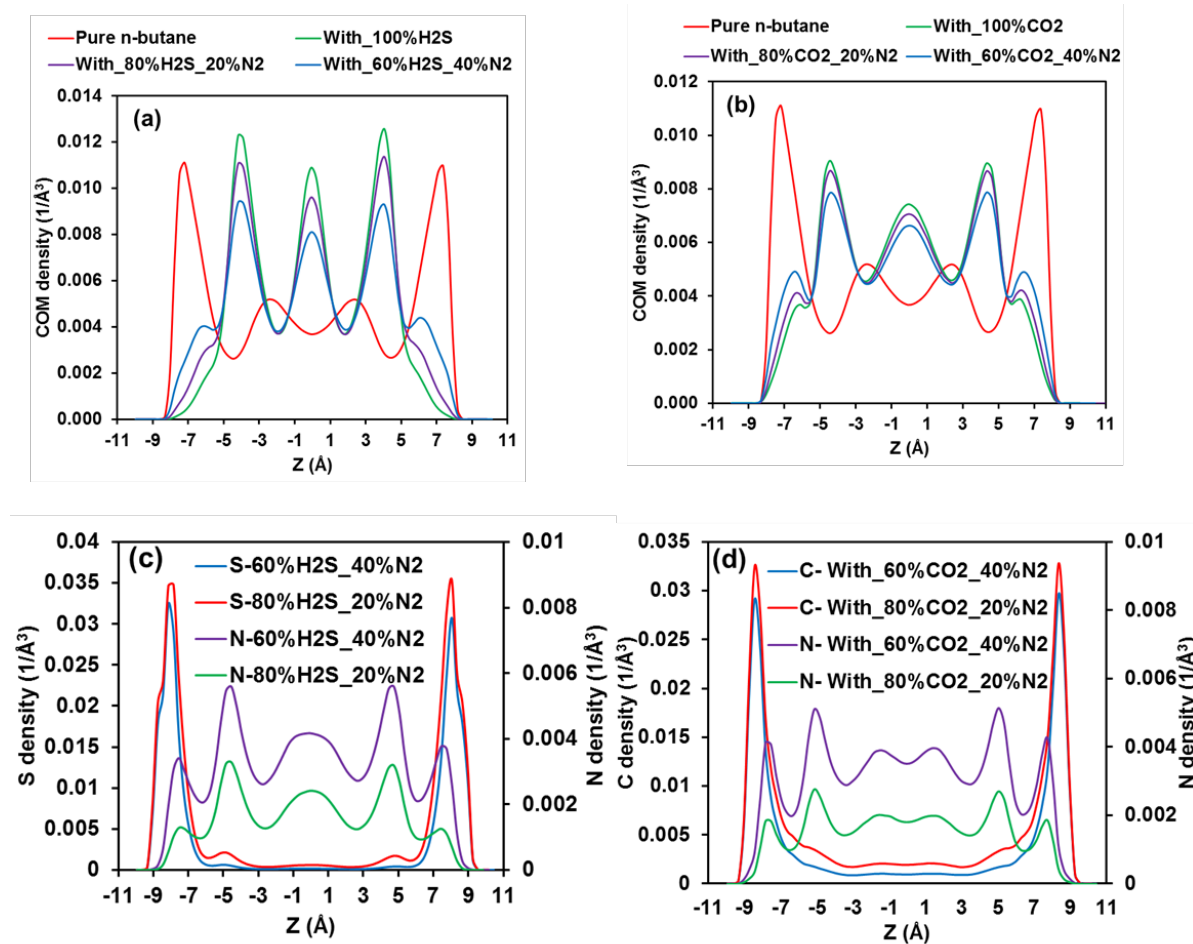


FIGURE B.5: Density profiles of (a) COM of n -butane in n -butane- H_2S - N_2 systems (b) COM of n -butane in n -butane- CO_2 - N_2 systems (c) S and N of H_2S and N_2 (d) C and N of CO_2 and N_2 at different acid gas- N_2 ratios in muscovite pores

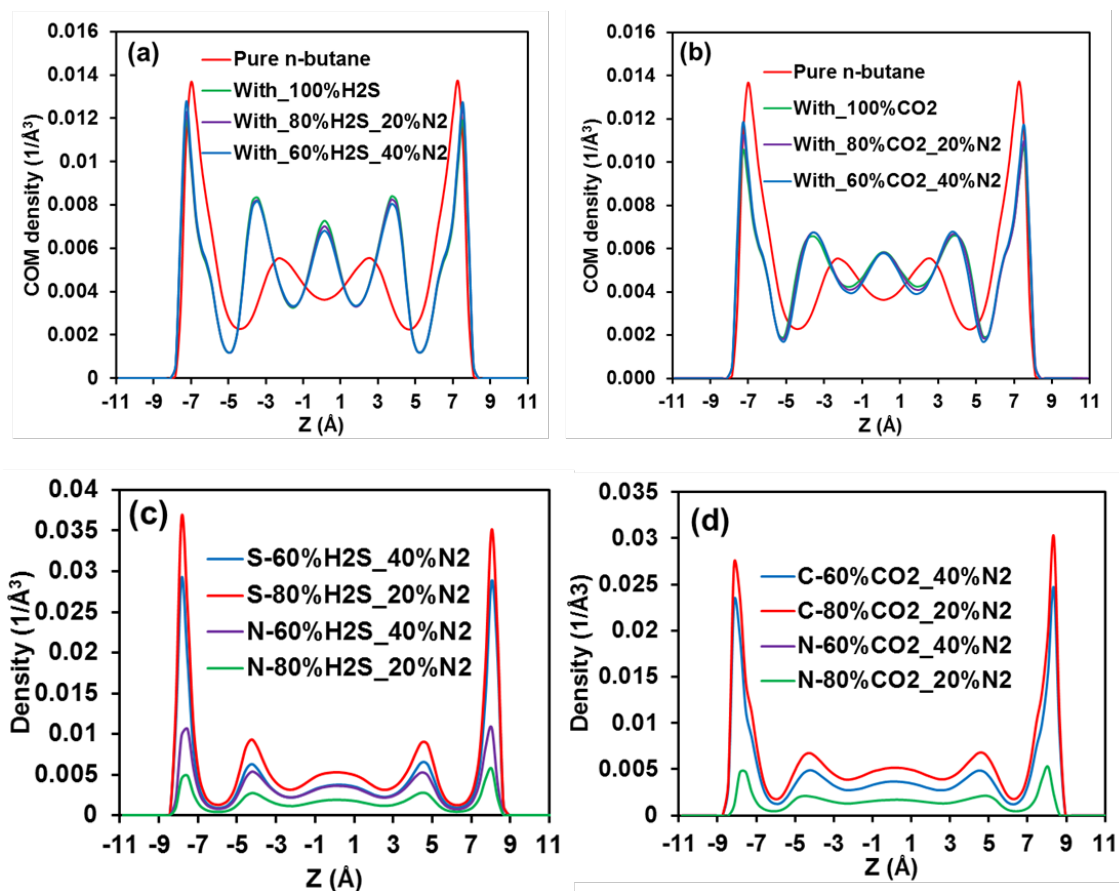


FIGURE B.6: Density profiles of (a) COM of *n*-butane in *n*-butane-H₂S-N₂ systems (b) COM of *n*-butane in *n*-butane-CO₂-N₂ systems (c) S and N of H₂S and N₂ (d) C and N of CO₂ and N₂ at different acid gas-N₂ ratios in MgO pores

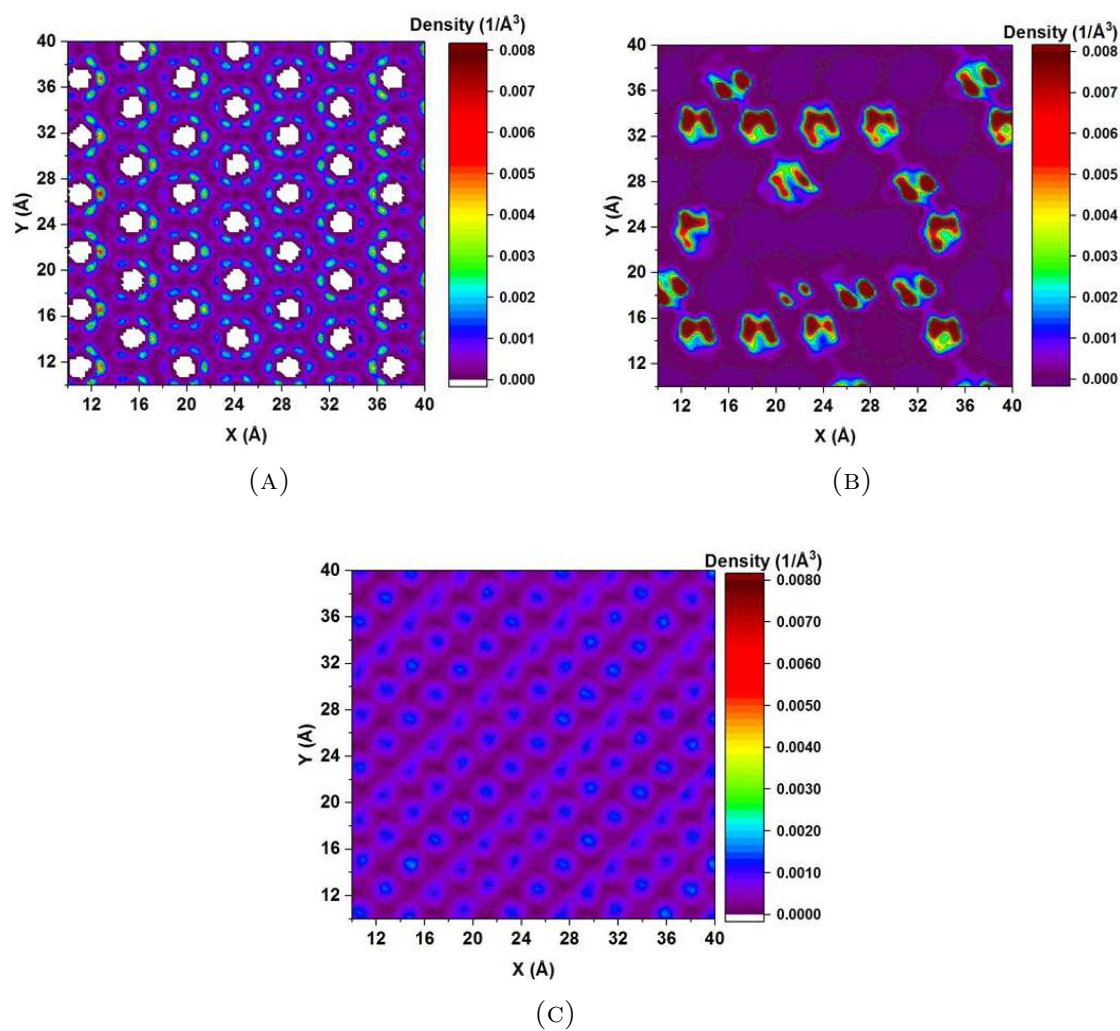


FIGURE B.7: In-plane density distribution of H of H₂S in silica (a) muscovite (b) and MgO (c). All systems contains 500 H₂S and 300 *n*-butane

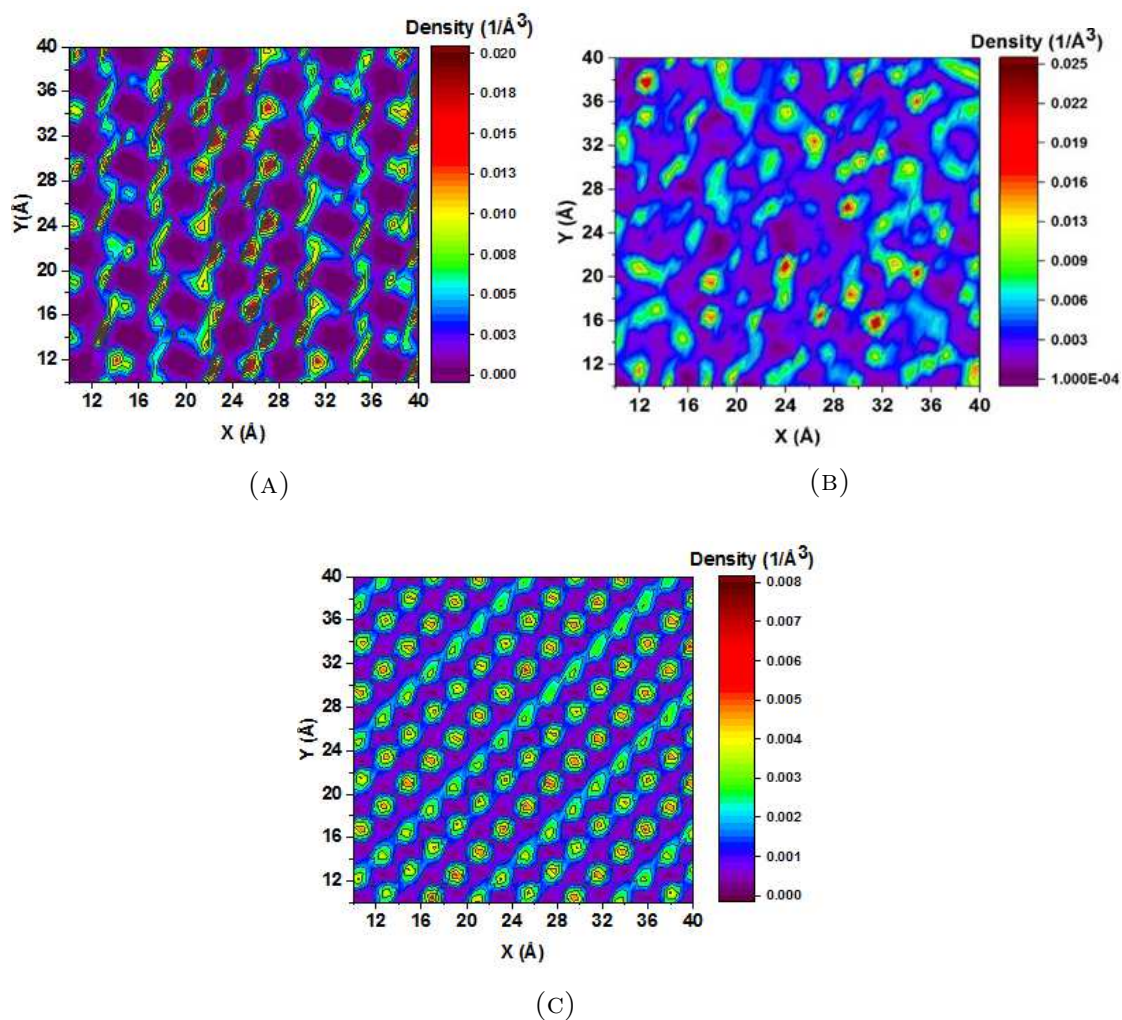


FIGURE B.8: In-plane density distribution of O of CO₂ in silica (a) muscovite (b) and MgO (c). All systems contains 500 H₂S and 300 *n*-butane

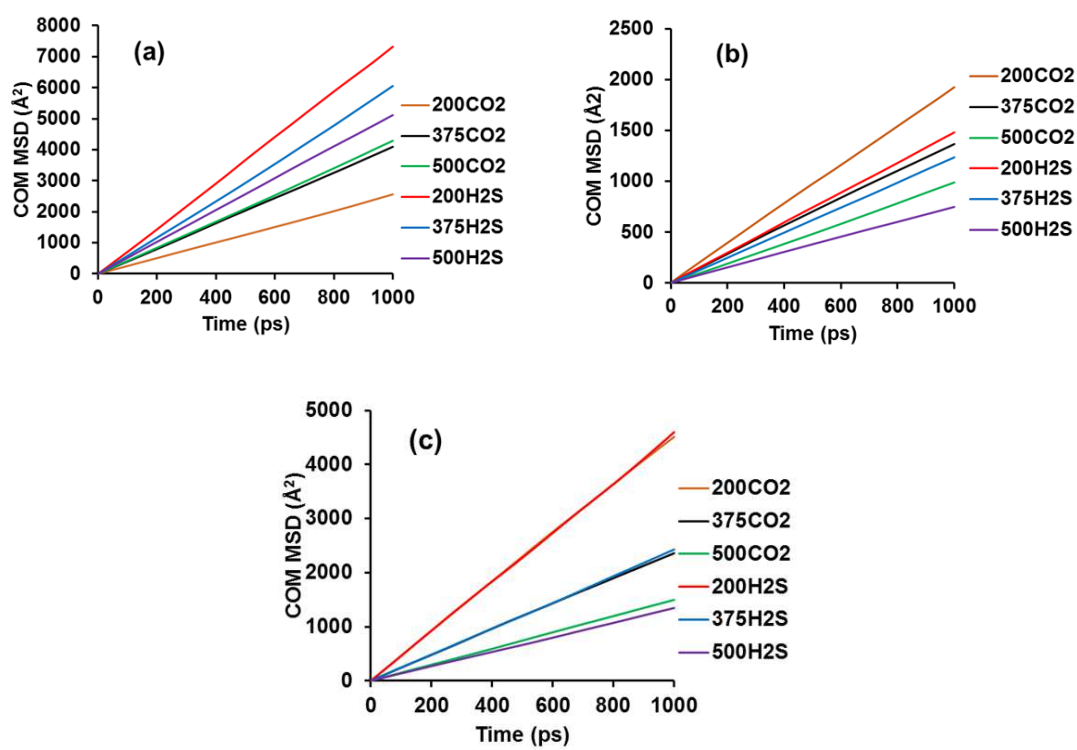


FIGURE B.9: COM MSD for acid gases in binary systems of *n*-butane-acid gas in (a) silica (b) muscovite (c) MgO

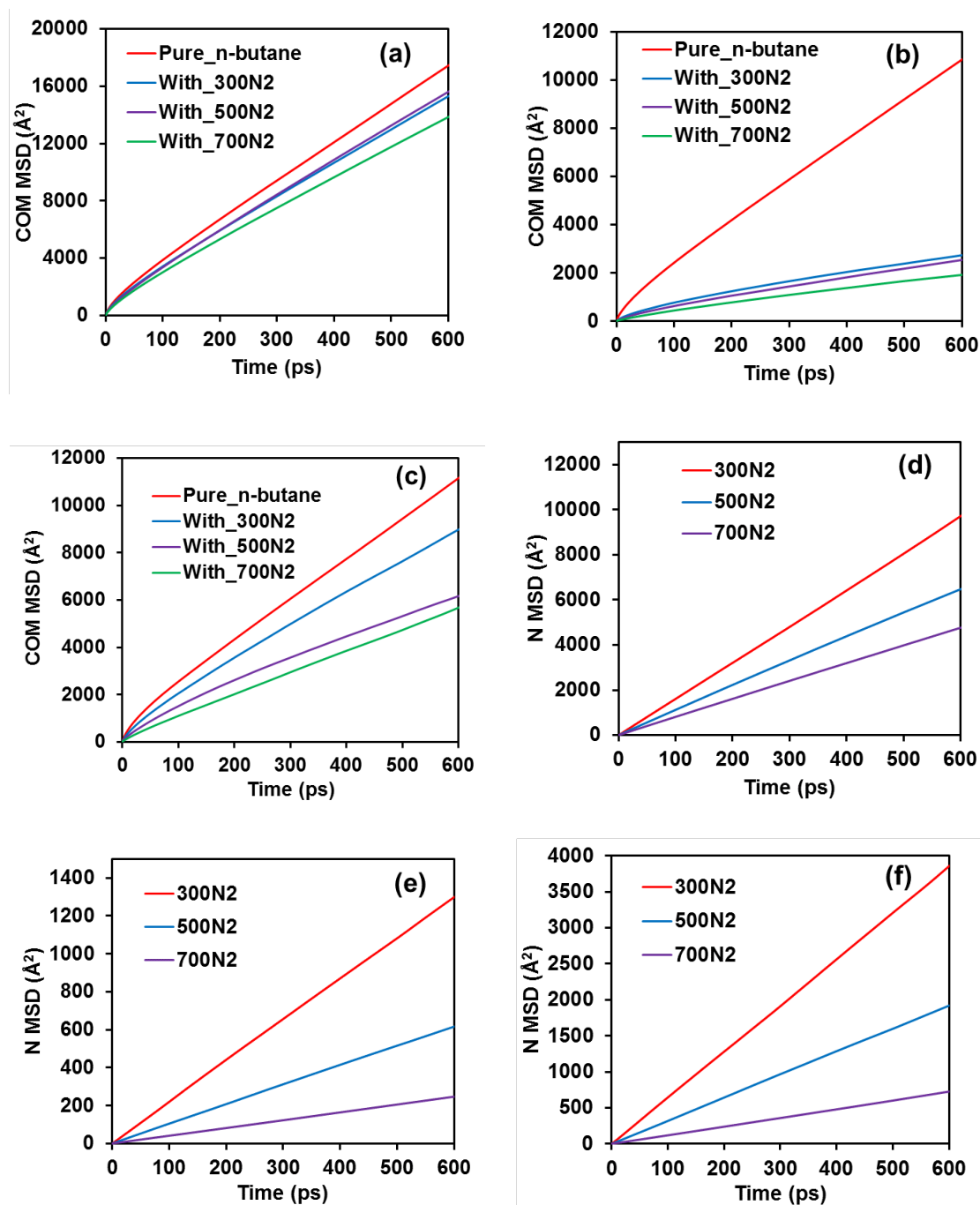


FIGURE B.10: COM MSD of *n*-butane for binary systems of *n*-butane- N_2 in (a) silica (b) muscovite (c) MgO; N MSD of N_2 in (d) silica (e) muscovite (f) MgO

Bibliography

- [1] Mengting Niu, Sha Wang, Xiangxin Han, and Xiumin Jiang. Yield and characteristics of shale oil from the retorting of oil shale and fine oil-shale ash mixtures. *Applied Energy*, 111:234–239, 2013.
- [2] Arun Yethiraj and Alberto Striolo. Fracking: What can physical chemistry offer?, 2013.
- [3] Alan D McNaught and Alan D McNaught. *Compendium of Chemical Terminology*, volume 1669. Blackwell Science Oxford, 1997.
- [4] Lin Ma, Patrick J Dowey, Ernest Rutter, Kevin G Taylor, and Peter D Lee. A novel upscaling procedure for characterising heterogeneous shale porosity from nanometer-to millimetre-scale in 3d. *Energy*, 2019.
- [5] Daniel JK Ross and R Marc Bustin. The importance of shale composition and pore structure upon gas storage potential of shale gas reservoirs. *Marine and Petroleum Geology*, 26(6):916–927, 2009.
- [6] George Everette King et al. Hydraulic fracturing 101: What every representative, environmentalist, regulator, reporter, investor, university researcher,

- neighbor and engineer should know about estimating frac risk and improving frac performance in unconventional gas and oil wells. In *SPE Hydraulic Fracturing Technology Conference*. Society of Petroleum Engineers, 2012.
- [7] Kunimitsu Morishige and Keizi Kawano. Freezing and melting of methyl chloride in a single cylindrical pore: Anomalous pore-size dependence of phase-transition temperature. *The Journal of Physical Chemistry B*, 103(37):7906–7910, 1999.
- [8] W Gorbatschow, M Arndt, R Stannarius, and F Kremer. Dynamics of hydrogen-bonded liquids confined to nanopores. *EPL (Europhysics Letters)*, 35(9):719, 1996.
- [9] Hugo K Christenson. Confinement effects on freezing and melting. *Journal of Physics: Condensed Matter*, 13(11):R95, 2001.
- [10] Gisela Gerstberger and Reiner Anwander. Screening of rare earth metal grafted mcm-41 silica for asymmetric catalysis. *Microporous and Mesoporous Materials*, 44:303–310, 2001.
- [11] Dimitrios Argyris, Naga Rajesh Tummala, Alberto Striolo, and David R Cole. Molecular structure and dynamics in thin water films at the silica and graphite surfaces. *The Journal of Physical Chemistry C*, 112(35):13587–13599, 2008.
- [12] DJ Donaldson and Kalliat T Valsaraj. Adsorption and reaction of trace gas-phase organic compounds on atmospheric water film surfaces: A critical review. *Environmental Science & Technology*, 44(3):865–873, 2010.

- [13] Anh Phan, David R Cole, and Alberto Striolo. Aqueous methane in slit-shaped silica nanopores: High solubility and traces of hydrates. *The Journal of Physical Chemistry C*, 118(9):4860–4868, 2014.
- [14] Linh Ngoc Ho, Stephanie Clauzier, Yves Schuurman, David Farrusseng, and Benoit Coasne. Gas uptake in solvents confined in mesopores: Adsorption versus enhanced solubility. *The Journal of Physical Chemistry Letters*, 4(14):2274–2278, 2013.
- [15] Linh Ngoc Ho, Yves Schuurman, David Farrusseng, and Benoit Coasne. Solubility of gases in water confined in nanoporous materials: Zsm-5, mcm-41, and mil-100. *The Journal of Physical Chemistry C*, 119(37):21547–21554, 2015.
- [16] Mery Diaz Campos, I Yucel Akkutlu, Richard F Sigal, et al. A molecular dynamics study on natural gas solubility enhancement in water confined to small pores. In *SPE Annual Technical Conference and Exhibition*. Society of Petroleum Engineers, 2009.
- [17] Alenka Luzar and Dusan Bratko. Gas solubility in hydrophobic confinement. *The Journal of Physical Chemistry B*, 109(47):22545–22552, 2005.
- [18] Marc Pera-Titus, Rayan El-Chahal, Volainiana Rakotovao, Cécile Daniel, Sylvain Miachon, and Jean-Alain Dalmon. Direct volumetric measurement of gas oversolubility in nanoliquids: Beyond henrys law. *ChemPhysChem*, 10(12):2082–2089, 2009.

- [19] Volaniana Rakotovao, Rachid Ammar, Sylvain Miachon, and Marc Pera-Titus. Influence of the mesoconfining solid on gas oversolubility in nanoliquids. *Chemical Physics Letters*, 485(4-6):299–303, 2010.
- [20] Greeshma Gadikota, Baptiste Dazas, Gernot Rother, Michael C Cheshire, and Ian C Bourg. Hydrophobic solvation of gases (CO_2 , CH_4 , H_2 , noble gases) in clay interlayer nanopores. *The Journal of Physical Chemistry C*, 121(47):26539–26550, 2017.
- [21] LW Tsay, MY Chi, HR Chen, and C Chen. Investigation of hydrogen sulfide stress corrosion cracking of ph 13-8 mo stainless steel. *Materials Science and Engineering: A*, 416(1-2):155–160, 2006.
- [22] Victoria Buch, J Paul Devlin, I Abrey Monreal, Barbara Jagoda-Cwiklik, Nevin Uras-Aytemiz, and Lukasz Cwiklik. Clathrate hydrates with hydrogen-bonding guests. *Physical Chemistry Chemical Physics*, 11(44):10245–10265, 2009.
- [23] Bjørn Kvamme, Tatyana Kuznetsova, and Kjetil Aasoldsen. Molecular dynamics simulations for selection of kinetic hydrate inhibitors. *Journal of Molecular Graphics and Modelling*, 23(6):524–536, 2005.
- [24] Pio Forzatti and Luca Lietti. Catalyst deactivation. *Catalysis today*, 52(2-3):165–181, 1999.
- [25] Yonghou Xiao, Shudong Wang, Diyong Wu, and Quan Yuan. Catalytic oxidation of hydrogen sulfide over unmodified and impregnated activated carbon. *Separation and Purification Technology*, 59(3):326–332, 2008.

- [26] Anh Phan, David R Cole, R Gregor Weiß, Joachim Dzubiella, and Alberto Striolo. Confined water determines transport properties of guest molecules in narrow pores. *ACS Nano*, 10(8):7646–7656, 2016.
- [27] Qamar M Malik, MR Islam, et al. CO₂ injection in the Weyburn field of Canada: Optimization of enhanced oil recovery and greenhouse gas storage with horizontal wells. In *SPE/DOE Improved Oil Recovery Symposium*. Society of Petroleum Engineers, 2000.
- [28] Seyyed Mohammad Ghaderi. *Simulation Study of CO₂ Injection and Storage in Alberta*. PhD thesis, University of Calgary, 2013.
- [29] James J Sheng. Critical review of field EOR projects in shale and tight reservoirs. *Journal of Petroleum Science and Engineering*, 159:654–665, 2017.
- [30] Haoyang Sun, Hui Zhao, Na Qi, Xiaoqing Qi, Kai Zhang, Wenchao Sun, and Ying Li. Mechanistic insight into the displacement of CH₄ by CO₂ in calcite slit nanopores: the effect of competitive adsorption. *RSC Advances*, 6(106):104456–104462, 2016.
- [31] Youguo Yan, Zihan Dong, Yingnan Zhang, Pan Wang, Timing Fang, and Jun Zhang. Co₂ activating hydrocarbon transport across nanopore throat: insights from molecular dynamics simulation. *Physical Chemistry Chemical Physics*, 19(45):30439–30444, 2017.
- [32] Thu Le, Alberto Striolo, and David R Cole. CO₂–C₄H₁₀ mixtures simulated in silica slit pores: relation between structure and dynamics. *The Journal of Physical Chemistry C*, 119(27):15274–15284, 2015.

- [33] Bing Liu, Junqin Shi, Baojiang Sun, Yue Shen, Jun Zhang, Xu Chen, and Muhan Wang. Molecular dynamics simulation on volume swelling of CO₂–alkane system. *Fuel*, 143:194–201, 2015.
- [34] Junfang Zhang, Zhejun Pan, Keyu Liu, and Nick Burke. Molecular simulation of CO₂ solubility and its effect on octane swelling. *Energy & Fuels*, 27(5):2741–2747, 2013.
- [35] Sixu Zheng, Huazhou Andy Li, Huijuan Sun, and Daoyong Yang. Determination of diffusion coefficient for alkane solvent–CO₂ mixtures in heavy oil with consideration of swelling effect. *Industrial & Engineering Chemistry Research*, 55(6):1533–1549, 2016.
- [36] Haoyang Sun, Hui Zhao, Na Qi, and Ying Li. Effects of surface composition on the microbehaviors of CH₄ and CO₂ in slit-nanopores: A simulation exploration. *ACS Omega*, 2(11):7600–7608, 2017.
- [37] Sen Wang, Farzam Javadpour, and Qihong Feng. Fast mass transport of oil and supercritical carbon dioxide through organic nanopores in shale. *Fuel*, 181:741–758, 2016.
- [38] Haibo Zhang and Dapeng Cao. Molecular simulation of displacement of shale gas by carbon dioxide at different geological depths. *Chemical Engineering Science*, 156:121–127, 2016.
- [39] Mirella S Santos, Luís FM Franco, Marcelo Castier, and Ioannis G Economou. Molecular dynamics simulation of n-alkanes and CO₂ confined by calcite nanopores. *Energy & Fuels*, 32(2):1934–1941, 2018.

- [40] Lu Jin, Steven Hawthorne, James Sorensen, Lawrence Pekot, Bethany Kurz, Steven Smith, Loreal Heebink, Volker Herdegen, Nicholas Bosshart, José Torres, et al. Advancing CO₂ enhanced oil recovery and storage in unconventional oil playexperimental studies on bakken shales. *Applied Energy*, 208:171–183, 2017.
- [41] O Eide, G Ersland, B Brattekas, A Haugen, MA Graue, A and Ferno, et al. CO₂ EOR by diffusive mixing in fractured reservoirs. *Petrophysics*, 56(01): 23–31, 2015.
- [42] Essa Georges Lwisa and Ashrakat R Abdulkhalek. Enhanced oil recovery by nitrogen and carbon dioxide injection followed by low salinity water flooding for tight carbonate reservoir: experimental approach. In *IOP Conference Series: Materials Science and Engineering*, volume 323, page 012009. IOP Publishing, 2018.
- [43] Øyvind Eide, Martin A Fernø, Zachary Alcorn, Arne Graue, et al. Visualization of carbon dioxide enhanced oil recovery by diffusion in fractured chalk. *SPE Journal*, 21(01):112–120, 2016.
- [44] Baojian Du and Linsong Cheng. Experimental study of enhanced oil recovery with CO₂ slug+ N₂ flood in low permeability reservoir. *Geosystem Engineering*, 17(5):279–286, 2014.
- [45] Haoyang Sun, Hui Zhao, Na Qi, Xiaoqing Qi, Kai Zhang, and Ying Li. Molecular insight into the micro-behaviors of CH₄ and CO₂ in montmorillonite slit-nanopores. *Molecular Simulation*, 43(13-16):1004–1011, 2017.

- [46] Santiago Romero-Vargas Castrillon, Nicolas Giovambattista, Ilhan A Aksay, and Pablo G Debenedetti. Effect of surface polarity on the structure and dynamics of water in nanoscale confinement. *The Journal of Physical Chemistry B*, 113(5):1438–1446, 2009.
- [47] Michael P Allen and Dominic J Tildesley. *Computer simulation of liquids*. Oxford university press, 2017.
- [48] Randall T Cygan, Jian-Jie Liang, and Andrey G Kalinichev. Molecular models of hydroxide, oxyhydroxide, and clay phases and the development of a general force field. *The Journal of Physical Chemistry B*, 108(4):1255–1266, 2004.
- [49] Marcus G Martin and J Ilja Siepmann. Transferable potentials for phase equilibria. 1. united-atom description of n-alkanes. *The Journal of Physical Chemistry B*, 102(14):2569–2577, 1998.
- [50] Jonathan G Harris and Kwong H Yung. Carbon dioxide’s liquid-vapor co-existence curve and critical properties as predicted by a simple molecular model. *The Journal of Physical Chemistry*.
- [51] Ganesh Kamath and Jeffrey J Potoff. Monte carlo predictions for the phase behavior of $\text{H}_2\text{S} + \text{n-alkane}$, $\text{H}_2\text{S} + \text{CO}_2$, $\text{CO}_2 + \text{CH}_4$ and $\text{H}_2\text{S} + \text{CO}_2 + \text{CH}_4$ mixtures. *Fluid Phase Equilibria*, 246(1-2):71–78, 2006.
- [52] Benoit Coasne, Anne Galarneau, Francesco Di Renzo, and RJM Pellenq. Molecular simulation of nitrogen adsorption in nanoporous silica. *Langmuir*, 26(13):10872–10881, 2010.

- [53] William L Jorgensen. Intermolecular potential functions and monte carlo simulations for liquid sulfur compounds. *The Journal of Physical Chemistry*, 90(23):6379–6388, 1986.
- [54] David Chandler. Introduction to modern statistical mechanics. *Introduction to Modern Statistical Mechanics*, by David Chandler, pp. 288. Foreword by David Chandler. Oxford University Press, Sep 1987. ISBN-10: 0195042778. ISBN-13: 9780195042771, page 288, 1987.
- [55] H. J. C. Berendsen, J. P. M. Postma, W. F. van Gunsteren, A. DiNola, and J. R. Haak. Molecular dynamics with coupling to an external bath. *The Journal of Chemical Physics*, 81(8):3684–3690, 1984. doi: 10.1063/1.448118. URL <http://link.aip.org/link/?JCP/81/3684/1>.
- [56] Daan Frenkel and Berend Smit. Understanding molecular simulations: from algorithms to applications. Technical report, Academic press, 2002.
- [57] Shūichi Nosé. A molecular dynamics method for simulations in the canonical ensemble. *Molecular Physics*, 52(2):255–268, 1984.
- [58] Wm G Hoover. Molecular dynamics. In *Molecular Dynamics*, volume 258, 1986.
- [59] Alper Kinaci, Justin B Haskins, and Tahir Çağın. On calculation of thermal conductivity from einstein relation in equilibrium molecular dynamics. *The Journal of Chemical Physics*, 137(1):014106, 2012.

- [60] Ariel A Chialvo, Lukas Vlcek, and David R Cole. Acid gases in CO₂-rich subsurface geologic environments. *Reviews in Mineralogy and Geochemistry*, 77(1):361–398, 2013.
- [61] Xiaoxing Wang, Xiaoliang Ma, Xiaochun Xu, Lu Sun, and Chunshun Song. Mesoporous-molecular-sieve-supported polymer sorbents for removing H₂S from hydrogen gas streams. *Topics in Catalysis*, 49(1-2):108, 2008.
- [62] WL Robb. Thin silicone membranes-their permeation properties and some applications. *Annals of the New York Academy of Sciences*, 146(1):119–137, 1968.
- [63] Helen Y Huang, Ralph T Yang, Daniel Chinn, and Curtis L Munson. Amine-grafted mcm-48 and silica xerogel as superior sorbents for acidic gas removal from natural gas. *Industrial & Engineering Chemistry Research*, 42(12):2427–2433, 2003.
- [64] Thaer M Al-Jadir and Flor R Siperstein. The influence of the pore size in metal-organic frameworks in adsorption and separation of hydrogen sulphide: A molecular simulation study. *Microporous and Mesoporous Materials*, 271:160–168, 2018.
- [65] Emiel JM Hensen and Berend Smit. Why clays swell. *The Journal of Physical Chemistry B*, 106(49):12664–12667, 2002.
- [66] Yaofeng Hu, Liangliang Huang, Shuangliang Zhao, Honglai Liu, and Keith E Gubbins. Effect of confinement in nano-porous materials on the solubility of a supercritical gas. *Molecular Physics*, 114(22):3294–3306, 2016.

- [67] Tran Thi Bao Le, Alberto Striolo, Siddharth S Gautam, and David R Cole. Propane–water mixtures confined within cylindrical silica nanopores: Structural and dynamical properties probed by molecular dynamics. *Langmuir*, 33(42):11310–11320, 2017.
- [68] Dimitrios Argyris, David R Cole, and Alberto Striolo. Hydration structure on crystalline silica substrates. *Langmuir*, 25(14):8025–8035, 2009.
- [69] Alberto Striolo. From interfacial water to macroscopic observables: a review. *Adsorption Science & Technology*, 29(3):211–258, 2011.
- [70] Saleh Riahi and Christopher N Rowley. Solvation of hydrogen sulfide in liquid water and at the water–vapor interface using a polarizable force field. *The Journal of Physical Chemistry B*, 118(5):1373–1380, 2014.
- [71] Joonho Lee and NR Aluru. Water-solubility-driven separation of gases using graphene membrane. *Journal of Membrane Science*, 428:546–553, 2013.
- [72] Monika Golebiowska, Michael Roth, Lucyna Firlej, Bogdan Kuchta, and Carlos Wexler. The reversibility of the adsorption of methane–methyl mercaptan mixtures in nanoporous carbon. *Carbon*, 50(1):225–234, 2012.
- [73] Raja Kirthi Kalluri, Deepthi Konatham, and Alberto Striolo. Aqueous nacl solutions within charged carbon-slit pores: partition coefficients and density distributions from molecular dynamics simulations. *The Journal of Physical Chemistry C*, 115(28):13786–13795, 2011.

- [74] Bertrand Guillot. A reappraisal of what we have learnt during three decades of computer simulations on water. *Journal of Molecular Liquids*, 101(1-3): 219–260, 2002.
- [75] Ulrich Essmann, Lalith Perera, Max L Berkowitz, Tom Darden, Hsing Lee, and Lee G Pedersen. A smooth particle mesh ewald method. *The Journal of Chemical Physics*, 103(19):8577–8593, 1995.
- [76] Mark James Abraham, Teemu Murtola, Roland Schulz, Szilárd Páll, Jeremy C Smith, Berk Hess, and Erik Lindahl. Gromacs: High performance molecular simulations through multi-level parallelism from laptops to supercomputers. *SoftwareX*, 1:19–25, 2015.
- [77] David Van Der Spoel, Erik Lindahl, Berk Hess, Gerrit Groenhof, Alan E Mark, and Herman JC Berendsen. Gromacs: fast, flexible, and free. *Journal of Computational Chemistry*, 26(16):1701–1718, 2005.
- [78] RW Hockney, SP Goel, and JW Eastwood. Quiet high-resolution computer models of a plasma. *Journal of Computational Physics*, 14(2):148–158, 1974.
- [79] Shuichi Miyamoto and Peter A Kollman. Settle: An analytical version of the shake and rattle algorithm for rigid water models. *Journal of Computational Chemistry*, 13(8):952–962, 1992.
- [80] George Kuranov, Bernd Rumpf, Natalia A Smirnova, and Gerd Maurer. Solubility of single gases carbon dioxide and hydrogen sulfide in aqueous solutions of n-methyldiethanolamine in the temperature range 313- 413 k at

- pressures up to 5 mpa. *Industrial & engineering chemistry research*, 35(6): 1959–1966, 1996.
- [81] RH Wright and O Maass. The solubility of hydrogen sulphide in water from the vapor pressures of the solutions. *Canadian Journal of Research*, 6(1): 94–101, 1932.
- [82] FT Selleck, LT Carmichael, and BH Sage. Phase behavior in the hydrogen sulfide-water system. *Industrial & Engineering Chemistry*, 44(9):2219–2226, 1952.
- [83] Jong Ii Lee and Alan E Mather. Solubility of hydrogen sulfide in water. *Berichte der Bunsengesellschaft für Physikalische Chemie*, 81(10):1020–1023, 1977.
- [84] ECW Clarke and DN Glew. Aqueous nonelectrolyte solutions. part viii. deuterium and hydrogen sulfides solubilities in deuterium oxide and water. *Canadian Journal of Chemistry*, 49(5):691–698, 1971.
- [85] PC Gillespie, JL Owens, and GM Wilson. Sour water equilibria extended to high temperatures and with inerts present. In *AIChE Winter National Meeting, Atlanta, GA*, 1984.
- [86] Virenkumar Shah, Daniel Broseta, Gerard Mouronval, and François Montel. Water/acid gas interfacial tensions and their impact on acid gas geological storage. *International Journal of Greenhouse Gas Control*, 2(4):594–604, 2008.

- [87] John G Kirkwood and Frank P Buff. The statistical mechanical theory of surface tension. *The Journal of Chemical Physics*, 17(3):338–343, 1949.
- [88] JM Míguez, MM Piñeiro, and Felipe J Blas. Influence of the long-range corrections on the interfacial properties of molecular models using monte carlo simulation. *The Journal of Chemical Physics*, 138(3):034707, 2013.
- [89] Ramona S Taylor, Liem X Dang, and Bruce C Garrett. Molecular dynamics simulations of the liquid/vapor interface of SPC/E water. *The Journal of Physical Chemistry*, 100(28):11720–11725, 1996.
- [90] Joost VandeVondele, Matthias Krack, Fawzi Mohamed, Michele Parrinello, Thomas Chassaing, and Jürg Hutter. Quickstep: Fast and accurate density functional calculations using a mixed gaussian and plane waves approach. *Computer Physics Communications*, 167(2):103–128, 2005.
- [91] Structure and dynamics of the TIP3P, SPC, and SPC/E water models at 298 K, author=Mark, Pekka and Nilsson, Lennart, journal=The Journal of Physical Chemistry A, volume=105, number=43, pages=9954–9960, year=2001, publisher=ACS Publications.
- [92] A Tamimi, Edward B Rinker, and Orville C Sandall. Diffusion coefficients for hydrogen sulfide, carbon dioxide, and nitrous oxide in water over the temperature range 293-368 k. *Journal of Chemical and Engineering Data*, 39(2):330–332, 1994.
- [93] Tuan A Ho, Dimitrios Argyris, Dimitrios V Papavassiliou, Alberto Striolo, Lloyd L Lee, and David R Cole. Interfacial water on crystalline silica: a

- comparative molecular dynamics simulation study. *Molecular Simulation*, 37(03):172–195, 2011.
- [94] A Malani, KG Ayappa, and S Murad. Effect of confinement on the hydration and solubility of nacl in water. *Chemical Physics Letters*, 431(1-3):88–93, 2006.
- [95] Richard J Gowers, Max Linke, Jonathan Barnoud, Tyler JE Reddy, Manuel N Melo, Sean L Seyler, David L Dotson, Jan Domanski, Sébastien Buchoux, Ian M Kenney, et al. Mdanalysis: a python package for the rapid analysis of molecular dynamics simulations. In *Proceedings of the 15th Python in Science Conference*, pages 98–105. SciPy, 2016.
- [96] Naveen Michaud-Agrawal, Elizabeth J Denning, Thomas B Woolf, and Oliver Beckstein. Mdanalysis: a toolkit for the analysis of molecular dynamics simulations. *Journal of Computational Chemistry*, 32(10):2319–2327, 2011.
- [97] Eddy Walther Hansen, Ralf Schmidt, Michael Stöcker, and Duncan Akporiaye. Self-diffusion coefficient of water confined in mesoporous mcm-41 materials determined by 1h nuclear magnetic resonance spin-echo measurements. *Microporous Materials*, 5(3):143–150, 1995.
- [98] Markus Ringnér. What is principal component analysis? *Nature Biotechnology*, 26(3):303, 2008.

- [99] Tai Bui, Anh Phan, David R Cole, and Alberto Striolo. Transport mechanism of guest methane in water-filled nanopores. *The Journal of Physical Chemistry C*, 121(29):15675–15686, 2017.
- [100] Hongjun Liu, Sheng Dai, and De-en Jiang. Molecular dynamics simulation of anion effect on solubility, diffusivity, and permeability of carbon dioxide in ionic liquids. *Industrial & Engineering Chemistry Research*, 53(25):10485–10490, 2014.
- [101] Dimitrios Argyris, David R Cole, and Alberto Striolo. Dynamic behavior of interfacial water at the silica surface. *The Journal of Physical Chemistry C*, 113(45):19591–19600, 2009.
- [102] Anh Phan, David R Cole, and Alberto Striolo. Preferential adsorption from liquid water–ethanol mixtures in alumina pores. *Langmuir*, 30(27):8066–8077, 2014.
- [103] Sally M Benson and John Deutch. Advancing enhanced oil recovery as a sequestration asset. *Joule*, 2(8):1386–1389, 2018.
- [104] Auli Niemi, Jacob Bensabat, Vladimir Shtivelman, Katriona Edlmann, Philippe Gouze, Linda Luquot, Ferdinand Hingerl, Sally M Benson, Philippe A Pezard, Kristina Rasmusson, et al. Heletz experimental site overview, characterization and data analysis for CO₂ injection and geological storage. *International Journal of Greenhouse Gas Control*, 48:3–23, 2016.

- [105] Franklin Mattes Orr, John P Heller, and Joseph J Taber. Carbon dioxide flooding for enhanced oil recovery: Promise and problems. *Journal of the American Oil Chemists Society*, 59(10):810A–817A, 1982.
- [106] Timing Fang, Muhan Wang, Yang Gao, Yingnan Zhang, Youguo Yan, and Jun Zhang. Enhanced oil recovery with CO₂/N₂ slug in low permeability reservoir: Molecular dynamics simulation. *Chemical Engineering Science*, 197:204–211, 2019.
- [107] Ingvi Gunnarsson, Edda S Aradóttir, Eric H Oelkers, Deirdre E Clark, Magnús ór Arnarson, Bergur Sigfússon, Sandra Ó Snæbjörnsdóttir, Juerg M Matter, Martin Stute, Bjarni M Júlíusson, et al. The rapid and cost-effective capture and subsurface mineral storage of carbon and sulfur at the carbfix2 site. *International Journal of Greenhouse Gas Control*, 79:117–126, 2018.
- [108] Shundong Yuan, Shiyan Wang, Xueying Wang, Mengmeng Guo, Yudou Wang, and Diansheng Wang. Molecular dynamics simulation of oil detachment from calcite surface in aqueous surfactant solution. *Computational and Theoretical Chemistry*, 1092:82–89, 2016.
- [109] Kristian Jessen, Guo-Qing Tang, and Anthony R Kavscek. Laboratory and simulation investigation of enhanced coalbed methane recovery by gas injection. *Transport in Porous Media*, 73(2):141–159, 2008.
- [110] Piotr Kowalczyk, Piotr A Gauden, Artur P Terzyk, Sylwester Furmaniak, and Peter JF Harris. Displacement of methane by coadsorbed carbon dioxide

- is facilitated in narrow carbon nanopores. *The Journal of Physical Chemistry C*, 116(25):13640–13649, 2012.
- [111] Youguo Yan, Chuanyong Li, Zihan Dong, Timing Fang, Baojiang Sun, and Jun Zhang. Enhanced oil recovery mechanism of CO₂ water-alternating-gas injection in silica nanochannel. *Fuel*, 190:253–259, 2017.
- [112] James J Sheng and Ke Chen. Evaluation of the EOR potential of gas and water injection in shale oil reservoirs. *Journal of Unconventional Oil and Gas Resources*, 5:1–9, 2014.
- [113] Runxi Wang, Fengjie Peng, Kunlun Song, Guang Feng, and Zhaoli Guo. Molecular dynamics study of interfacial properties in CO₂ enhanced oil recovery. *Fluid Phase Equilibria*, 467:25–32, 2018.
- [114] Jun Pu, Xuejie Qin, Feifei Gou, Wenchao Fang, Fengjie Peng, Runxi Wang, and Zhaoli Guo. Molecular modeling of CO₂ and n-octane in solubility process and α -quartz nanoslit. *Energies*, 11(11):3045, 2018.
- [115] Thu Le, Stephanie Ogbe, Alberto Striolo, and David R Cole. N-octane diffusivity enhancement via carbon dioxide in silica slit-shaped nanopores—a molecular dynamics simulation. *Molecular Simulation*, 42(9):745–752, 2016.
- [116] Chawarwan Khan, Robert Amin, and Gary Madden. Effects of CO₂ and acid gas injection on enhanced gas recovery and storage. *Journal of Petroleum Exploration and Production Technology*, 3(1):55–60, 2013.
- [117] Marlene M Huerta, Jose Manuel Alvarez, Eddie Jossy, Ken Forshner, et al. Use of acid gas (CO₂/H₂S) for the cyclic solvent injection (csi) process

- for heavy oil reservoirs. In *SPE Heavy Oil Conference Canada*. Society of Petroleum Engineers, 2012.
- [118] Gernot Rother, Elizabeth G Krukowski, Dirk Wallacher, Nico Grimm, Robert J Bodnar, and David R Cole. Pore size effects on the sorption of supercritical CO₂ in mesoporous cpg-10 silica. *The Journal of Physical Chemistry C*, 116(1):917–922, 2011.
- [119] M Causa, R Dovesi, C Pisani, and C Roetti. Ab initio hartree-fock study of the mgo (001) surface. *Surface Science*, 175(3):551–560, 1986.
- [120] CA Scamehorn, AC Hess, and MI McCarthy. Correlation corrected periodic hartree–fock study of the interactions between water and the (001) magnesium oxide surface. *The Journal of Chemical Physics*, 99(4):2786–2795, 1993.
- [121] Tuan A Ho and Alberto Striolo. Water and methane in shale rocks: Flow pattern effects on fluid transport and pore structure. *AIChE Journal*, 61(9):2993–2999, 2015.
- [122] Stephanie L Teich-McGoldrick, Jeffery A Greathouse, and Randall T Cygan. Molecular dynamics simulations of structural and mechanical properties of muscovite: Pressure and temperature effects. *The Journal of Physical Chemistry C*, 116(28):15099–15107, 2012.

- [123] Jianwei Wang, Andrey G Kalinichev, R James Kirkpatrick, and Randall T Cygan. Structure, energetics, and dynamics of water adsorbed on the muscovite (001) surface: A molecular dynamics simulation. *The Journal of Physical Chemistry B*, 109(33):15893–15905, 2005.
- [124] William M White. *Geochemistry*. John Wiley & Sons, 2013.
- [125] Aashish Tuladhar, Zizwe A Chase, Marcel D Baer, Benjamin A Legg, Jinhui Tao, Shuai Zhang, Austin D Winkelman, Zheming Wang, Christopher J Mundy, James J De Yoreo, et al. Direct observation of the orientational anisotropy of buried hydroxyl groups inside muscovite mica. *Journal of the American Chemical Society*, 141(5):2135–2142, 2019.
- [126] Hiroshi Sakuma and Katsuyuki Kawamura. Structure and dynamics of water on Li⁺, Na⁺, K⁺, Cs⁺, H₃O⁺ exchanged muscovite surfaces: A molecular dynamics study. *Geochimica et Cosmochimica Acta*, 75(1):63–81, 2011.
- [127] Hiroshi Sakuma and Katsuyuki Kawamura. Structure and dynamics of water on muscovite mica surfaces. *Geochimica et Cosmochimica Acta*, 73(14):4100–4110, 2009.
- [128] Yanmei Song and Lenore L Dai. The shear viscosities of common water models by non-equilibrium molecular dynamics simulations. *Molecular Simulation*, 36(7-8):560–567, 2010.
- [129] Haoyang Sun, Hui Zhao, Na Qi, and Ying Li. Simulation to enhance shale gas recovery using carbon dioxide in silica nanopores with different sizes. *Energy Technology*, 5(11):2065–2071, 2017.

- [130] Hirofumi Sato, Nobuyuki Matubayasi, Masaru Nakahara, and Fumio Hirata. Which carbon oxide is more soluble? ab initio study on carbon monoxide and dioxide in aqueous solution. *Chemical Physics Letters*, 323(3-4):257–262, 2000.
- [131] Sakiru Badmos, Alberto Striolo, and David R Cole. Aqueous hydrogen sulphide in slit-shaped silica nano-pores: Confinement effects on solubility, structural and dynamical properties. *The Journal of Physical Chemistry C*, 2018.
- [132] Tran Thi Bao Le, Alberto Striolo, and David R Cole. Structural and dynamical properties predicted by reactive force fields simulations for four common pure fluids at liquid and gaseous non-reactive conditions. *Molecular Simulation*, 44(10):826–839, 2018.
- [133] In-Chul Yeh and Gerhard Hummer. System-size dependence of diffusion coefficients and viscosities from molecular dynamics simulations with periodic boundary conditions. *The Journal of Physical Chemistry B*, 108(40):15873–15879, 2004.
- [134] Burkhard Dünweg and Kurt Kremer. Molecular dynamics simulation of a polymer chain in solution. *The Journal of Chemical Physics*, 99(9):6983–6997, 1993.
- [135] Ahmad Kadoura, Arun Kumar Narayanan Nair, and Shuyu Sun. Molecular dynamics simulations of carbon dioxide, methane, and their mixture in

- montmorillonite clay hydrates. *The Journal of Physical Chemistry C*, 120 (23):12517–12529, 2016.
- [136] Alberto Striolo and Adrian Jones. Shalexenvironment: A multi-disciplinary effort to assess the environmental implications for shale gas exploration and production in europe. In *ABSTRACTS OF PAPERS OF THE AMERICAN CHEMICAL SOCIETY*, volume 252. AMER CHEMICAL SOC 1155 16TH ST, NW, WASHINGTON, DC 20036 USA, 2016.
- [137] Alberto Striolo and David R Cole. Understanding shale gas: Recent progress and remaining challenges. *Energy & Fuels*, 31(10):10300–10310, 2017.
- [138] Bing Liu, Chao Qi, Tingyi Mai, Jun Zhang, Kaiyun Zhan, Zhiliang Zhang, and Jianying He. Competitive adsorption and diffusion of CH₄/CO₂ binary mixture within shale organic nanochannels. *Journal of Natural Gas Science and Engineering*, 53:329–336, 2018.
- [139] Sen Wang, Qihong Feng, Farzam Javadpour, Tian Xia, and Zhen Li. Oil adsorption in shale nanopores and its effect on recoverable oil-in-place. *International Journal of Coal Geology*, 147:9–24, 2015.
- [140] Keith Mosher, Jiajun He, Yangyang Liu, Erik Rupp, and Jennifer Wilcox. Molecular simulation of methane adsorption in micro-and mesoporous carbons with applications to coal and gas shale systems. *International Journal of Coal Geology*, 109:36–44, 2013.

- [141] A Harrison, RF Cracknell, J Krueger-Venus, and L Sarkisov. Branched versus linear alkane adsorption in carbonaceous slit pores. *Adsorption*, 20(2-3):427–437, 2014.
- [142] Kui Lin, Quanzi Yuan, and Ya-Pu Zhao. Using graphene to simplify the adsorption of methane on shale in md simulations. *Computational Materials Science*, 133:99–107, 2017.
- [143] HengAn Wu, Jie Chen, and He Liu. Molecular dynamics simulations about adsorption and displacement of methane in carbon nanochannels. *The Journal of Physical Chemistry C*, 119(24):13652–13657, 2015.
- [144] Quanzi Yuan, Xueyan Zhu, Kui Lin, and Ya-Pu Zhao. Molecular dynamics simulations of the enhanced recovery of confined methane with carbon dioxide. *Physical Chemistry Chemical Physics*, 17(47):31887–31893, 2015.
- [145] Sylwester Furmaniak, Artur P Terzyk, Piotr A Gauden, Piotr Kowalczyk, and Peter JF Harris. Folding of graphene slit like pore walls—a simple method of improving CO₂ separation from mixtures with CH₄ or N₂. *Journal of Physics: Condensed Matter*, 26(48):485006, 2014.
- [146] Xiaoqing Lu, Dongliang Jin, Shuxian Wei, Mingmin Zhang, Qing Zhu, Xiaofan Shi, Zhigang Deng, Wenyue Guo, and Wenzhong Shen. Competitive adsorption of a binary CO₂–CH₄ mixture in nanoporous carbons: effects of edge-functionalization. *Nanoscale*, 7(3):1002–1012, 2015.
- [147] Wang Sen, Feng Qihong, Zha Ming, Lu Shuangfang, Qin Yong, Xia Tian, and Chi ZHANG. Molecular dynamics simulation of liquid alkane occurrence

- state in pores and slits of shale organic matter. *Petroleum Exploration and Development*, 42(6):844–851, 2015.
- [148] Maria Sammalkorpi, Athanassios Z Panagiotopoulos, and Mikko Haataja. Structure and dynamics of surfactant and hydrocarbon aggregates on graphite: A molecular dynamics simulation study. *The Journal of Physical Chemistry B*, 112(10):2915–2921, 2008.
- [149] Jae Hyun Park and Narayana R Aluru. Surface diffusion of n-alkanes: Mechanism and anomalous behavior. *Chemical Physics Letters*, 447(4-6):310–315, 2007.
- [150] Taotao Cao, Zhiguang Song, Sibao Wang, Xinxing Cao, Yan Li, and Jia Xia. Characterizing the pore structure in the silurian and permian shales of the sichuan basin, china. *Marine and Petroleum Geology*, 61:140–150, 2015.
- [151] Valérie Coustet and Jacques Jupille. High-resolution electron-energy-loss spectroscopy of isolated hydroxyl groups on α -Al₂O₃ (0001). *Surface Science*, 307:1161–1165, 1994.
- [152] JH De Boer and BCd Lippens. Studies on pore systems in catalysts ii. the shapes of pores in aluminum oxide systems. *Journal of Catalysis*, 3(1):38–43, 1964.
- [153] Alain C Pierre. *Introduction to sol-gel processing*, volume 1. Springer Science & Business Media, 2013.

-
- [154] Gerardo Campos-Villalobos, Flor R Siperstein, Carmine D'Agostino, and Alessandro Patti. Self-diffusion of glycerol in γ -alumina nanopores: Understanding the effect of pore saturation on the dynamics of confined polyalcohols. *arXiv preprint arXiv:1905.05159*, 2019.
- [155] William A Steele. The physical interaction of gases with crystalline solids: I. gas-solid energies and properties of isolated adsorbed atoms. *Surface Science*, 36(1):317–352, 1973.